La Rivista del Nuovo Cimento
https://doi.org/10.1007/s40766-024-00052-1

REVIEW PAPER

Reversibly switchable fluorescent proteins: "the fair switch project"

Riccardo Nifosì[1] · **Barbara Storti**[1] · **Ranieri Bizzarri**[2,3]

Received: 15 January 2024 / Accepted: 9 February 2024

Abstract

Fluorescent proteins (FPs) have transformed cell biology through their use in fluorescence microscopy, enabling precise labeling of proteins via genetic fusion. A key advancement is altering primary sequences to customize their photophysical properties for specific imaging needs. A particularly notable family of engineered mutants is constituted by Reversible Switching Fluorescent Proteins (RSFPs), i.e. variant whose optical properties can be toggled between a bright and a dark state, thereby adding a further dimension to microscopy imaging. RSFPs have strongly contributed to the super-resolution (nanoscopy) revolution of optical imaging that has occurred in the last 20 years and afforded new knowledge of cell biochemistry at the nanoscale. Beyond high-resolution applications, the flexibility of RSFPs has been exploited to apply these proteins to other non-conventional imaging schemes such as photochromic fluorescence resonance energy transfer (FRET). In this work, we explore the origins and development of photochromic behaviors in FPs and examine the intricate relationships between structure and photoswitching ability. We also discuss a simple mathematical model that accounts for the observed photoswitching kinetics. Although we review most RSFPs developed over the past two decades, our main goal is to provide a clear understanding of key switching phenotypes and their molecular bases. Indeed, comprehension of photoswitching phenotypes is crucial for selecting the right protein for specific applications, or to further engineer the existing ones. To complete this picture, we highlight in some detail the exciting applications of RSFPs, particularly in the field of super-resolution microscopy.

Keywords Fluorescent protein · Photoswitching · RSFP · *Cis–trans* isomerization · Super-resolution imaging

✉ Ranieri Bizzarri
ranieri.bizzarri@unipi.it

1 NEST, Istituto Nanoscienze - CNR and Scuola Normale Superiore, Pisa, Italy

2 Department of Surgical, Medical, Molecular Pathology and Critical Care Medicine, University of Pisa, via Roma 55, 56126 Pisa, Italy

3 Center for Instrument Sharing, University of Pisa, Pisa, Italy

Published online: 29 April 2024

1 Introduction

In his Nobel lecture, Martin Chalfie told the audience that he discovered the existence of an autofluorescent protein at one seminar in the late eighties [1]. When he first heard of a protein spontaneously able to become fluorescent in the cellular setting, he was so excited he could not pay attention to the remaining part of the seminar: the idea of cloning the GFP to tag selectively some cells in *C. elegans* had come up in his mind all of a sudden. It took a few more years of hard work to have it expressed in the little worm and glowing under the microscope [2]. It was 1994, and the "fluorescent protein" age in molecular biology and biophysics had officially begun.

It is hard to fully appreciate the consequences of this discovery. The ability to encode genetically an optical property in a selective manner has opened the way to unprecedented knowledge on how life emerges from the chaotic assembly of biomolecules in the cells, and how cells cooperate to sustain even more complex functions in a multicellular organism [3, 4]. The discovery of GFP has made it possible to *see* cell biochemistry happening in real-time: the roots of life became the subject of countless amazing movies.

One fluorescent protein was not enough. In a few years, the ancestor GFP had been engineered into a palette of colorful reporters, named Fluorescent Proteins (FPs), by the effort of several scientists [5]. Among those, we should mention Roger Tsien, who in 2008 earned the Nobel Prize in Chemistry for the GFP discovery together with Martin Chalfie and Osamo Shimomura, the Japanese scientist who originally isolated and characterized the GFP from the *Aequorea victoria* jellyfish [6]. In the same years, it was discovered that other sea organisms contain proteins similar to GFP in terms of structure and post-translational modification to generate the optical unit referred to as the GFP chromophore [7]. Nowadays, fluorescent proteins appear to be a protein family specific to *Metazoa* and, in spite of their patchy distribution across phyla, it is thought that the common ancestor of all Metazoa most likely possessed the FP gene [8]. Furthermore, also non-Aequorea FPs can be engineered to give artificial variants with tailored optical phenotypes.

As if that was not exciting enough, after a few more years the story of fluorescent proteins took an unexpected turn: the optical properties of some variants could be modified by the external light (Photo-Transformable Fluorescent Proteins, PTFPs) [9]. Even more strikingly, the highly-conjugated GFP chromophore, whose molecular core is shared by all variants regardless of the actual sequence, was found to be intrinsically photochromic. This means it is amenable to reversible photoswitching between two optical states underlined by a simple conformational change between the *cis* and *trans* diastereoisomeric states [10]. Accordingly, Reversible Switchable Fluorescent Proteins (RSFPs) began to be engineered and applied in non-conventional optical schemes [11, 12].

Crucially, PTFPs became one of the pillars of the "super-resolution" revolution in microscopy [13], i.e. the development of strategies circumventing the optical limit of diffraction and enabling theoretically unlimited spatial resolution [14, 15]. Indeed, nanoscopy, as super-resolution microscopy is often named, leverages the optical switch among states to separate in space and/or time the overlapping emissions of nearby

molecules [16]. In this scenario, RSFPs play a key role, as reversible photoswitching between optically distinct ground states enables nanoscopy approaches such as RESOLFT [17] or pcSOFI [18], operating at milder illumination conditions more apt to imaging living cells.

Nowadays, tens of RSFPs have been proposed in the scientific literature, and a considerable number of them have been applied to cell imaging, thereby discovering or characterizing biochemical processes with unprecedented detail. The scope of this review is not to enlist all the variants published in the literature, albeit we did our best to enclose most of them in our description. Rather, on one side we try to posit the genesis and biophysical hallmarks of the photochromic behavior, starting from the basic properties of the *Aequorea victoria* GFP (wtGFP) and dealing with the subtle structure–property relationships that unleash and modulate the photoswitching ability. On the other side, we address the current use of the RSFPs in fluorescence microscopy, with particular attention to super-resolution approaches.

To maintain such a symmetry, the reader is presented with the basis of the photophysical behavior of fluorescent proteins in Sect. 1. Section 2 focuses on the mechanism of reversible photoswitching, provides a mathematical framework to interpret the macroscopic observables endowed by the photochromic ability, and describes in some detail many variants as a way to convey both the structure–property relationship and useful information to design actual experiments. Section 3 is dedicated to the applications of RSFPs in optical microscopy. Yet, instead of merely reporting a list of approaches and variants, we focus mostly on those imaging applications that have been truly enabled, or greatly benefited, by the discovery of RSFPs.

The title of this work plays on words with the famous 1999 horror movie "The Blair Witch Project". In this movie, three students amateurishly film a documentary about a local myth known as the "Blair Witch", unleashing a tragic chain of events. But RSFPs are neither myth nor is their usage associated with fictional evil forces. RSFPs constitute a real and amazing toolbox of probes for optical microscopy; and they represent Science at its best.

2 Fluorescent proteins: from the structure to the function

The identification of a fluorescent protein participating in the bioluminescence system of the jellyfish Aequorea Victoria traces back to the seminal work of Shimomura in the early 1960s [19]. This protein, known as Green Fluorescent Protein (GFP), derived its name from the vivid green fluorescence produced upon UV-blue light excitation. Thereafter, it has been simply referred to as wild-type GFP or wtGFP in accordance with scientific nomenclature. Following its cloning [2, 20, 21], numerous fluorescent and non-fluorescent GFP homologues were discovered in various organisms [7, 22]. Reference [23] summarizes recent findings in the evolutionary history and ecological functions of fluorescent proteins (FP) in sea organisms. Many natural homologues of GFP are non-fluorescent, although they absorb visible light (chromo-proteins or CPs). Moreover, protein engineering through sequence mutagenesis has generated an abundance of Fluorescent Proteins (FPs) with optical properties spanning the visible spectrum and beyond [3, 12]. For a great source of information, the reader is referred

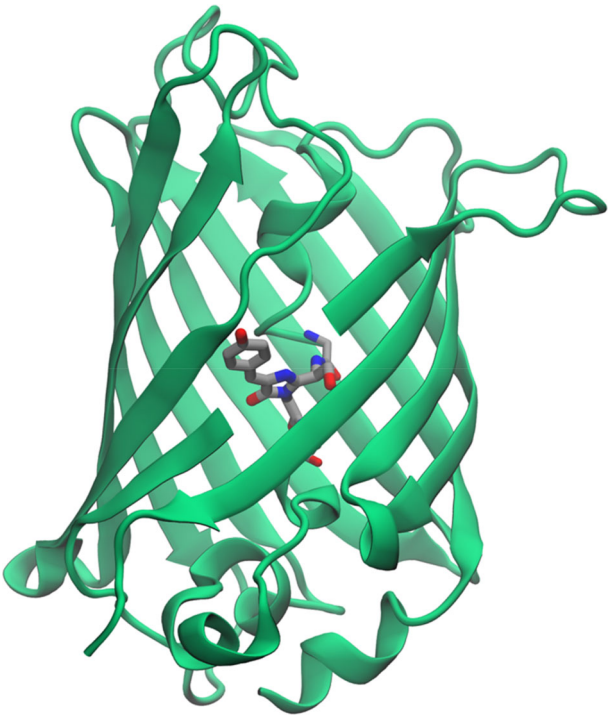

Fig. 1 General structure of Fluorescent Proteins. The tertiary structure of FPs has a characteristic β-barrel fold generated by the cylindrical arrangement of several antiparallel β-sheets around the core chromophore moiety (*p*-HBI). In this image, the frontal β-strand is cut off to offer a view of the chromophore

to the online Fluorescent Protein database (FPbase, www.fpbase.org), which is a free and open-source, community-editable database for FPs and their properties [24].

All known FPs exhibit a notable structural similarity, sharing a conserved β-barrel tertiary structure irrespective of the homology of their primary sequence (Fig. 1) [12, 25, 26]. Differences can be observed in the quaternary structure, as several natural FPs form tightly bound tetramers or dimers, a characteristic that initially hindered their applications. However, primary sequence mutagenesis has, in most cases, reversed this association, yielding monomeric variants of the parent proteins [27–30]. The chromophore moiety, the origin of fluorescence, is autocatalytically generated within the β-barrel fold through sequential cyclization/dehydration/oxidation of an internal tripeptide sequence, as exemplified in Scheme 1 for wtGFP [31], although for some mutants the dehydration and oxidation steps could be reversed [32].

For many variants, additional oxidation reactions can take place, expanding the variety of chromophore structures (Scheme 2) [26]. Fine-tuning of spectral properties arises from the non-covalent interactions of these chromophore structures with the surrounding molecular matrix [33]. This structure-dependent diversity in optical response is undoubtedly one of the factors contributing to the success of FPs. The precise engineering of protein sequences has enabled the tailoring of FPs for specific

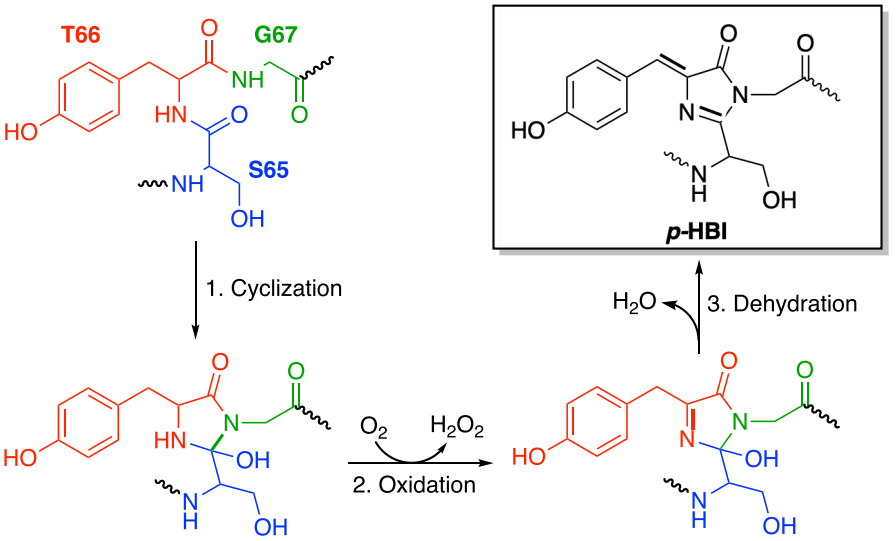

Scheme 1 Formation of the FP chromophore of wtGFP (*p*-HBI). In most FPs, chromophore formation follows from the cyclization-oxidation-dehydratation post-translational processing of an amino acid triplet, which is Ser^{65}-Tyr^{66}-Gly^{67} in wtGFP [38]

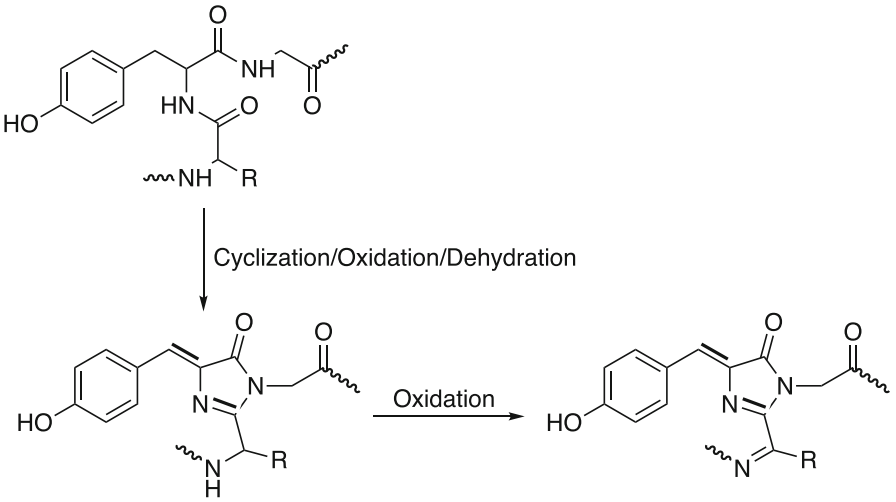

Scheme 2 Formation of a typical FP chromophore of RFPs. In some protein contexts, the chromophore (here a *p*-HBI moiety) can be further oxidized by O_2 to extend electron conjugation, thereby red-shifting the absorption/emission properties of the variant [33]

imaging techniques in cells [4, 12, 34, 35]. The tunability of FPs through sequence engineering, coupled with the careful arrangement of the parent protein structure and chromophore, represents a challenging and highly stimulating field for bioscientists interested in structure–property relationships in biomolecules [34].

While wtGFP has been largely replaced in many applications by its mutants and homologues, it remains a suitable starting point for introducing concepts related to the optical and photophysical properties of FPs, including its ability to undergo reversible switching. Consequently, the reader is initially presented with wtGFP, considered the "photophysical" archetype of FPs. Section 1.1 covers the structure and formation of wtGFP chromophore, while Sect. 1.2 explores the intrinsic photophysical properties of the chromophore, including photoswitching, as highlighted by several studies on synthetic chromophore analogs The ground-state and excited-state properties of wtGFP are reported in Sects. 1.3 and 1.4, respectively. Finally, Sect. 1.5 is a short summary of the main spectral properties of the continuously expanding family of FPs, including both proteins retrieved in nature and their engineered variants.

2.1 Structure of wtGFP

wtGFP consists of a single peptide chain comprising 238 amino acids and has a molecular weight of 27 kDa [5]. In 1996, X-ray spectroscopy revealed for the first time that this sequence folds into a compact cylindrical structure, commonly referred to as a β-barrel (Fig. 1). The lateral wall of this β-barrel is an 11-stranded β-sheet, with a diameter of 24 Å and a height of 42 Å [36]. The β-barrel is capped on both ends by short α-helical sections and traversed by an α-helix containing the amino acids forming the chromophore.

In wtGFP, the chromophore is a 4-(p-hydroxybenzylidene) imidazolidinone, often referred to as *p*-HBI or Y-Chro. *p*-HBI is composed of two conjugated aromatic rings—a six-member aromatic phenol and a five-member imidazolidinone (Scheme 1). The chromophore originates from the post-translational autocatalytic modification of three consecutive amino acids: Ser65-Tyr66-Gly67 [37]. The formation of the GFP chromophore involves three distinct chemical processes triggered by the protein folding into the β-barrel tertiary structure [31, 38] (Scheme 1). In the first step, the tripeptide Ser65-Tyr66-Gly67 cyclizes; in the second step, the cyclic intermediate is oxidized by molecular oxygen to yield a conjugated structure; and in the third step, a water molecule is released. The oxidation reaction represents the rate-limiting step of the overall process and takes at least 30 min to occur [39].

The heterologous expression of the Aequorea GFP gene in other organisms leading to fluorescence demonstrates that the post-translational synthesis of the chromophore does not require any jellyfish-specific enzyme [2]. However, exogenous oxygen is necessary because wtGFP does not develop fluorescence under anaerobic conditions [21].

The imidazolidinone five-membered heterocyclic ring is a common feature of all known FP chromophores [12, 26]. In wtGFP, the alternating single and double bonds in the bridge region extend the electron delocalization from the phenolate to the carbonyl of the imidazolidinone. The efficient absorption of visible light is ultimately

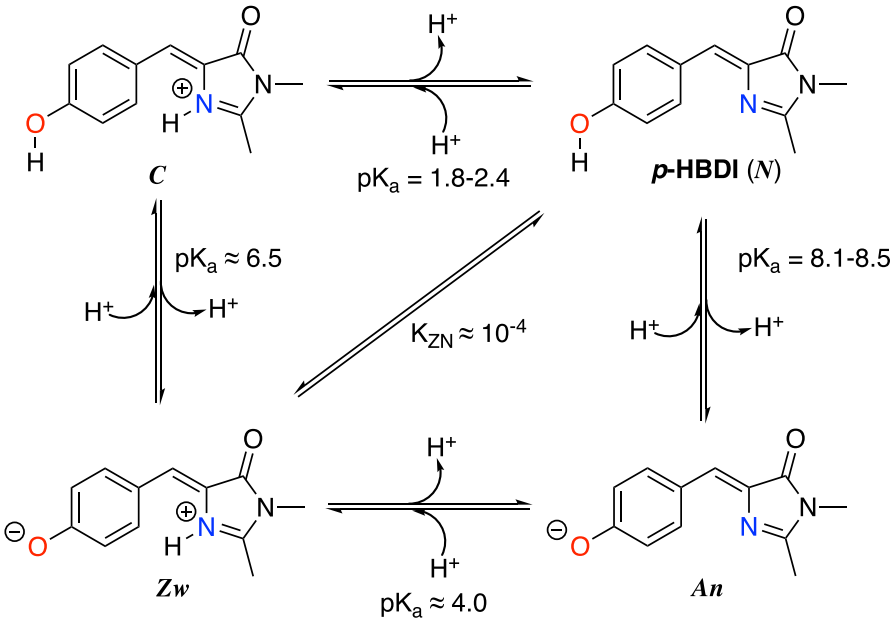

Scheme 3 Ground-state protonation reaction of *p*-HBDI, the synthetic analogue of wtGFP chromophore. *p*-HBDI contains two protonatable heteroatoms, the phenolic oxygen (in red) and the unsubstituted imidazolidinone nitrogen (in blue). Their protonation affords four different species: cationic (O and N are protonated, ***C***), neutral (O is protonated, ***N***), anionic (O and N are deprotonated, ***An***), and zwitterionic (O is deprotonated and N is protonated, ***Zw***). Conventionally, the *p*-HDBI is identified with the ***N*** form, although all four states may occur in water solution depending on pH

determined by this π-conjugated system. It is noteworthy that the phenol ring of the chromophore originates entirely from the lateral group of Tyr66. This allows for the replacement of Tyr66 with other amino acids bearing aromatic side chains, such as phenylalanine, histidine, or tryptophan, to obtain different optical properties [5].

The *intrinsic photophysical* properties of *p*-HBI have been highlighted by using synthetic analogues. The established experimental model for the chromophore of wtGFP and many other FPs variants is a *p*-hydroxybenzylidene-2,3-dimethylimidazolidinone, or *p*-HBDI [40] (Scheme 3). This model includes the relevant π-conjugated system but lacks the side chain of the first residue of the tripeptide, which is Ser in wtGFP.

2.2 Photophysical properties of *p*-HBDI

The ground-state photophysical properties of *p*-HBDI are dominated by its two main protonation sites: the oxygen of the phenol group and the unsubstituted nitrogen in the imidazolidinone ring (Scheme 3). These two protonation sites disclose four protonation states denoted as "protonated" ***C*** (net charge: + 1), "neutral" ***N*** (net charge: 0), "zwitterionic" ***Zw*** (net charge: 0), and "anionic" ***An*** (net charge: − 1) (Scheme 3).

In several organic solvents, ***N*** is the only soluble form and its absorption is located around 350 nm, undergoing a bathochromic shift as the polarity of the solvent increases

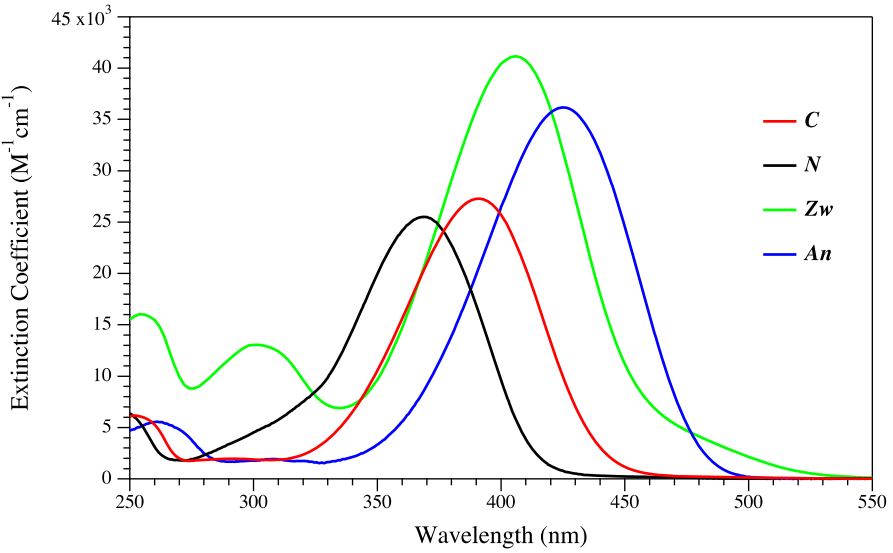

Fig. 2 Absorption of protonation states of p-HBDI in water. The molar absorption spectra of the *N*, *C*, and ***An*** forms of *p*-HBDI, together with that of a structural analogue of ***Zw***, are reported for the 250–550 nm range. Data is taken from Ref. [44]

[41]. In water, each of the four states may occur depending on the pH and exhibit a distinct absorption signature. The ***C***, ***N***, and ***An*** forms have absorption maxima at 387–393, 368–372, and 425–428 nm, respectively (Fig. 2) [41, 42]. The red-shifted absorption of ***An*** compared to ***N*** was attributed to extended electronic conjugation of the former state, which lowers the S0- > S1 transition energy [43]. Due to its scarce population at any pH, absorption of ***Zw*** is not directly measurable. However, a zwitterionic-mimicking derivative was found to absorb at 406 nm in water (Fig. 2) [41].

Changes in absorption spectra with pH were used to obtain the pK_a of the four protonation equilibria. Bell et al. found that the ***C*** → ***N*** ionization has $pK_a = 1.8–2.4$, whereas the ***N*** → ***An*** ionization has $pK_a = 8.2$ [42]. The pK_a of ***C*** → ***Zw*** was found to be ~ 6.5 by using the aforementioned zwitterionic-mimicking *p*-HBDI analogue [41]. These three pK_a values enable the full thermodynamic description of the protonation reactions relevant to *p*-HBDI (Scheme 3). Of note, the proton equilibrium involving ***N*** and ***An*** is the predominant process above pH = 3 (***Zw*** accounts for less than 0.01% of its isoelectric counterpart ***N*** above pH = 3).

In *p*-HBDI, the imidazolidinone and the phenoxy bonds of the methine bridge are referred to as I-bond and P-bond, and rotation angles around these bonds are denoted as τ and ϕ, respectively (Scheme 4). The extended electronic π-system hampers the rotation of one cycle with respect to the other around the I-bond and P-bond, and the molecule is almost planar in its ground-state minimum [45]. Accordingly, *p*-HBDI (and its protonation states) occurs in two stable diastereoisomeric states, i.e., *cis* and *trans* (also referred to *Z* and *E*, respectively), for which ($\phi = 0°$, $\tau = 0°$) and ($\phi =$

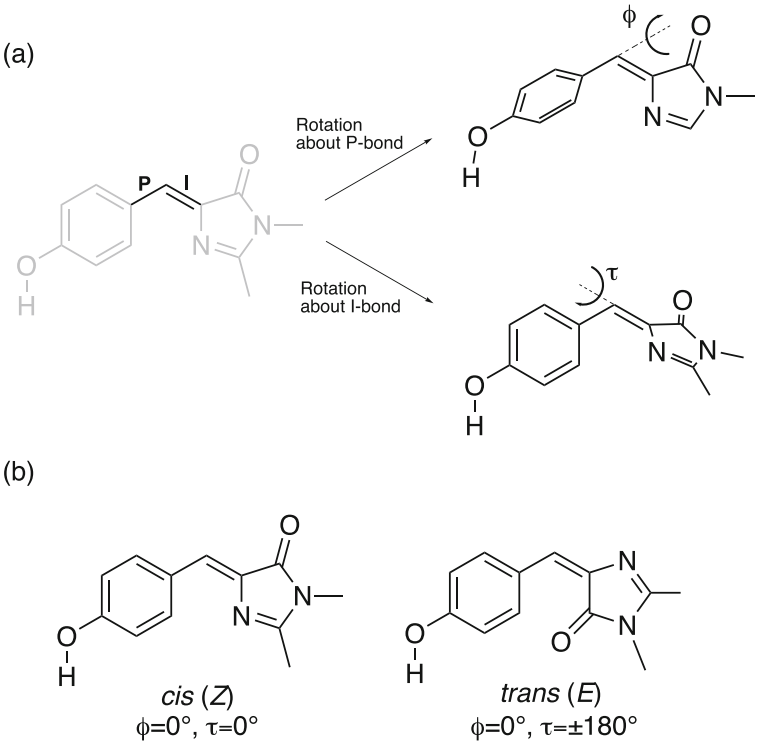

Scheme 4 Stereochemical configurations of *p*-HBDI. **a** The stereochemical configurations of *p*-HBDI are mostly determined by the imidazolidinone (I-bond) and the phenoxy (P-bond) bonds (the other bonds are shown in gray for better visualization), whose rotation angles are ϕ and τ, respectively. **b** *cis* (*Z*) and *trans* (*E*) isomers (diastereoisomers) of *p*-HBDI obtained by full rotation about the I-bond ($\Delta\tau = \pm 180°$)

0°, $\tau = \pm 180°$), respectively (Scheme 4). *p*-HBDI or its ***An*** form contains mostly (> 97.5%) the *cis* isomer at room temperature in water, on account of its significantly higher thermodynamic stability (~ 10 kJ/mol) compared to the *trans* isomer [46]. Of note, *cis* ***C*** is only 3.3 kJ/mol more stable than trans ***C***, possibly on account of the steric repulsion that ensues between the proton on the imidazolidinone N nitrogen and one proton of the phenol ring in the *cis* isomer [46].

In all solvents, the four protonation states of *cis p*-HBDI exhibit negligible fluorescence emission upon excitation on their absorption bands (quantum yields < 10^{-3}) [40]. In a series of seminal papers, Meech's group experimentally showed that the poor emissivity owes to a fast and efficient deactivation channel involving intramolecular torsion of the chromophore in the excited state followed by internal conversion on the picosecond timescale [40, 47–51]. Consistently, *p*-HBDI fluorescence was restored when molecular mobility and the related torsional deactivation channel of the excited state are hindered, i.e., at very low temperatures or in high-viscosity media [40, 47–50]. Fast spectroscopy measurements were carried out also *in vacuo* on electrosprayed ***An****p*-HBDI [52]. ***An*** was found to be almost non-fluorescent *in vacuo*, positing the intrinsic, solvent-independent nature of deactivation mechanisms for excited *p*-HBDI

[53]. This hypothesis was brilliantly confirmed upon the discovery that the initially excited Franck–Condon state of excited ***An*** *in vacuo* relaxes to a twisted intermediate in a few hundred femtoseconds, and from the twisted state to the ground state in about 1 ps [54, 55]. This conclusively stated that the decay mechanisms *in vacuo* and in solution are identical [55]. Low-temperature trapping of the excited state for about 1.2 ns also demonstrated that fluorescence is an intrinsic property of the *p*-HBDI chromophore [56].

The radiationless decay to the ground state has been accounted for by rotations about either P-bond or I-bond by several theoretical studies [57]. According to Olsen et al. [58], photoexcitation generates a biradical excited state, whose fate is influenced by the protonation of the phenolic oxygen. The excited biradical state of ***An*** is delocalized over the molecule, allowing twisting motions about both the P-bond and the I-bond. Yet, rotation about the P-bond is energetically barrierless, whereas some residual energy activation is observed for the I-bond, leading to almost complete twisting through ϕ rotation, as also suggested by Olivucci et al. [45]. Instead, for ***N*** form, the excited biradical state is not delocalized and twisting is favorable *only* about the I-bond [58]. The main radiationless decay by ϕ-rotation of ***An*** has been recently questioned by List et al., whose study fully accounted for inertial effects in the non-equilibrium conditions that follow photoexcitation (Scheme 5) [59]. They concluded that the internal conversion takes places predominantly through twisting around the I-bond, while the P-twist pathway plays a minor role (~ 20% of the population).

Twisting of *p*-HBDI about the I-bond at the excited state is believed to be at the basis of the observed efficient photoisomerization of *p*-HBDI and analogues from

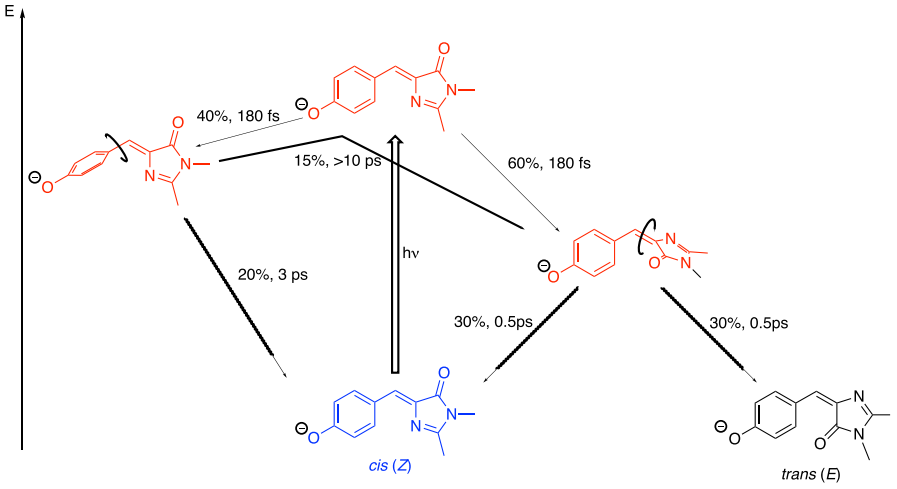

Scheme 5 Excited state processes of isolated *An p*-HBDI according to List et al. [59]. Upon photoexcitation, *cis An p*-HBDI populates a Franck–Condon (LE) state that rapidly (~ 180 fs) evolves almost equimolarly to two twisted intermediates, one about the P-bond (P-twist) and one about the I-bond (I-twist). I-twist undergoes fast (0.5 ps) internal conversion back to *cis An* and to *trans An* with equal probability. P-twist can undergo fast internal conversion to *cis An* or slower (> 10 ps) back-conversion to I-twist. Excited species are in red, the S1 → S0 internal conversions are denoted by wavy arrows

the *cis* to the *trans* state observed in different media [10, 60], as well as *in vacuo* [61]. Indeed, the theoretical work of List et al. strongly supports a photoisomerization mechanism that originates from direct passage through the I-twisted intersection seam (Scheme 5) [59]. This mechanism is referred to as the **one-bond flip** (**OBF**) and is an alternative to the **hula-twist** (**HT**) mechanism, where both P-bond and I-bond undergo a concerted rotation. The same authors calculated that about 30% of the population of excited ***An*** reaches the *trans* state, a value close to the *cis–trans* photoisomerization yields estimated for *p*-HBDI and analogues [10, 60]. On the experimental side, the seminal work by Voliani et al. [10, 60] addressing *cis*/trans quantification of *p*-HBDI and analogs at photo steady state set out for singling out the spectroscopic properties of *trans* isomers. Interestingly, the absorption band of *trans* isomer was found to be only lightly red-shifted compared to *cis,* whereas the excited-state decays of the two isomers are indistinguishable [10, 57, 62]. The minor spectral red shift seems related to oscillator-strength transfer to the excitation involving the molecular orbital localized on the phenolic ring (HOMO-3), possibly due to decreased conjugation over the entire *trans* chromophore [10].

On account of the higher free energy of the *trans* isomer (vide supra), a *trans–cis* ground state isomerization is observable upon photoisomerization at RT. *Trans–cis* ground-state isomerization was found to be a thermally activated process occurring with multiexponential kinetics on a timescale ranging from a few seconds to several minutes [10], in agreement with a measured energy barrier of about 55 kJ/mol for both ***N*** and ***An*** in water [46]. The spontaneous recovery was found to be much faster in protic than in aprotic solvents, pointing to the role of proton mobility [10]. Indeed, *p*-HBDI derivative where the phenolic hydroxyl had been replaced with a hydrogen [10] or a methyl group [63] were found to be stable for several hours in the *trans* state upon photoisomerization. A simple explanation of these findings takes into account the mesomeric or resonance structures of *p*-HBDI yielding partial single bond character to I-bond in ***N*** and ***An***, respectively [63]. Quite consistently, Li et al. have shown by using the H/D exchange effect that the ground-state *trans–cis* isomerization occurs via a mechanism remotely regulated by the proton dissociation of the phenol group by means of one associated water molecule [64] (Scheme 6). Proton dissociation weakens the double bond character of the I-bond, thus favouring the *trans–cis* isomerization. Interestingly, Dong et al. reported that non-ionizable *p*-HBDI

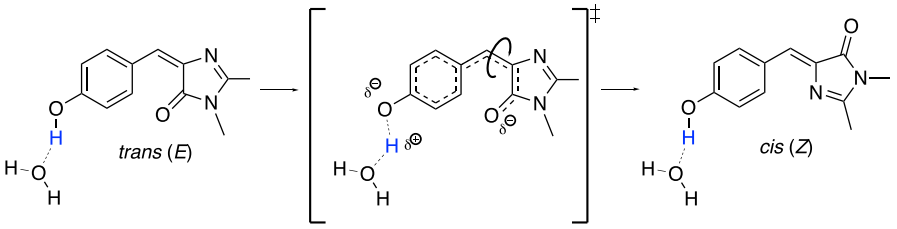

Scheme 6 Mechanism of ground-state *trans* → *cis* isomerization of *p*-HBDI according to Li et al. [64]. A water molecule remotely regulates ground-state *trans* → *cis* isomerization because it decreases the double bond character of I-bond by establishing a direct H-bond interaction with the phenolic proton. Of note, the transition state involves partial dissociation of a phenol proton with the assistance of the associated water

derivatives may nonetheless undergo slow ground-state *trans–cis* isomerization by an addition/elimination step, via a nucleophilic attack at the methine bridge carbon [65].

2.3 Ground state photophysical properties of wtGFP

The first X-ray structure of the protein revealed that chromophore maturation in wtGFP leads to the formation of the *cis*-isomer of *p*-HBI [36]. Yet, the absorption peaks of wtGFP in the optical range are significantly red-shifted (30–50 nm) compared to *p*-HBDI (Fig. 3). The neutral chromophore state, which in wtGFP is referred to as the **A** state, absorbs at 398 nm. The anionic form of the chromophore, which in wtGFP is referred to as the **B** state, absorbs at 475 nm. Remarkably, the absorption of ***An*** can be probed in vacuo by electrospray, and here shows an absorption maximum at 479 nm that nearly coincides with the absorption peaks of **B** [52]. This may suggest that, in the protein, the β-barrel fold shields the chromophore from the surroundings without significantly changing its electronic structure. Nonetheless, the redshifts of **A** and **B** are believed to stem mostly from the complex network of interactions experienced by *p*-HBI within the protein fold [66]. Indeed, X-ray data indicate that *p*-HBI is surrounded by four entrapped water molecules and several charged and polar residues such as Q69, Q94, R96, H148, T203, S205, and E222 [36, 67–69]. Additionally, in **A** and **B** states, the chromophore environment is significantly different: a proton network connecting the chromophore phenol to E222 is active in **A**, whereas it is hindered in **B** due to the 120° rotation of T203 to establish a strong H-bond with the phenolate group [68]. The optical absorption signature of wtGFP is completed by the peak at 280 nm, which is

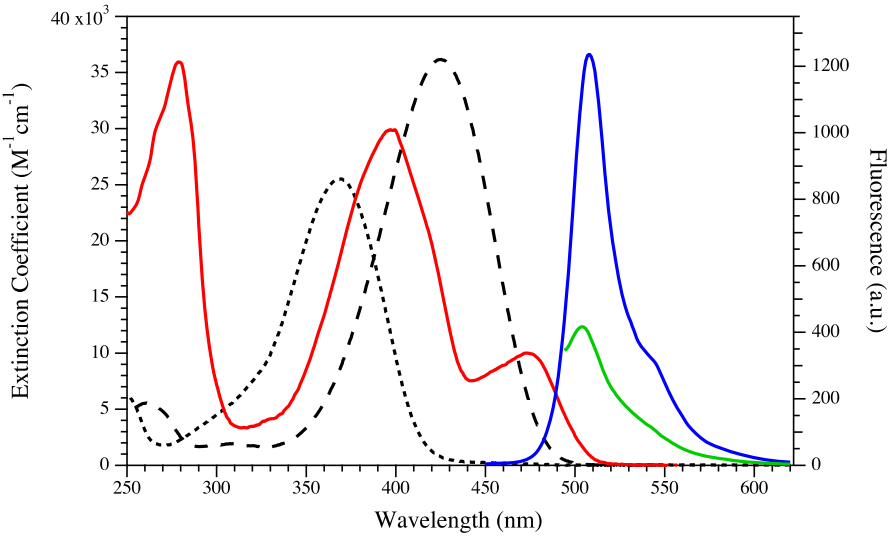

Fig. 3 Absorption and emission spectra of wtGFP. Molar absorption spectrum of wtGFP (red line) and emission spectra obtained by excitation of the **A** state at 400 nm (blue line) and of the **B** state at 488 nm (green line). The absorption spectra of the ***N*** (black dotted line) and ***An*** (black dashed line) forms of *p*-HBDI are reported for comparison. Data is taken from ref [44]

attributed to the side-chains of tyrosine and tryptophan residues in the protein (Fig. 3) [70].

At physiological pH both **A** and **B** states are present in the absorption spectrum of wtGFP with a 3:1 intensity ratio. From the extinction coefficients of the two states, an **A/B** population ratio around 6/1 can be calculated [71]. Surprisingly, however, this ratio is nearly unaffected by changes in proton concentration in the 5–10 pH range [71]. This molecular phenotype was rationalized by the "2S-model" of protonation, a mechanism of proton exchange that is shared by several FP variants [72, 73]. The 2S-model assumes that the protonation of *p*-HBI is thermodynamically coupled with that of a nearby ionizable residue, which is E222 in wtGFP. Depending on the protonation of the two sites we can have four different species, i.e., **A'**, **A**, **B**, **B'** (Scheme 7). Here, the letter represents the protonation state of the phenolic group of the chromophore (**A** and **B** stands for the neutral and anionic forms, respectively), while the absence of the apex means that the total charge of the system is zero (this occurs when the protonation of E222 is the opposite than that of the chromophore).

In wtGFP (and other FPs) the proton coupling between *p*-HBI and E222 is strongly anti-cooperative (i.e.: deprotonation of one site hampers the deprotonation of the other): this leads to an extended pH range where only internal proton exchange takes place and the optical properties are insensitive of the external pH. In wtGFP this pH range goes from 5 to 10, but in many other FPs the range is narrower. Of note, in wtGFP proton exchanges from/to the chromophore are coupled with extended H-bond rearrangements upon proton displacements. First, the E222 residue takes a proton from S205, which in turn accepts it from one structural bridging water molecule (W22), that, as a final step, deprotonates the phenolic group of the chromophore.

2.4 Excited state photophysical properties of wtGFP

The rigid folded structure of wtGFP is also responsible for the significant protein fluorescence emission compared to p-HBDI in water. The **A** state displays $\Phi_A = 0.78$ [74], whereas the **B** state has $\Phi_B = 0.79$ [70]. Fluorescence of both states is also unaffected by the presence of classical quenching agents [75]. **A** and **B** are characterized by minor differences in emission maxima and shapes (Fig. 3), a rather unexpected property given their large difference in absorption maxima. Pump-probe experiments targeting the excited-state depletion at short (ps) timescales highlighted that the emission similarity stems from a proton transfer mechanism occurring at the excited state (Scheme 8) [73, 76, 77]. Photon absorption by **B** leads to excited state **B*** that has a single emission channel at 503 nm with a lifetime around 3 ns (Scheme 8). Conversely, upon excitation of **A**, two competing photo processes leading to emission are triggered: (i) direct emission from **A*** (at 440–480 nm) and (ii) Excited State Proton Transfer (ESPT) from **A*** to Glu222 through a proton wire of H-bonds involving one water molecule and Ser205 eventually leading to 507 nm emission [76–78]. ESPT takes place in a few picoseconds due to the strongly increased acidity of the phenol group in the excited state [43, 73], and it represents a much more efficient depletion channel of **A*** than direct fluorescence emission [79]. In more detail, upon ESPT, **A*** evolves to **I***, an intermediate excited state where the chromophore is anionic like in

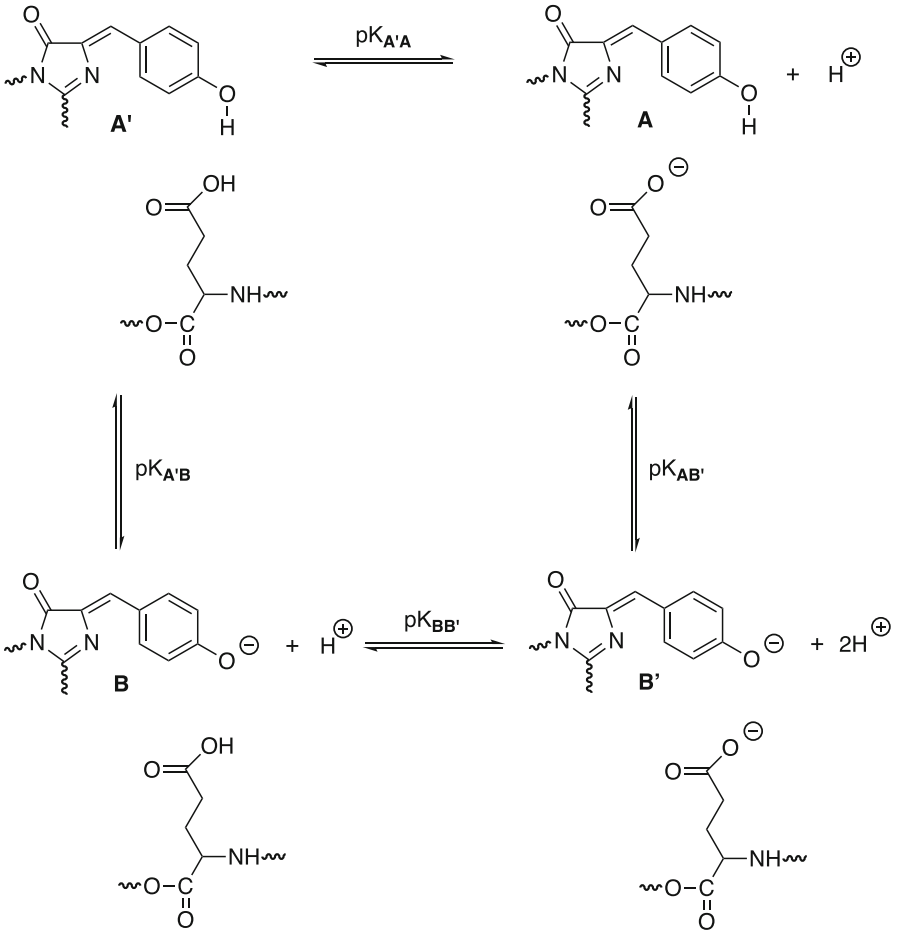

Scheme 7 2S-model of chromophore protonation in wtGFP according to Bizzarri et al. [72]. According to the 2S-model of chromophore protonation, the phenolic protonation of *p*-HBI and a nearby residue (in wtGFP: E222) are thermodynamically coupled. This leads to four different states A', A, B, and B'. The latter is usually not populated in the pH range of protein stability. Depending on the relative pK_a values of *p*-HBI and E222 the protein experiences a pH range where only the two A and B states are populated. Yet, the A/B equilibrium is pH independent, and the optical properties of the protein are not changed upon external pH variation. In wtGFP this range goes from pH 5 to 10

B* but its surrounding residues are in the relaxed form typical of A owing to the very short timescale of **I** decay (a few ns) that does not allow for the rearrangement of the chromophore environment driven by phenol deprotonation (e.g., flipping of the lateral chain of Thr203) (Scheme 8) [77, 80]. This explains why **I*** emits at wavelengths similar, but not equal, to **B***. Upon emission, **I*** decays to **I**, which quickly evolves to **A**, which is more stable by 7.6 kJ/mol of free energy, according to Wiehler et al. [81]. The **I** → **A** conversion seems to take place by reversing the internal proton wire associated with ESPT [68].

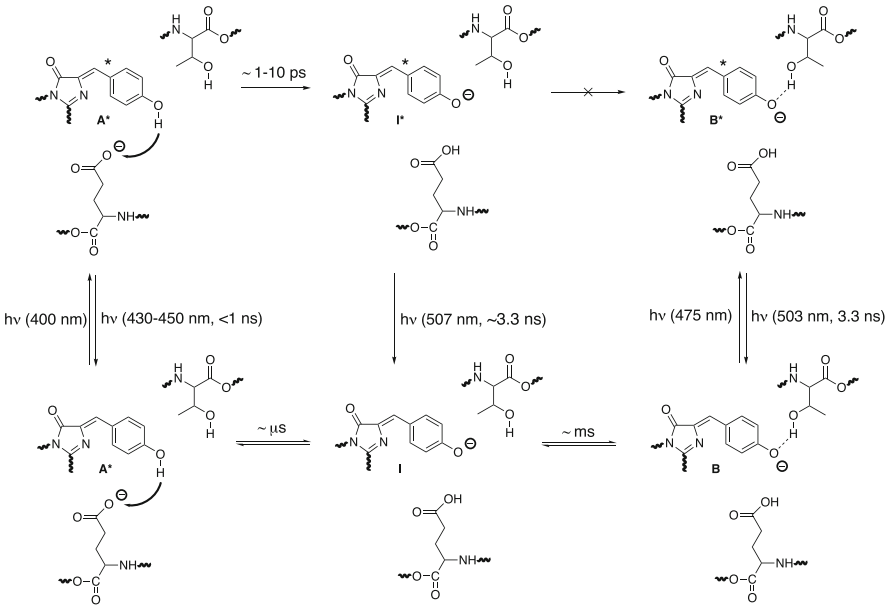

Scheme 8 Photophysical model of wtGFP emission [73, 77]. Excitation of **A** around 400 nm leads to **A***, which yields fast (ps) excited state proton transfer (ESPT) to E222. Yet **A*** does not evolve to **B***, because the ESPT mechanism is too fast for enabling conformational relaxation of the residues surrounding *p*-HBI (here is shown only T203, whose flipping upon chromophore deprotonation is well documented [68]). Thus, **A*** evolves to **I***, an intermediate state where the excited chromophore is anionic, but the protein conformation is unrelaxed. This explains why photoexcitation of **A** leads to an emission similar, but not fully overlapping, that of **B***

2.5 Modulation of the spectral properties of the chromophore: the ever-expanding family of FPs

The development of optimized FPs by protein engineering followed shortly after the first report of exogenous expression of wtGFP in an organism other than *aequorea jellyfish* [82–84]. It was early understood [5] that the optical properties of any FP are the result of: (i) the chromophore structure, particularly the nature of the aromatic ring and the presence of an additional double bond conjugated to the imidazolidinone, (ii) the interaction between the chromophore and its immediate environment. The environment can act on the chromophore by: (a) deforming some of its bond lengths through H-bonds, (b) distorting the planarity of the chromophore, and (c) differentially stabilizing the ground and excited states by electrostatic interactions, these three actions being correlated. Therefore, starting from a plethora of structural (but not sequence) analogs of wtGFP discovered in several sea and terrestrial organisms, spectral as well as other photophysical properties were further tuned by sequence engineering, yielding several hundreds of available variants to comply with the ever-growing demand in the field of optical imaging. The interested reader is referred to several excellent reviews in this field (e.g.: [8, 12, 35]) and the FP internet database (www.fpbase.org).

Here, we shall discuss only a few main issues that prove relevant for understanding the molecular phenotypes of RSFPs.

The pre-chromophore tripeptide has a X(1)-Tyr(2)-Gly(3) sequence in all-natural FPs discovered so far, yielding inevitably a *p*-HBI chromophore upon maturation (Y-Chro). The X(1) position is versatile, accommodating almost any amino acid, while the replacement of Gly(3) disrupts chromophore formation, emphasizing the essential conformational flexibility of Glycine at this site [38]. In contrast, substituting Tyr(2) with aromatic amino acids (Phe, His, or Trp) maintains fluorescence albeit with blue-shifted excitation and fluorescence wavelengths compared to the native protein [5].

The ultimate structure of the chromophore is determined by post-translational processing around the X1 α-carbon. In numerous fluorescent proteins (FPs), including wtGFP, no modifications occur at this site. Conversely, in several natural wtGFP analogs from non-*Aequorea victoria* sea organisms, oxidation of the C-N main chain bond of X1 takes place (Scheme 2) [26, 30, 33, 85]. This oxidation results in an acylimine substituent at the corresponding position of the imidazolidinone ring, and recent findings indicate that this oxidation precedes dehydrogenation of the bridging carbon [86]. From a photophysical perspective, the formation of the acylimine moiety extends the π-conjugated system, thereby lowering the excitation energy and leading to red/orange fluorescence. These proteins therefore constitute the large family of Red Fluorescent Proteins (RFPs).

In some RFPs, additional reactions occur on the acylimine moiety [85]. Examples include hydrolysis associated with backbone cleavage in asFP595, or side-chain cyclization through nucleophilic addition of Threonine (Orange), Cysteine (mKO), or Lysine (zFP538) side chains followed by backbone cleavage [87–89]. In proteins like Kaede and its relatives (KikGR, EosFP, Dendra), UV excitation triggers cleavage of the backbone between the main-chain N and Cα of the Histidine at X1. Subsequently, double-bond formation occurs between Cα and Cβ [90].

Many FPs with *p*-HBI chromophore retain the optical sensitivity from external pH but do not comply with the 2S-model, as they show a simple protonation equilibrium between protonated and deprotonated chromophore (Scheme 9) [72]. In these FPs, ionization of the phenolic group does not couple thermodynamically with that of protonatable nearby residues. In *Aequorea* proteins this occurs because the pK_a of E222 is much higher than that of *p*-HBI, and the latter deprotonates first [72]. Accordingly, the low pH optical state of these variants corresponds to **A'**. To avoid confusion, in the forthcoming sections we shall refer to the low pH optical state of ***any*FP** not obeying the 2S-model as the **A'** state, even if the protein does not belong to the *Aequorea*

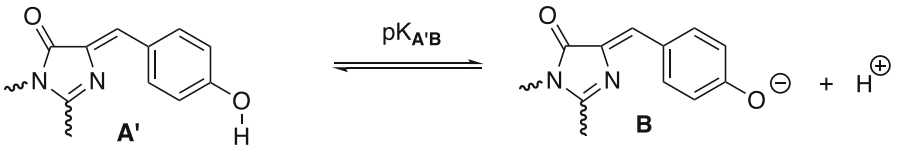

Scheme 9 Simple protonation equilibrium of *p*-HBI. In many Y-Chro FPs, the protonation of the *p*-HBI chromophore is not thermodynamically coupled to the protonation of any other surrounding residue, and a simple ionization equilibrium characterized by only the **A'** and **B** states ensues

family. Of note, the anionic chromophore of most RFPs is much more stable than its neutral counterparts within the pH range of 5–9. This effect is usually attributed to the increased acidity of the phenol group induced by the presence of additional conjugated double bond(s).

3 Reversible photoswitching: an emerging property of several fluorescent protein variants

In this chapter, the reader is initially presented in Sect. 2.1 with a general and comprehensive description of the photoswitching phenomenon, which highlights the relevant physicochemical parameters determining the features of the RSFPs within a quantitative model. In Sect. 2.2 we specifically discuss the properties and mechanism of the largest group of RSFPs, the "negative" switchers possessing a *p*-HBI chromophore analogous to wtGFP. The family of negative switchers is completed in Sect. 2.3 by the description of the "orange-red" RSFPs, which comprises proteins with a *p*-HBI chromophore with extended electronic conjugation. In Sect. 2.4 we address the smaller family of "positive" switchers, which are gathered together regardless of the structure of their chromophore. Eventually, in Sect. 2.5 we consider the special class of "decoupled" switchers, which so far comprises only two members. In each section we describe in some detail most members of the considered group, clustering the different variants on account of the lineage of their farthest ancestor protein.

3.1 The photoswitching phenomenon

3.1.1 Definition of reversibly photoswitchable fluorescent proteins

Early after its demonstration as a genetically encodable probe [2], wtGFP was reported to exhibit several peculiar light-driven transformations such as photoactivation [91–93] and photoconversion [94]. Partial photoswitching was revealed in some engineered *Aequorea* variants of different colors, such as YFP [95], ECFP and Citrine [96], and E^2GFP [97]. Notably, the low yields of these processes made them perceived mostly as nuisances. The scenery radically changed in the early 2000s when a rational approach to protein engineering was applied to both the *Aequorea* family and the newly discovered RFPs from *Anthozoa* organisms such as *Anemonia sulcata* and *Trachyphyllia geoffroyi* [98]. The first efficient *reversibly switchable* proteins KFP1 [99] and Dronpa [100] were developed and applied to novel optical imaging fields such as dynamical tracking.

By definition, the term ***phototransformable*** refers to the family of FPs whose physicochemical properties can be extensively modified by the use of light. Phototransformable FPs comprise three classes of proteins exhibiting different responses to light: ***photoactivatable*** (PAFPs), ***photoconvertible*** (PCFPs), and ***reversibly switchable*** proteins (RSFPs). PAFPs and PCFPs are characterized by *irreversible* photoinduced transformations: from a non-fluorescent to a fluorescent state in the former case, and between two fluorescent states with distinct spectral properties in the latter one. On

the other hand, RSFPs can be reversibly photoswitched back and forth between two distinct optical states several times (*photochromism*). In most RSFPs one optical state is non-emissive and it is referred to as ***off*** or **dark**; its emissive counterpart is denoted as ***on*** or **bright**. PAFPs and PCFPs owe their phototransformation behaviors to *photochemical* mechanisms which entail the covalent (irreversible) modification of the protein chromophore. The photochromism of RSFPs is instead characterized by a reversible conformational rearrangement of the chromophore and its environment. Of note, many *Anthozoa* phototransformable FPs display strong sequence homology: this has enabled the rational combination of photoconversion and photoswitching proteins in some variants [101], as well as the sequence rewiring of PCFPs into RSFPs [102] and vice-versa [103].

3.1.2 Negative, positive and decoupled RSFPs

Depending upon the effect of light absorbed at the excitation peak(s), RSPFs are traditionally categorized into ***negative***, ***positive***, or ***decoupled*** switchers (Fig. 4) [98].

- In negative RSFPs, light at the excitation wavelength induces both fluorescence and the transition from the *on* to the *off* (dark) state. Recovery of the *on* state is accomplished (without any fluorescence) by excitation on the absorption band of the *off state*, which mostly occurs at higher energies (shorter wavelengths) as compared to the *on state.*
- In positive RSFPs, the light that induces fluorescence also toggles the protein from the *off* to the *on* state.
- In decoupled RSFPs the fluorescence excitation spectrum is decoupled from that for optical switching.

By far, negative switchers constitute the largest share of RSFPs reported insofar and were developed from both *Hydrozoa* and *Anthozoa* ancestors. All reported positive switchers, instead, trace their origins back to *Anthozoa* ancestors. The *Aequorea* variants Dreiklang [104] and Spoon [105] are the only examples of decoupled switchers and were not engineered from the positive or negative RSFPs.

The mechanistic principles governing the switching have been elucidated for several RSFPs by crystallographic as well as ultrafast spectroscopy studies [106–109], often coupled with molecular dynamics [110–112]. The pivotal event in the switching process of typical RSFPs involves the intrinsic light-triggered *cis–trans* isomerization of the chromophore (§1.2), as originally proposed by Nifosi et al. [97]. Hence, photoswitching tends to occur spontaneously to a certain degree in numerous fluorescent proteins, and it has been effectively reinstated through engineering efforts in both hydrozoan and anthozoan RSFPs [17, 98]. This result is a clear indication that the chromophore photoisomerization is strictly coupled to the motion of the surrounding β-barrel. *cis* ↔ *trans* photoisomerization is usually accompanied with a protonation change of the chromophore [113–117], as well as by alterations of its planarity and of the surrounding hydrogen-bonding network [118]. Most *cis* chromophores are almost planar, whereas significant deviation from planarity (angles between the five- and six-membered rings ranging from 20° to 45°) is a key feature of *trans* conformation [119]. Of note, a recent study by Chang et al. highlighted that the protein packing

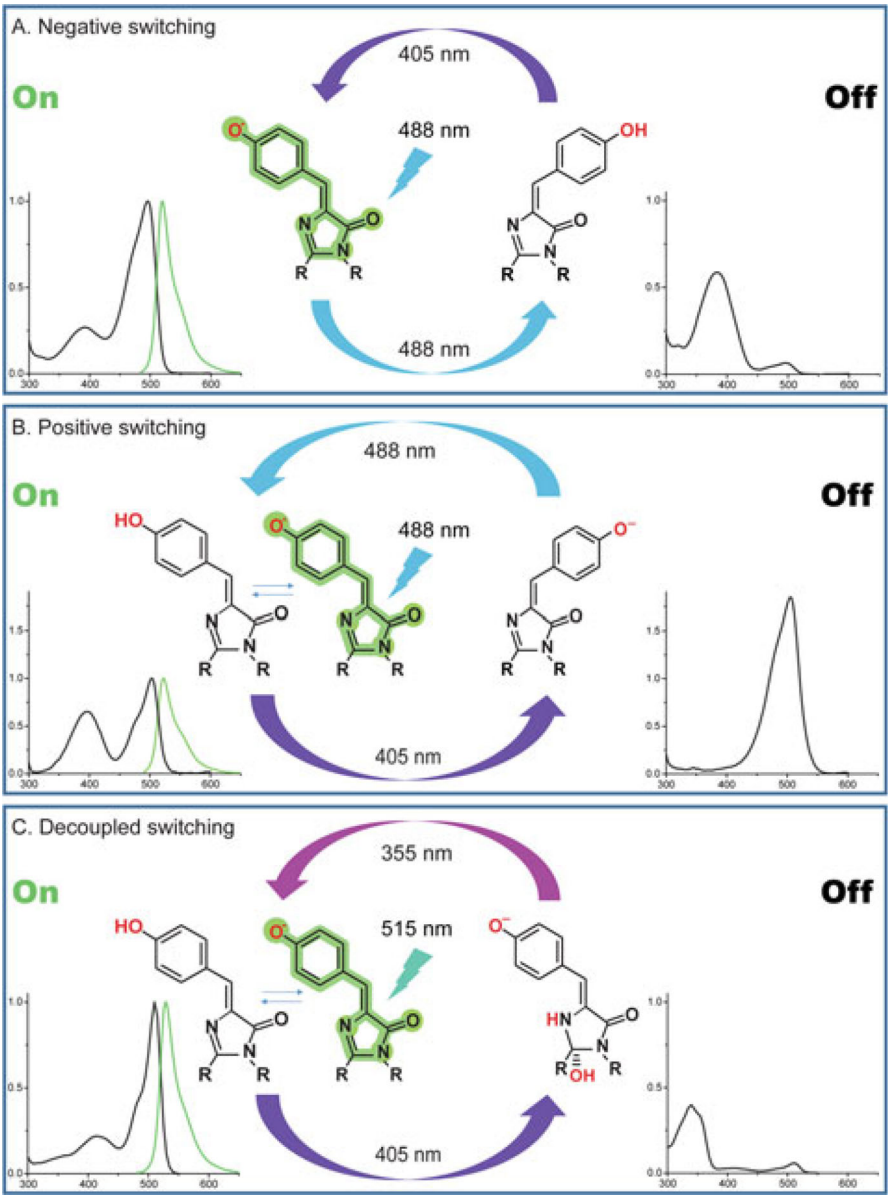

Fig. 4 Families of RSFPs. RSFPs are classified into three distinct families on account of the switching mechanism. **a** In negative switching RSFPs (negative RSFPs), the light that activates fluorescence also drives the *on* → *off* transition. Excitation at shorter wavelengths, instead, restores the *on* state. **b** In positive switching RSFPs (positive RSFPs), the light that activates fluorescence also drives the *off* → *on* transition. Excitation at shorter wavelengths, instead, restores the *off* state. **c** In decoupled switching RSFPs (decoupled RSFPs), proteins are excited with light of a different wavelength than that used for *on*- or *off*-switching. For each family, schematic chromophore structures in the *on* and the *off* states, examples for the switching wavelengths, and the respective absorption and emission spectra are reported. Reprinted with permission from [17]

in the crystal lattice may significantly influence the *cis–trans* photoisomerization: a loose packing configuration leads to the OBF mechanism, while a tight configuration results in the HT mechanism [120].

In most crystallographic structures of conventional RSFPs, the *off*-state exhibits a *trans*-conformation, while the *on*-state displays a *cis*-conformation [108, 116, 121]. The observed strict correlation between *trans p*-HBI and *off* state, however, does not reflect a common photophysical property of FPs, because several non-switchable FPs possess a bright fluorescent chromophore in the *trans* conformation [106, 107].

3.1.3 A quantitative model of RSFP photochromicity

Four parameters recapitulate the photochromic behavior of any RSFP: the photoswitching quantum yields, the extinction coefficients of *on* and *off* states, the thermal recovery rate from the *off* state to the *on state*, and the quantum yield(s) of irreversible photobleaching. At a given illumination wavelength and intensity, these parameters determine the major observable properties of RSFPs (Fig. 5), namely:

The ***photoswitching rates***, i.e. the net rates of *on* ↔ *off* photoconversion. Faster photoswitching rates are preferable in most applications of RSFPs [17].
The ***residual fluorescence*** in the *off* state within a protein ensemble. This corresponds to the emission that survives upon complete *off*-photoswitching and stems from the photosteady-state which is reached by illuminating at any given wavelength [122]. The ratio between the maximum fluorescence and the residual fluorescence is called the ***contrast*** of the RSFP. The contrast defines the dynamic range of any switching measurement and, therefore, its S/N ratio. High contrast values (> 10) are essential in most applications of RSFPs, particularly those in super-resolution imaging [17].
The ***switching fatigue***, expressing the fraction of the proteins that is destroyed at every photochromic cycle. Low switching fatigues enable more switching cycles per unit time, which is beneficial to any application of RSFPs [16].

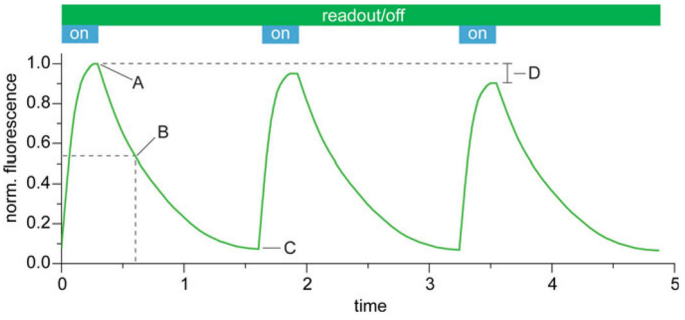

Fig. 5 Observable properties of the reversible photoswitching phenomenon. The figure shows an exemplary switching curve of a negative RSFP switched consecutively *on* and *off* with green and blue light. From the plot of the fluorescence intensity, four quantitative properties can be recovered: **A** the effective brightness, **B** the switching rate (here *off*-switching), **C** the residual fluorescence in the *off*-state, **D** the switching fatigue. Reprinted with permission from [17]

To these properties, we must add the ***brightness***, defined as the product of the extinction coefficient of the protein in the *on* state at the excitation wavelength and the emission quantum yield. It is worth noting that the actual fluorescence intensity of a protein ensemble in the *on* state, named *effective brightness*, may be lower than the calculated brightness because some chromophore population resides in a non-emissive depending on the solution pH, the maturation and turnover rates, the temperature, the presence of protein tags and other factors [17]. A high effective brightness is quintessential to any RSFP application and strategies to maximize it are usually devised when the protein is engineered [102].

In the following, we shall present a general model of photochromic conversion of an RSFP denoted as P under the assumption that photoconversion occurs between a bright (denoted as P_B) and a dark (denoted as P_D) state. This treatment is agnostic in terms of the switching mechanism, but we may occasionally identify P_B and P_D with the *cis* and *trans* isomers of the protein chromophore, owing to the generality of *cis* $\leftrightarrow$ *trans* photoisomerization in RSFPs (§2.1.2). We shall also include a thermal isomerization channel operating from the P_D to the P_B states with a rate constant k_{on}. Indeed, in most RSFPs the *trans* conformer has a higher free energy than the *cis* conformer, and a thermal *trans* $\rightarrow$ *cis* relaxation has been repeatedly observed in the physiological range of pH and temperature (§2.1.2), similarly to the behavior of the isolated chromophore (§1.2). Clearly, the notation swap $k_{on} \rightarrow -k_{off}$ must be applied if the thermal channel goes in the opposite way. Finally, we also consider a slow progressive photobleaching of the protein under illumination to an irreversible *off* state P_{Bl}.

Of note, we shall assume that photoswitching, thermal recovery or irreversible photobleaching are much slower than any other equilibria that may involve the chromophore, e.g. its protonation exchanges with nearby residues. Also, for protein ensembles, we shall assume that the protein diffusion in the observation volume is much faster than any kinetics related to photoswitching (well-stirred solution approximation), so to avoid a spatial dependence of P_D and P_B concentrations owing to non-uniform illumination as it occurs in optical microscopy [123]. Neglecting any process unrelated to photoswitching greatly simplifies the mathematical analysis because it links the observed changes of P_B and P_D only to photoinduced processes. Although this approach can be justified in many applications where the photoswitching rate is low to moderate (characteristic times of switching between the microsecond to second range, contingent upon the applied light intensity [112, 124–127]), these hypotheses should be always tested in real experiments.

Ensemble behavior at single illumination wavelength and in the absence of irreversible photobleaching We shall start our mathematical description by considering a small rectangular volume of a RSFP solution at constant temperature and pH (Fig. 4). The volume is illuminated in a front-face configuration on its lateral surface S, and its thickness (which is also the optical path) is Δx, with $V = S\Delta x$ (Fig. 6a). The photoisomerization is carried out by illuminating with a light of intensity I_0 at a wavelength λ where the absorption of P_B and P_D are A_B and A_D along the light path Δx, respectively. We also introduce the photoisomerization quantum yields φ_{on} ($D \rightarrow B$) and φ_{off} ($B \rightarrow D$), which do not dependent on the illumination wavelength (Fig. 6b).

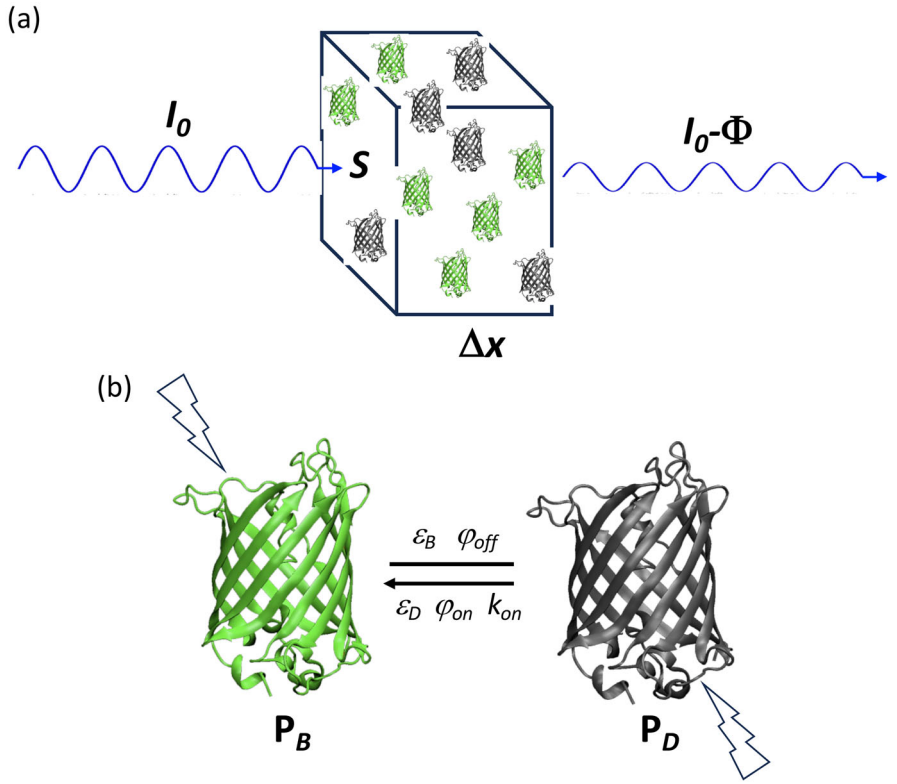

Fig. 6 Reversible photoswitching of a FP. **a** Light with wavelength λ and intensity I_0 impinges orthogonally on the surface S of a small volume V (thickness = Δx) which encloses a solution of RSFP at constant pH and temperature; some light is absorbed (φ) by the RSFP molecules, which may undergo photoswitching between a **bright** (green proteins) and a **dark** (black proteins) state. **b** Scheme of reversible photoswitching of the protein between the **bright** state P_B (green structure) and the **dark** state P_D (black structure) state; the photoswitching is determined by the molar absorptions of P_B (ε_B) and P_D (ε_D), as well as the photoswitching yields ε_{off}, ε_{on} and the thermal rate constant k_{on}

In the absence of irreversible photobleaching, the kinetics of photoswitching are expressed by the following equations [10, 117]:

$$\frac{d[P_B]}{dt} = \frac{S\Phi}{V}\left(-\frac{A_B}{A_B + A_D}\varphi_{off} + \frac{A_D}{A_B + A_D}\varphi_{on}\right) + k_{on}[P_D], \tag{1a}$$

$$\frac{d[P_D]}{dt} = \frac{S\Phi}{V}\left(+\frac{A_B}{A_B + A_D}\varphi_{off} - \frac{A_D}{A_B + A_D}\varphi_{on}\right) - k_{on}[P_D], \tag{1b}$$

where Φ is the flux of photon moles absorbed by the solution per unit area and the square brackets denote concentrations. This flux is related to the total optical density

$(A_B + A_D)$ by [128, 129]:

$$\Phi = I_0\left\{1 - 10^{-(A_D+A_B)}\right\}. \tag{2}$$

By considering $V = S\Delta x$ and incorporating 2 into 1a-b, we have:

$$\frac{d[\mathrm{P}_B]}{dt} = \frac{I_0}{\Delta x}\left(-\frac{A_B}{A_B + A_D}\varphi_{\mathrm{off}} + \frac{A_D}{A_B + A_D}\varphi_{\mathrm{on}}\right)\left\{1 - 10^{-(A_B+A_D)}\right\} + k_{\mathrm{on}}[P_D], \tag{3a}$$

$$\frac{d[\mathrm{P}_D]}{dt} = \frac{I_0}{\Delta x}\left(+\frac{A_B}{A_B + A_D}\varphi_{\mathrm{off}} - \frac{A_D}{A_B + A_D}\varphi_{\mathrm{on}}\right)\left\{1 - 10^{-(A_B+A_D)}\right\} - k_{\mathrm{on}}[\mathrm{P}_D]. \tag{3b}$$

For the low optical density of the solution ($(A_B + A_D) < 0.1$), the exponential term can be expanded up to the first term, thereby linearizing the two equations:

$$\frac{d[\mathrm{P}_B]}{dt} = \ln 10\frac{I_0}{\Delta x}(-A_B\varphi_{\mathrm{off}} + A_D\varphi_{\mathrm{on}}) + k_{\mathrm{on}}[\mathrm{P}_D], \tag{4a}$$

$$\frac{d[\mathrm{P}_T]}{dt} = \ln 10\frac{I_0}{\Delta x}(+A_B\varphi_{\mathrm{off}} - A_D\varphi_{\mathrm{on}}) - k_{\mathrm{on}}[\mathrm{P}_D]. \tag{4b}$$

We shall assume that the Lambert and Beer law holds for both P_B and P_D, i.e.:

$$A_B = \varepsilon_B\Delta x[\mathrm{P}_B], \tag{5a}$$

$$A_D = \varepsilon_D\Delta x[\mathrm{P}_D], \tag{5b}$$

where ε_B and ε_D are the extinction coefficient of B and D states at a given illumination wavelength, respectively. Incorporation of 5a-b into 4a-b gives:

$$\frac{d[\mathrm{P}_B]}{dt} = -\ln 10\varepsilon_B\varphi_{\mathrm{off}}I_0[\mathrm{P}_B] + \ln 10\varepsilon_D\varphi_{\mathrm{on}}I_0[\mathrm{P}_D] + k_{\mathrm{on}}[\mathrm{P}_D], \tag{6a}$$

$$\frac{d[\mathrm{P}_D]}{dt} = +\ln 10\varepsilon_B\varphi_{\mathrm{off}}I_0[\mathrm{P}_B] - \ln 10\varepsilon_D\varphi_{\mathrm{on}}I_0[\mathrm{P}_D] - k_{\mathrm{on}}[\mathrm{P}_D]. \tag{6b}$$

Of note, 6a-b depend on neither the thickness Δx of the volume, nor its exposed surface S, and they therefore apply to any spatial point of the solution where the impinging light intensity is I_0.

We now consider the mass balance condition, that is:

$$\mathrm{P}_0 = [\mathrm{P}_B] + [\mathrm{P}_D]. \tag{7}$$

Equation 4b becomes:

$$\frac{d[\mathrm{P}_D]}{dt} = \ln 10 \varepsilon_B \varphi_{\mathrm{off}} I_0 \mathrm{P}_0 - \{\ln 10 \varepsilon_B \varphi_{\mathrm{off}} I_0 + \ln 10 \varepsilon_D \varphi_{\mathrm{on}} I_0 + k_{\mathrm{on}}\}[\mathrm{P}_D]. \quad (8)$$

Equation 8 admits as solution:

$$[\mathrm{P}_D] = [\mathrm{P}_D]_\infty + ([\mathrm{P}_D]_0 - [\mathrm{P}_D]_\infty) e^{-\frac{t}{\tau}} \quad (9)$$

where τ is the characteristic time of photoswiching, and $[\mathrm{P}_D]_0$, $[\mathrm{P}_D]_\infty$ are the concentrations of D at time zero and at the photosteady state, respectively. We have:

$$\tau = \{\ln 10 \varepsilon_B \varphi_{\mathrm{off}} I_0 + \ln 10 \varepsilon_D \varphi_{\mathrm{on}} I_0 + k_{\mathrm{on}}\}^{-1}, \quad (10)$$

and

$$[\mathrm{P}_D]_\infty = \frac{\ln 10 \varepsilon_B \varphi_{\mathrm{off}} I_0}{\{\ln 10 \varepsilon_B \varphi_{\mathrm{off}} I_0 + \ln 10 \varepsilon_D \varphi_{\mathrm{on}} I_0 + k_{\mathrm{on}}\}} \mathrm{P}_0, \quad (11)$$

By applying Eq. 7, a similar first-order kinetics holds for the P_B state:

$$[\mathrm{P}_B] = [\mathrm{P}_B]_\infty + ([\mathrm{P}_B]_0 - [\mathrm{P}_B]_\infty) e^{-\frac{t}{\tau}}, \quad (12)$$

$$[\mathrm{P}_B]_\infty = \frac{\ln 10 \varepsilon_D \varphi_{\mathrm{on}} I_0 + k_{\mathrm{on}}}{\{\ln 10 \varepsilon_B \varphi_{\mathrm{off}} I_0 + \ln 10 \varepsilon_D \varphi_{\mathrm{on}} I_0 + k_{\mathrm{on}}\}} \mathrm{P}_0. \quad (13)$$

Of note, Eq. 10 expresses the switching rate constant τ^{-1} of the RSFP under illumination at a wavelength λ. As expected for a linear photoprocess, τ^{-1} is directly proportional to the illumination intensity I_0 and admits a non-zero value k_{on} for $I_0 = 0$ due to sole thermal relaxation. 12a–b yield the concentrations of P_B and P_D at the photosteady-state that is inevitably obtained upon prolonged illumination. Equations 10, 11, and 13 can be rewritten in a simplified form by introducing the absorption cross sections σ_B and σ_D, that is:

$$\tau = \{\varphi_{\mathrm{off}} \sigma_B I_0 + \varphi_{\mathrm{on}} \sigma_D I_0 + k_{\mathrm{on}}\}^{-1}, \quad (14)$$

$$[\mathrm{P}_D]_\infty = \frac{\varphi_{\mathrm{off}} \sigma_B I_0}{\{\varphi_{\mathrm{off}} \sigma_B I_0 + \varphi_{\mathrm{on}} \sigma_D I_0 + k_{\mathrm{on}}\}} \mathrm{P}_0, \quad (15)$$

$$[\mathrm{P}_B]_\infty = \frac{\varphi_{\mathrm{on}} \sigma_D I_0 + k_{\mathrm{on}}}{\{\varphi_{\mathrm{off}} \sigma_B I_0 + \varphi_{\mathrm{on}} \sigma_D I_0 + k_{\mathrm{on}}\}} \mathrm{P}_0. \quad (16)$$

The absorption cross-sections are expressed in (cm^2/photons) and are related to the extinction coefficients (units: $\mathrm{M}^{-1}\ \mathrm{cm}^{-1}$) through Avogadro's number N_A according to:

$$\sigma = 1000 \cdot \frac{\ln 10 \varepsilon}{N_A}. \quad (17)$$

In 14–16 the illumination intensity I_0 is expressed in ($photons{\cdot}s^{-1}{\cdot}cm^{-2}$). Commonly, the illumination intensity is expressed in ($kW{\cdot}cm^{-2}$) and conversion is given by:

$$I_0\left(photons \cdot s^{-1} \cdot cm^{-2}\right) = 5.05 \cdot 10^{18} \bullet I_0\left(kW \cdot cm^{-2}\right) \cdot \lambda(nm). \tag{18}$$

Single-molecule behavior at single illumination wavelength and in the absence of irreversible photobleaching The ensemble treatment is immediately extensible to a single molecule level by substituting the concentrations of P_B and P_D states with their probabilities $\mathcal{P}_B$ and $\mathcal{P}_D$. Thus, Eqs. 9 and 12 become:

$$\mathcal{P}_B = \mathcal{P}_{B,\infty} + \left(\mathcal{P}_{B,0} - \mathcal{P}_{B,\infty}\right)e^{-\frac{t}{\tau}}, \tag{19a}$$

$$\mathcal{P}_D = \mathcal{P}_{D,\infty} + \left(\mathcal{P}_{D,0} - \mathcal{P}_{D,\infty}\right)e^{-\frac{t}{\tau}}, \tag{19b}$$

where the pedices have the same meaning, and τ is still expressed by Eq. 14. Experimentally, however, a single molecule is either P_B or P_D. The relevant quantities in this context are τ_B and τ_D i.e. the characteristic survival times of the P_B and P_D states, respectively. Given the first-order kinetics expressed by Eqs. 19a, 19b, it is easy to demonstrate that the characteristic times are:

$$\tau_B = \{\varphi_{\text{off}}\sigma_B I_0\}^{-1}, \tag{20a}$$

$$\tau_D = \{\varphi_{\text{on}}\sigma_D I_0 + k_{\text{on}}\}^{-1}. \tag{20b}$$

Equations 20a, 20b enable straightforward calculation of the photoswitching yields of B and D states by measuring their survival times in single-molecule experiments, as originally reported for Dronpa [115]. Of note, the fractional probability of finding the RSFP in the P_B state is given by:

$$\frac{\tau_B}{\tau_B + \tau_D} = \frac{\{\varphi_{\text{off}}\sigma_B I_0\}^{-1}}{\{\varphi_{\text{off}}\sigma_B I_0\}^{-1}\{\varphi_{\text{off}}\sigma_B I_0\}^{-1}}. \tag{21}$$

Which promptly rearranges to:

$$\frac{\tau_B}{\tau_B + \tau_D} = \frac{\varphi_{\text{on}}\sigma_D I_0 + k_{\text{on}}}{\{\varphi_{\text{off}}\sigma_B I_0 + \varphi_{\text{on}}\sigma_D I_0 + k_{\text{on}}\}}. \tag{22}$$

As expected for an ergodic system, comparison of Eqs. 16 and 22 shows that the ensemble and single-molecule systems are related by:

$$\frac{\tau_B}{\tau_B + \tau_D} = \frac{[P_B]_\infty}{P_0}. \tag{23}$$

Photochromic cycle of an ensemble of switchers in the absence of irreversible photobleaching Let us now consider a full photoswitching cycle focusing on the time evolution of P_B concentration. We shall assume that the protein is initially all in the state P_B. In the first half of the photoswitching cycle, we illuminate at λ_B, where P_B mostly absorbs. Then $B \rightarrow D$ photoswitching occurs, and P_B monoexponentially decays with time constant (Eq. 14):

$$\tau_{B\rightarrow D} = \{\varphi_{\text{off}}\sigma_B(\lambda_B)I_0(\lambda_B) + \varphi_{\text{on}}\sigma_D(\lambda_B)I_0(\lambda_B) + k_{\text{on}}\}^{-1}, \tag{24}$$

down to a concentration given by Eq. 16:

$$[\mathrm{P}_B](\lambda_B) = \frac{\varphi_{on}\sigma_D(\lambda_B)I_0(\lambda_B) + k_{\text{on}}}{\{\varphi_{\text{off}}\sigma_B(\lambda_B)I_0(\lambda_B) + \varphi_{\text{on}}\sigma_D(\lambda_B)I_0(\lambda_B) + k_{\text{on}}\}}\mathrm{P}_0. \tag{25}$$

Next, in the second half of the photoswitching, we illuminate at λ_D, where P_D predominantly absorbs. P_B now grows with time constant:

$$\tau_{D\rightarrow B} = \{\varphi_{\text{off}}\sigma_B(\lambda_D)I_0(\lambda_D) + \varphi_{\text{on}}\sigma_D(\lambda_D)I_0(\lambda_D) + k_{\text{on}}\}^{-1}, \tag{26}$$

up to a concentration:

$$[\mathrm{P}_B](\lambda_D) = \frac{\varphi_{\text{on}}\sigma_D(\lambda_D)I_0(\lambda_D) + k_{\text{on}}}{\{\varphi_{\text{off}}\sigma_B(\lambda_D)I_0(\lambda_D) + \varphi_{\text{on}}\sigma_D(\lambda_D)I_0(\lambda_D) + k_{\text{on}}\}}\mathrm{P}_0. \tag{27}$$

If a second photoswitching cycle follows, P_B will again decay to $[P_B](\lambda_B)$, before rising to $[P_B](\lambda_D)$, and this pattern is going to be conserved across cycles if irreversible photobleaching is absent. Thus, any photoswitching cycle but the first involves toggling P_B between two concentration extremes: $[P_B](\lambda_B)$ and $[P_B](\lambda_D)$. Given the transient nature of the first cycle, the initial P_B concentration is irrelevant. Notably, we may even start by illuminating at λ_D and, apart from the first half-cycle, the following pattern will not change.

Under the reasonable hypothesis that RSFP fluorescence is linearly related to the P_B concentration, the fluorescence photoswitching *contrast* R related to (λ_B, λ_D) is defined by:

$$R = \frac{[\mathrm{P}_B](\lambda_D)}{[\mathrm{P}_B](\lambda_B)}. \tag{28}$$

Computing contrast becomes very simple when one of the switching yields is much larger than the other. We shall assume that $\varphi_{\text{on}} > \varphi_{\text{off}}$, as it occurs in most RSFPs. If, as expected, $\sigma_B(\lambda_D) \ll \sigma_D(\lambda_D)$, Eq. 27 becomes:

$$[\mathrm{P}_B](\lambda_D) \cong \frac{\varphi_{on}\sigma_D(\lambda_D)I_0(\lambda_D) + k_{\text{on}}}{\{\varphi_{on}\sigma_D(\lambda_D)I_0(\lambda_D) + k_{\text{on}}\}}\mathrm{P}_0 = \mathrm{P}_0. \tag{29}$$

That is, reactivation from P_D restores about 100% P_B [130]. In this scenario, R becomes:

$$R = \frac{\{\varphi_{\text{off}}\sigma_B(\lambda_B)I_0(\lambda_B) + \varphi_{\text{on}}\sigma_D(\lambda_B)I_0(\lambda_B) + k_{\text{on}}\}}{\varphi_{\text{on}}\sigma_D(\lambda_B)I_0(\lambda_B) + k_{\text{on}}}. \tag{30}$$

We immediately observe that the contrast *levels off* to a maximum for a strong excitation and/or a very inefficient thermal channel, so to neglect k_{on} compared to the photoinduced rates. We have:

$$R \to R_{\max} = \frac{\varphi_{\text{off}}\sigma_B(\lambda_B) + \varphi_{\text{on}}\sigma_D(\lambda_B)}{\varphi_{\text{on}}\sigma_D(\lambda_B)}. \tag{31}$$

Given the independence of $R_{\max}$ from illumination intensity, it may be easier to compute this parameter from extinction coefficients [131], i.e.:

$$R_{\max} = \frac{\varphi_{\text{off}}\varepsilon_B(\lambda_B) + \varphi_{\text{on}}\varepsilon_D(\lambda_B)}{\varphi_{\text{on}}\varepsilon_D(\lambda_B)}. \tag{32}$$

Equation 32 shows that contrast can be maximized by setting λ_B where the molar absorption of P_D is poor with respect to P_B, i.e. $\varepsilon_B(\lambda_B)/\varepsilon_D(\lambda_B) \gg 1$. For instance, if $\varphi_{\text{on}} \sim 10\varphi_{\text{off}}$, $R_{\max} > 10$ is obtained for $\varepsilon_B(\lambda_B) > 90\varepsilon_D(\lambda_B)$. As previously stated, the reciprocal of the contrast affords the residual fluorescence after a switching-*off* transition.

It is worth noting that excitation to produce fluorescence at the generic wavelength λ_{exc} may -in principle- affect the contrast. This effect is of no concern in positive switchers because excitation is usually carried out at λ_D, thus avoiding the $P_B \to P_D$ conversion. Yet, in negative switchers $\lambda_{\text{exc}} = \lambda_B$, and some *off*-switching is inevitably produced by illuminating the fluorescent state. This means that the fluorescence at the beginning of the *off*-cycle *could be lower* than expected for a protein that is 100% *B* immediately after reactivation, thereby degrading the contrast. Here the critical parameter is the initial $P_B \to P_D$ photoisomerization rate, which under the assumption $[P_B]_0 = P_0$ (Eq. 29) may be approximated by (Eq. 6a):

$$\frac{d[P_B]}{dt} \approx -\varphi_{\text{off}}\sigma_B(\lambda_{\text{ex}})I_0(\lambda_{\text{ex}})P_0. \tag{33}$$

Illuminating for a short time Δt at the beginning of the *off* cycle, $[P_B]$ decays according to the linear law:

$$[P_B](t) = P_0(1 - \varphi_{\text{off}}\sigma_B(\lambda_{\text{ex}})I_0(\lambda_{\text{ex}})\Delta t). \tag{34}$$

And the approximation of little consumption of *B* state and maximum contrast holds for:

$$\Delta t \ll \frac{1}{\varphi_{\text{off}}\sigma_B(\lambda_{\text{ex}})I_0(\lambda_{\text{ex}})}. \tag{35}$$

Now, the signal (in photons) detected by the measurement apparatus in the time Δt can be expressed as:

$$S = \eta \Phi \sigma_B(\lambda_{ex}) I_0(\lambda_{ex}) \Delta t, \tag{36}$$

where η accounts for the collection efficiency, and Φ is the fluorescence quantum yield of the protein. If S_{min} is the minimum number of detected photons to give a meaningful (for example 3 $\times$ the background) signal in the apparatus, we have that the minimum collection time is:

$$\Delta t_m = \frac{S_m}{\eta \Phi \sigma_B(\lambda_{ex}) I_0(\lambda_{ex})}. \tag{37}$$

Considering the condition expressed by Eq. 35, we have:

$$\frac{S_m}{\eta} \ll \frac{\Phi}{\varphi_{off}}. \tag{38}$$

A large Φ/φ_{off} ratio avoids significant photoconversion upon fluorescence excitation on the P_B band and therefore significant loss of contrast between the dark and bright states. Alternatively, co-illumination at λ_D and λ_B before the switching-*off* cycle can be considered, to generate fluorescence from the protein while preventing any $P_B \rightarrow P_D$ photoconversion.

Photochromic cycle of an ensemble of switchers in the presence of irreversible photobleaching Finally, we shall introduce the effect of irreversible photobleaching of the protein. We define the switching fatigue *SWF* from the fluorescence obtained at the beginning of any two consecutive photoswitching cycles which start out from 100% P_B (Eq. 29):

$$SWF = \frac{F(n+1)}{F(n)} = \frac{P_0(n+1)}{P_0(n)}. \tag{39}$$

From SWF, it is easy to compute the % of retained fluorescence after N cycles:

$$\frac{F(N)}{F(0)} = SWF^N. \tag{40}$$

SWF is indeed a critical parameter for any application devised for a given RSFP. A 5% fatigue means that after 45 cycles the fluorescence of the proteins is about 10% of the initial value. If several cycles are needed, as in most super-resolution applications, $SWF > 5\%$ should be avoided and $SWF < 1\%$ should be targeted. If less cycles are required, like in qOLID [132], larger SWF may be tolerated.

Interestingly, irreversible photobleaching is usually well-described by a monoexponential decay of fluorescence over time, which may be interpreted as a first-order

decay kinetics of the global protein:

$$[\mathrm{P}_0](t) = \mathrm{P}_0\left[e^{-\left(\frac{T_B+T_D}{\tau_{bl}}\right)}\right], \tag{41}$$

where T_B, T_D are the time spent to drive one $\mathrm{P}_B \rightarrow \mathrm{P}_D$ (*off*) and one $\mathrm{P}_D \rightarrow \mathrm{P}_B$ (*on*) half-cycles, respectively. The SWF is given by:

$$SWF = \frac{F(n+1)}{F(n)} = \left(e^{-\frac{T_B+T_D}{\tau_{bl}}}\right). \tag{42}$$

In principle irreversible photobleaching may occur from either or both P_B and P_D. Thus, we can introduce the irreversible photobleaching yields $\varphi_{bl,B}$ and $\varphi_{bl,D}$, under the assumption of a linear photoprocess. This leads to a characteristic time of photobleaching given by:

$$\tau_{bl} = \frac{T_B + T_D}{\left\{\varphi_{bl,B}\sigma_B(\lambda_B)I_0(\lambda_B)T_B + \varphi_{bl,D}\sigma_D(\lambda_D)I_0(\lambda_D)T_D\right\}}. \tag{43}$$

For simplicity, let us assume that photobleaching comes only from P_B. Equation 43 becomes:

$$\tau_{bl} = \frac{T_B + T_D}{\left\{\varphi_{bl,B}\sigma_B(\lambda_B)I_0(\lambda_B)T_B\right\}}, \tag{44}$$

and Eq. 42:

$$SWF = \frac{F(n+1)}{F(n)} = \left(e^{-\varphi_{bl,B}\sigma_B(\lambda_B)I_0(\lambda_B)T_B}\right). \tag{45}$$

Now, we could assume that $T_B \approx 3\tau_{B\rightarrow D}$, and that the spontaneous recovery is not really affecting the photoswitching at the selected illuminations. Combination of Eqs. 24 and 45 yields:

$$SWF = \left[e^{-\left(\frac{\varphi_{bl,B}\sigma_B(\lambda_B)}{3\varphi_{\mathrm{off}}\sigma_B(\lambda_B)+3\varphi_{\mathrm{on}}\sigma_D(\lambda_B)}\right)}\right]. \tag{46}$$

This means that SWF is ideally independent of illumination intensity. This result is quite general and applies also if irreversible photobleaching comes from P_D is considered (not shown). Indeed, photobleaching is a linear photoprocess likewise photoswitching, and less photobleaching per unit time comes at the price of a lower number of photocycles per unit time, either. The only relevant parameter to determine SWF are the ratios between the irreversible photobleaching and reversible photoswitching yields. A good rule of thumb is obtained by assuming $\varphi_{\mathrm{off}}\sigma_B(\lambda_B) \gg \varphi_{\mathrm{on}}\sigma_D(\lambda_B)$ in

Eq. 46 and expanding to first term:

$$SWF \approx 1 - \frac{\varphi_{bl,B}}{3\varphi_{\text{off}}}. \tag{47}$$

Since φ_{bl} in FPs is usually in the range 10^{-6}-10^{-4}, φ_{off} higher than 10^{-3} will afford RSFPs with good to excellent resistance to photobleaching.

In spite of the ideal independence from the illumination intensity, the measured values of SWF are often context-dependent, on account of the rather different experimental conditions which may involve the characterization of RSFPs in solution, or immobilized in a gel, or expressed in bacteria (not to say about illumination conditions, buffering pH or temperature). Thus, it can be useful to compare the *relative* resistance to photobleaching of one switcher X with respect to an archetype RSFP with similar spectral characteristics (ref) as measured in the same experimental conditions. In such a case, we may introduce the PR ratio as:

$$PR = \frac{\ln(SWF_{\text{ref}})}{\ln(SWF_X)}. \tag{48}$$

Inspection of Eq. 40 immediately shows that PR represents the ratio between the switching cycles N_X and N_{ref} needed to decrease the fluorescence of the two RSFPs by the same amount, that is:

$$PR = \frac{N_X}{N_{\text{ref}}}. \tag{49}$$

A $PR > 1$ implies that the variant X is more resistant to photobleaching than *ref*, while the opposite holds true for $PR < 1$.

3.2 Negative RSFPs with "GFP-like" chromophore

The "archetype" family of RSFPs comprises "GFP-like" negative switchers, i.e. proteins possessing a *p*-HBI chromophore that has not undergone further oxidation after its maturation from the original tripeptide (§1.1). These blue-to-yellow variants are well-characterized from the photophysical point of view, and they have found widespread applications in non-conventional and super-resolution imaging techniques (§3). In the next sections, we describe their photoswitching mechanism (§2.2.1) and ground-state isomerization to restore the *on* state (§ 2.2.2). In Sects. 2.2.3–2.2.6 and Tables 1, 2 and 3 we describe the main properties of several representative variants, grouped into families according to their common ancestor protein. Of note, where possible, we used reported comparative photofatigue data to calculate the *PR* ratio (§ 2.1.3.4, Eq. 48) with respect to rsEGFP2 ($PR = 1$).

3.2.1 Photoswitching mechanism

Scheme 10 summarizes the photoswitching mechanism in negative switchers consid-

Table 1 Negative switchers from *av*GFP of *Aequorea Victoria* (wtGFP in the text). Proteins are ordered according to increasing maximum excitation wavelength in the *on* state

Name	λ_{max} *ON* ex/em (nm)	ε*ON* ($\times 10^3$)[a]	ϕ_F	Brightness relative to EGFP[b]	λ_{max} OFF (nm)	ε *OFF* ($\times 10^3$)[a]	pK_a *cis*	λ_{off} /λ_{on} (nm)	ϕ_{off} $\times 10^3$	ϕ_{on} $\times 10$	$\tau_{1/2}$, thermal, (min)	Contrast[c]	PR[d]	Refs
modBFP	390/455	27.0	0.33	0.26			5.5	405/514						[150]
rsEGFP2[e]	478/503	61.3	0.30	0.56	408	25.8[f]	5.8	488/405	16.5[g]	3.3[g]	192[f]	57[g]	1[h]	[124]
rsFolder[i]	477/503	51.6	0.25	0.39	413[e]	38.5[f]	5.5	488/405	21	4.4	2890	26		[148]
rsFolder2j	478/503	44.0	0.23	0.30	413[e]	42.4[f]	5.5	488/405	20	2.8	1050	40		[148]
rsEGFP2-V151A	483/?	62.2	0.26	0.48	410	32.3	6.4	488/405	11	2.5	2245	119		[131]
rsEGFP2-V151L	483/?	68.3	0.28	0.57	417	33.3	5.7	488/405	6.5	2.9	416	15		[131]
rsFolder2-V151A	484/?	61.1	0.21	0.38	410	32.3	6.4	488/405	14	2.2	3118	125		[131]
rsFolder2-V151L	483/?	74.4	0.45	1.00	418	37.0	5.9	488/405	6.5	2.7	540	15		[131]
WQ	476/504	57.4	0.45	0.77	403	28.6	6.1	488/405	2.7	0.7	4.8	5	1	[112]
WQT	482/505	64.3	0.71	1.36	405	27.6	5.7	488/405	1.1	0.25	8.2	4	0.72	[112]
Mut2Q	496/507	54.0	0.28	0.45	407	27.2	6.0	478/405	4.7	0.26	25	3.9		[117]
rsGreen1	486/509	58.0	0.42	0.73	396	19.5	5.9	488/405	4.2	1.4		111	0.36	[125]
rsGreen0.7	487/511	62.0	0.40	0.74	396	20.4	6.7	488/405	2.6	1.2		18	0.33	[125]
rsGreen0.7b	489/511	53.0	0.43	0.74	396	19.7	6.7	488/405	5.3	1.6		333	0.55	[125]
rsGreen0.8	487/511	61.0	0.38	0.69	396	18.7	6.7	488/405	3.0	1.5		20	0.30	[125]
rsGreen0.9	485/509	66.0	0.41	0.81	396	20.5	5.7	488/405	3.8	1.3		111	0.48	[125]
rsGreenF	485/511	52.0	0.39	0.60	390	18.2	6.7	488/405	8.7	1.8		333	0.54	[125]

Table 1 (continued)

Name	λ_{max} *ON* ex/em (nm)	εON ($\times 10^3$)[a]	ϕ_F	Brightness relative to EGFP[b]	λ_{max} OFF (nm)	ε *OFF* ($\times 10^3$)[a]	pK_a *cis*	λ_{off} /λ_{on} (nm)	ϕ_{off} $\times 10^3$	ϕ_{on} $\times 10$	$\tau_{1/2}$, thermal, (min)	Contrast[c]	PR[d]	Refs
rsEGFP	493/510	47.0	0.36	0.50	396		6.5	488/405	5.5[k]	1.7[j]		333[k]	0.57	[147]
EYQ1	510/524	73.0	0.72	1.56	414	23	6.9	514/405	0.18	0.6	27	4.2	0.25	[117]

[a] In $M^{-1}cm^{-1}$

[b] EGFP brightness ($\varepsilon \times \phi_F$) is set to 33,540 M^{-1} cm^{-1}

[c] Contrast is defined as the ratio between fluorescence intensities before and after switching off

[d] For definition of PR see Eq. 48. We adopted: PR = 1 for rsEGFP2

[e] Ref. [131]. reports $\phi_{off} = 9.3 \times 10^{-3}$, $\phi_{on} = 2.3 \times 10^{-1}$ and contrast = 43; ref. [108] reports $\phi_{off} = 4.0 \times 10^{-2}$ and $\phi_{on} = 4.0 \times 10^{-1}$; ref [141] reports $\phi_{off} = 0.1 \times 10^{-3}$ and $\phi_{on} = 1.8 \times 10^{-1}$; ref. [151] reports a contrast of 20

[f] From [131]

[g] From [148]. Ref. [125] reports $\phi_{off} = 8.9 \times 10^{-3}$, $\phi_{on} = 1.2 \times 10^{-1}$

[h] The absolute value of photoswitching fatigue (SWF) of rsEGFP2 is 0.033% from [124]

[i] Ref. [131] reports $\varepsilon = 71.9$, $\phi_{off} = 7.3 \times 10^{-3}$, $\phi_{on} = 2.4 \times 10^{-1}$ and contrast = 20

[j] Ref. [131] reports $\varepsilon = 62.2$, $\phi_{off} = 0.11 \times 10^{-3}$, $\phi_{on} = 2.5 \times 10^{-1}$ and contrast = 46

[k] From [125]

Table 2 Negative switchers from 22G of *Echinophyllia sp.* SC22 and from cFP484 of *Clavularia sp.* In both groups, proteins are ordered according to increasing maximum excitation wavelength of the *on* state

Name (T = tetramer)	λ_{max} *ON* ex/em (nm)	ε*ON* ($\times 10^3$)[a]	ϕ_F	Brightness relative to EGFP	λ_{max} *OFF* (nm)	ε*OFF* ($\times 10^3$)[a]	pK_a *cis*	λ_{off} /λ_{on} (nm)	$\phi_{off} \times 10^3$	$\phi_{on} \times 10$	$\tau_{1/2}$, thermal, (min)	Contrast	PR[b]	Refs
From cFP484 of *Clavularia sp.*														
mTFP0.7	453/488	60.0	0.50	0.89			4.0	458/405			5.3			[161]
GMars-Q	470/494	38.6	0.64	0.74	380		6.1	488/405			~ 120			[127]
GMars-T	476/498	55.0	0.53	0.87			4.7	488/405					0.6	[162]
From 22G of *Echinophyllia sp. SC22*														
bsDronpa	460/504	45.0	0.50	0.67	385	26		488/405			54	17	0.07	[163]
Dronpa-2[c]	489/515	56.0	0.28	0.47				488/405	47		0.5			[164]
Dronpa-3	489/515	58.0	0.33	0.57				488/405	5.3					[164]
rsFastLime	496/515	39.1	0.77	0.90	384[d]	23.5[d]		488/405	3.5[e]		8	67	0.02[d]	[158]
Dronpa[f]	503/517	95.0	0.85	2.40	390	23	5.3	488/405	0.07	3.7	840	9.3[g]	0.002[d]	[100]
ffDronpa	503/517	105.0	0.75	2.62	~ 380	22	5.0	488/405	0.07	1.7	840	25.2		[103]
ffDronpa-F	503/517	77	0.69	1.6				488/405	0.07					[165]
rsKame	503/517	72.0	0.86	1.84					0.08[e]		1600[e]			[160]
pcDronpa (T) GS[h]	505/517	115	0.85	2.9	~ 380	19	5.5	488/405	0.0056	0.92		3.67		[103]
pcDronpa (T) OS[h]	569/581	75	0.68	1.5			6.3	561						[103]
pcDronpa2 (T) GS[h]	504/515	100	0.83	2.5	~ 380	20	5.8	488/405	0.013			5.57		[103]

Table 2 (continued)

Name (T = tetramer)	λ_{max} *ON* ex/em (nm)	ε*ON* ($\times 10^3$)[a]	ϕ_F	Brightness relative to EGFP	λ_{max} *OFF* (nm)	ε*OFF* ($\times 10^3$)[a]	pK_a *cis*	λ_{off} /λ_{on} (nm)	$\phi_{off} \times 10^3$	$\phi_{on} \times 10$	$\tau_{1/2}$, thermal, (min)	Contrast	PR[b]	Refs
pcDronpa2 (T) OS[h]	569/583	105	0.68	2.1			6.1	561						[103]
PDM1-4 (T)	503/517							488/405						[166]

[a] In $M^{-1}cm^{-1}$
[b] For definition of PR see Eq. 48. We adopted: PR = 1 for rsEGFP2
[c] Also known as Dronpa-M159T
[d] From [163]
[e] From ref. [144]
[f] Ref. [163] reports $\varepsilon = 125$, $\phi_F = 0.68$; ref [103] reports $\phi_F = 0.76$, $\phi_{off} = 0.16 \times 10^{-3}$, $\phi_{on} = 1.6 \times 10^{-1}$; ref [167] reports $\varepsilon = 94.1$, $\phi_F = 0.67$, $\phi_{off} = 0.3 \times 10^{-3}$, $\phi_{on} = 7.0 \times 10^{-1}$
[g] From ref. [151]; ref. [168] reports 14.5; ref. [103] reports 38.4; ref. [163] reports 17
[h] GS = Green State; OS = Orange State

Table 3 Negative switchers from EosFP of *Lobophyllia hemprichii*. Proteins are ordered according to increasing maximum excitation wavelength of the *on* state

Name	λ_{max} *ON* ex/em (nm)	εON ($\times 10^3$)[a]	ϕ_F	Brightness relative to EGFP	pK_a *cis*	$\lambda_{off}/\lambda_{on}$ (nm)	$\phi_{off} \times 10^3$	$\phi_{on} \times 10$	$\tau_{1/2}$, thermal, (min)	Contrast	PR[b]	Refs
Skylan-S	499/511	152.4	0.64	2.9					139	18.3	2.7	[168]
Skylan-NS	499/511	133.8	0.59	2.3	5.8				70	34.2	0.035	[151]
mEosFP M159A	487/512	98.6	0.52	1.53	4.3	488/405	2.6	1.5				[101]
mGeos-E	501/513	69.6	0.75	1.54	6–6.5	488/405			848		0.0025	[102]
mGeos-M	503/514	51.6	0.85	1.30	4.5–5	488/405			169		0.0019	[102]
mGeos-C	505/516	77.0	0.81	1.84	6	488/405			223		0.001	[102]

[a] In $M^{-1} cm^{-1}$

[b] For definition of PR see Eq. 48. We adopted: PR = 1 for rsEGFP2

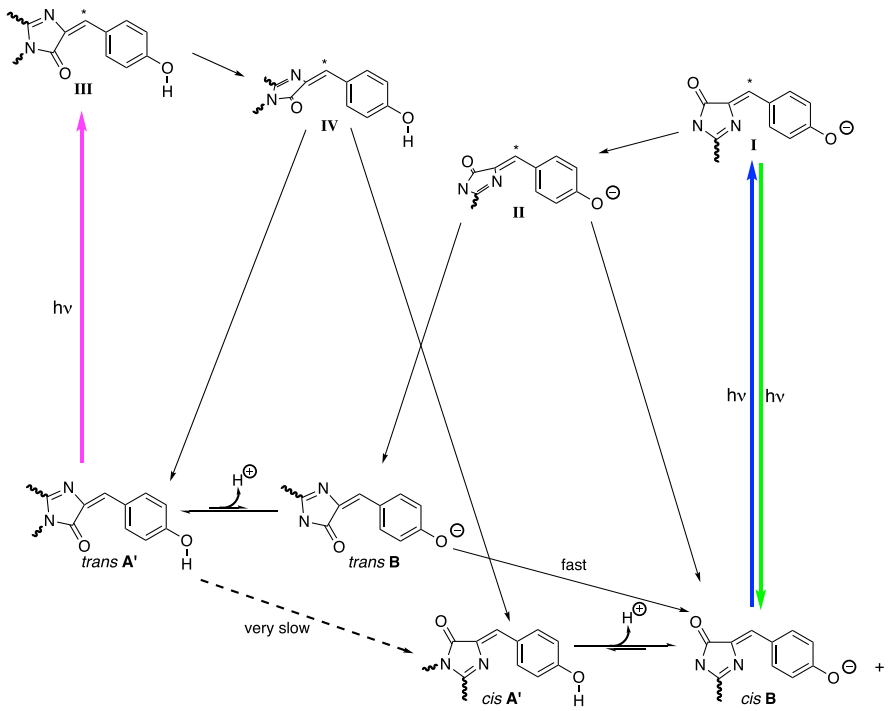

Scheme 10 General overview of photoswitching in negative RSFPs. Natively, the *p*-HBI chromophore equilibrates between the *cis* **B** and *cis* **A'** states, although the former is much more populated at physiological pH given the $pK_a < < 7$. Photoexcitation of *cis* **B** (blue arrow) to its F–C state (**I**) yields fluorescence by radiative decay (green arrow). Yet, some **I** undergo I-twisting to give intermediate **II**. **II** can evolve either back to *cis* **B**, or -through a full rotation about the I-bond- to *trans* **B**. The *trans* chromophore has $pK_a > > 7$, and *trans* **B** is readily converted to *trans* **A'**, which identifies with the *off* state. Photoexcitation of *trans* **A'** at a shorter wavelength than for *cis* **B** (purple arrow) leads to its F–C excited form (**III**) which efficiently undergoes twisting to generate the intermediate **IV**. By internal conversion, IV can either go back to *trans* **A'** or evolve to *cis* **A'**, which rapidly restores the *on* state, *cis* **B**. Of note, *trans* **B** admits a fast thermally-activated decay to *cis* **B**, whereas the thermal channel from *trans* **A'** to *cis* **A'** is much more slower. As a result, the kinetics of the thermal *off* → *on* decay is dependent on the relative populations of *trans* **A'** and **B**, and therefore upon the pH of the solution

ering both the chromophore isomerization and protonation state of the chromophore.

The native (also referred to as "resting") *p*-HBI chromophore is characterized by a *cis* configuration [121] and is usually deprotonated around physiological pH on account of a pK_a well below pH 7 [112, 117]. According to the chromophore nomenclature (§1.3), this corresponds to the **B** state, and for more clarity will be henceforth denoted as *cis* **B**. In negative RSFPs, *cis* **B** is fluorescent and embodies the bright (*on*) state (Fig. 4a and Scheme 10). Apparently, reported negative RSFPs do not show thermodynamic coupling between the *p*-HBI and another internal protonatable residue, and *cis* **B** exchanges proton only with the *cis* **A'** state (Schemes 7 and 10), which is usually non-fluorescent. Several negative switchers exhibit $pK_a < < 7$ (Table 1), and therefore populate mostly *cis* **B** at neutral pH. Excitation of *cis* **B** does not produce only fluorescence but also photoisomerizes *p*-HBI from *cis* to *trans* geometry, switching

off the fluorescence on account of a protonation effect. Indeed, upon isomerization the pK_a of *p*-HBI rises significantly above neutrality [116, 117], and the chromophore is thermodynamically confined to *trans* **A'**, which is non-fluorescent analogously to *cis* **A'**. Owing to the protonation and its related change of π-conjugated electron system, **B** is usually 80–120 nm red-shifted as compared to *trans* **A'** (Table 1). Upon excitation, *trans* **A'** promptly undergoes *trans* → *cis* photoisomerization coupled with deprotonation (Scheme 10). Interestingly, in the deeply studied negative switcher Dronpa from *Pectiniidae*, the illumination of *cis***A'** yields ESPT in about 14 ps, but lacks the photoconversion capability [115]. This behavior has been observed also by us in yellow EYQ1 [117] and green WQ [112] from *Aequorea*.

In negative RSFPs, the *off* → *on* photoswitching quantum yield (φ_{on}) is usually comparable with the quantum yield (Φ_{flu}) of fluorescent emission (Tables 1, 2 and 3). Instead, the quantum yield of *on* → *off* transition (φ_{off}) is usually one or two orders of magnitude lower (Tables 1, 2 and 3), witnessing a less efficient isomerization pathway at the excited state. So far, only the *off* → *on* photoisomerization has been investigated by ultrafast spectroscopy methods (vide infra). Indeed, the high φ_{on} values facilitate the detection of photoswitching signals, which are otherwise hard to detect for yields < 0.1 particularly when electronic spectra are broad and display overlapping peaks [133].

Early ultrafast studies prompted some debate over the sequence of intra-molecular events during the switching process [118, 134, 135]. Yet, multiple techniques including time-resolved fluorescence, fs/ns-Transient Absorptions, Time-Resolved Infrared spectroscopy and serial femtosecond crystallography applied to Dronpa derivatives [109, 136–138], rsEGFP2 [108] and IrisFP [139] have later convincingly demonstrated that *trans* → *cis* isomerization occurs in about 3–20 ps time and *precedes* a ground state deprotonation (Scheme 10). Proton loss occurs in the μs-ms time range and may involve multiple steps or populations (Scheme 11) [108, 140, 141]. Chromophore isomerization is intimately governed by the multidimensional potential energy surfaces explored at both excited and ground states. Indeed, a recent study pivoted on time-resolved multiple-probe infrared spectroscopy highlighted that the newly formed *cis* chromophore of the negative switcher rsEGFP2 reaches its final position in the protein pocket within 100 ps after several intermediate steps, including conformational rearrangements in the chromophore pockets occurring after *trans* → *cis* photoisomerization but before protonation (Scheme 11). The timescales of the first steps of photoisomerization are very close to those observed for *p*-HBDI (§1.2), thus reaffirming the intrinsic ability of *p*-HBI to twist at an excited state and be channeled to a change of its diastereisomeric configuration. Nonetheless, serial femtosecond crystallography on a rsEGFP2 analog with chlorine-substituted *p*-HBI have demonstrated that twisting follows a HT mechanism [142] instead of an OBF as suggested for the isolated chromophore (§1.2). Competition between the almost isovolumetric HT *trans* → *cis* mechanism and other non-isovolumetric deactivation processes may explain the surprising inverse proportionality between the available binding pocket volume and the efficiency of *on*-switching observed in a series of rsEGFP2 variants [131]. The interested reader is referred to the excellent review by Tang and Fang for a comprehensive account of ultrafast characterization of RSFPs photoswitching [143].

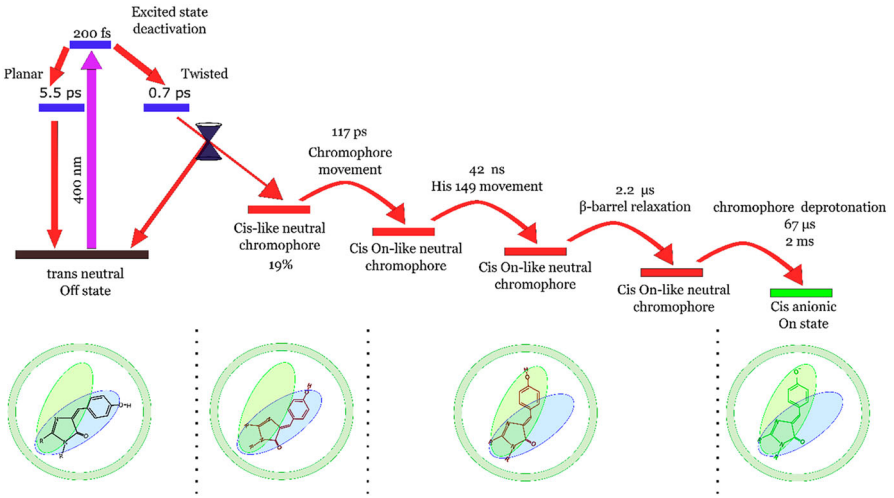

Scheme 11 *Off*-to-*On* Photoswitching Mechanism for negative switching rsEGFP2. Upon excitation at the wavelength of *trans* **A'** of rsEGFP2, the protonated *p*-HBI chromophore reaches the excited state, and within a few fs may evolve to a twisted state. From there, the chromophore undergoes internal conversion to a *cis*-like neutral ground state which, through a series of progressively slower steps, ends up in the *cis* **B** (*on*) state. Figure reprinted with permission from Ref. [141]. Copyright 2022 American Chemical Society

3.2.2 Thermal recovery from *trans* state

Similarly to *p*-HBDI [10], negative switchers isomerize thermally from the *trans* (*off*) state to *cis* (*on*) state in timescales ranging from second to hours (Table 1). The thermal channel owes to the higher free energy of *trans p*-HBI as compared to the *cis* conformer (4 kcal/mol for Dronpa and its derivative rsFastlime, as estimated by molecular dynamics simulations [144]). Yet, the change in protonation state upon photoisomerization in negative RSFPs somewhat complicates the scenario. This topic has been pioneered by Bizzarri et al. in a 2010 paper dealing with the negative yellow switcher EYQ1 and the green switcher Mut2Q [117]. By pH-jump/absorption spectroscopy measurements, the authors found that *trans* **A**' and *trans* **B** forms relax, respectively, to *cis* **A'** and *cis* **B** according to two distinct first-order kinetics [117]. More precisely, the rate constant for the relaxation of the protonated chromophore (*trans* **A'** → *cis* **A'**, $k_{A'} \sim 10^{-4} \div 10^{-5}$ s^{-1}) was found 3–4 orders of magnitude smaller than for the decay of the deprotonated form (*trans* **B** → *cis* **B**, $k_B \sim 10^{-1} \div 10^{-2}$ s^{-1}) [117]. As suggested for *p*-HBDI [63], the lower energy barrier between *trans* **B** and *cis* **B** may be related to the electron delocalization occurring in the anionic chromophore, which enables a partial transfer of the double- bond character from the I-bond to the P-bond. This partial electronic transfer should favor an HT isomerization mechanism, as proposed by Morozov for the Dronpa-2 derivative [145]. Yet other authors have proposed the ground-state isomerization of Dronpa to occur via an OBF mechanism [134]. Beside the electronic state, direct dependence between the protein flexibility and the activation energy barrier has been observed [144], witnessing once more the relevance of protein flexibility for photochromic properties [146]

Assuming two thermal isomerization channels as in Scheme 10, the experimental rate constant is given by the average of $k_{A'}$ and $k_{B'}$ values, each weighted by the molar fraction of the related *trans* state [117]. If pK_T is the pK_a of *trans* p-HBI, we have:

$$k(pH) = \frac{k_{A'} + k_B 10^{(pH-pK_T)}}{1 + 10^{(pH-pK_T)}}. \tag{50}$$

Equation 50 pinpoints the crucial role of pK_T in determining the spontaneous recovery of a negative RSFP endowed with a *p*-HBI chromophore. For example, the pK_T of EYQ1 is 9.87 [117], and at biological pH the thermal kinetics of this protein is largely dominated by the *trans* **A'** → *cis* **A'** reaction. Nonetheless, raising the pH would lead to a larger population of *trans* **B**, accelerating the thermal decay because the *trans* **B** → *cis* **B** ground-state isomerization becomes progressively more active. $k_{A'}$ sets the lower limit of recovery rate, which should always be tuned to the desired imaging application.

3.2.3 Negative RSFPs from wtGFP of *Aequorea victoria*

The main properties of most representative variants are reported in Table 1

rsEGFP variants rsEGFP2 is a green variant from *Aequorea* that has been developed by the Jakobs group in 2012 and early became the "gold standard" of negative switchers on account of its striking fast photoconversion, high contrast, excellent fatigue resistance and thermal stability in the *trans* state [124]. rsEGFP2 is the refinement of a first negative switcher, rsEGFP, developed by the same group in 2011 from the monomeric "enhanced" fluorescent protein EGFP (F64L/S65T/A206K wtGFP) through site-directed and error-prone mutagenesis [147]. rsEGFP adds four mutations to EGFP (Q69L/V150A/V163S/S205N), maintaining the same spectroscopic characteristics, although its brightness is 50% of its parent non-switching protein (Table 1). *cis* **B** absorbs at 493 nm, emitting at 510 nm. Yet, the rather high pK_a (6.5) implies a minor *cis* **A'** band at physiological pH. Upon *off*-switching, rsEGFP yields *trans* **A'**, which absorbs at 396 nm (Table 1). rsEGFP displays a striking contrast ratio > 300 and impressive resistance to photobleaching [147].

Compared to rsEGFP, rsEGFP2 introduces the T65A mutation and restores the S205 of EGFP, being therefore F64L/S65A/Q69L/V150A/V163S A206K wtGFP. The absorption and emission of *cis* **B** in rsEGFP2 are blue-shifted by 15 nm compared to rsEGFP, whereas *trans* **A'** is red-shifted by 12 nm (Table 1). As switcher, rsEGFP2 is about ~ 100 times faster and twice as much resistant to photobleaching compared to rsEGFP, while maintaining almost the same brightness and losing only a little in terms of contrast. Thermal decay occurs in a few hours at neutral pH. Detailed structural studies have demonstrated that *trans* **A'** *p*-HBI splits into two different conformers (*trans1* and *trans2*), which display different φ and τ dihedral angles, protein environment and H-bonding network (Fig. 7) [131, 140]. More specifically, *trans2* shows a nearly planar *p*-HBI that is H-bonded to H149 (H148 in the original sequence of wtGFP). Vice-versa, *p*-HBI in *trans1* assumes a distorted geometry and is H-bonded to a water molecule, while H148 establishes an H-bond with Y146.

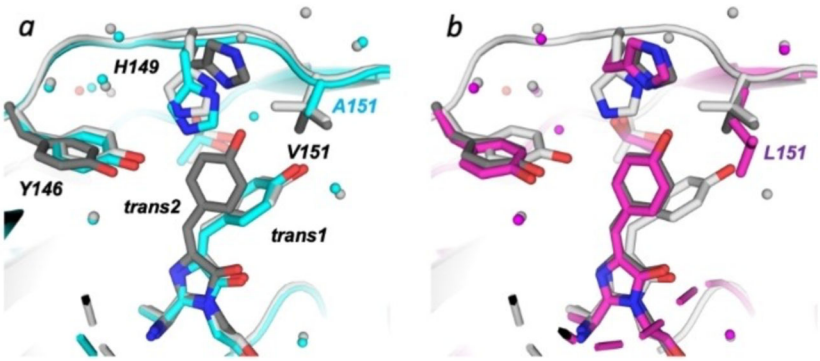

Fig. 7 Structures of *trans* **A'** (*off*) conformers of rsEGFP2 and its V151A and V151L variants solved from RT SFX data. Off-state models of **a** rsEGFP2-V151A (cyan; PDB entry 7O7X) and **b** -V151L (purple; PDB entry 7O7W) variants are superimposed on the model of parental rsEGFP2 in the off-state solved from RT SFX data (PDB entry 7O7U), featuring *trans1* in light grey and *trans2* in dark grey. Reprinted with permission from [131]

This conformational heterogeneity was eliminated by mutating V151, a residue that needs to retract to enable *cis* ↔ *trans* isomerization of the chromophore [108]. In the V151A and V151L variants of rsEGFP2 the chromophore adopts uniquely the *trans1* or *trans2* conformation, respectively (Fig. 7) [131]. rsEGFP2 V151A exhibited higher contrast compared to parent protein rsEGFP2 (2.6x), whereas the opposite was demonstrated for rsEGFP2 V151L (0.33x). The photophysical characterization suggested that this difference does not stem from the photoswitching yields -which are similar in all cases- but rather from a lower extinction coefficient of the *trans1* **A'** state at the fluorescence excitation wavelength (488 nm) [131], as also predicted by Eq. 32. This effect was in turn attributed to a blue-shift of *trans1* **A'** (397 nm) with respect to *trans2* **A'** (405 nm), which was fully accounted for by the structure-dependent different electron delocalization of the two *p*-HBI conformers, as indicated by quantum chemistry calculations [131].

rsFolder variants El Khatib and co-workers pursued a fully rational design of reversible photoswitching properties [148]. Starting from Superfolder-GFP (a robustly folded version of wtGFP that folds well even when fused to poorly folded polypeptides [149]) they incorporated in the sequence the four crucial point mutations that allowed evolving EGFP into rsEGFP2 (T65A, Q69L, V163S, A206K [124]), affording the negative switcher rsFolder [148]. rsFolder exhibits almost the same spectral properties as rsEGFP2, being also similar in terms of photoswitching yields, albeit rsEGFP2 displays twice as much contrast (Table 1). Yet, the thermal *off* → *on* rate constant of rsFolder is 15-fold smaller than rsEGFP2 at neutral pH, making this protein one of the most stable RSFPs in the dark state. X-ray inspection of the crystal structure indicated that *trans p*-HBI in the chromophore's cavity adopts an arrangement almost mirroring that of the *cis* configuration, thereby remaining tightly attached to the barrel

scaffold [148]. This likely explains the exceptional stability of the *off* state. Mutation of the T146 residue, which stabilizes the *trans* chromophore in rsEGFP2, to Alanine afforded rsFolder2 (T146A rsFolder). rsFolder2 recovered most of the high switching contrast of rsEGFP2 at the price of a two-fold faster thermal *off* → *on* recovery from *trans* state. Of note, the similarity of rsFolder2 to rsEGFP2 was not restricted to the macroscopic photophysical behavior, since also rsFolder2 exhibited a heterogeneous population of *trans1* and *trans2* **A'** chromophore in the *off* state [148]. Analogously to rsEGFP2, the introduction of V151A or V151L in the rsFolder2 sequence led to the selective stabilization of *trans1* or *trans2* conformer, respectively [148].

rsGreen variants In 2015 the Dedecker group developed a palette of negative *Aequorea* RSFPs starting from rsEGFP by a mix of rational and random mutagenesis [125]. Optimization of the brightness afforded rsGreen0.7, which was further optimized for fast photoswitching and low contrast and fatigue resistance to yield four more variants (rsGreen0.8, rsGreen0.9, rsGreen1, and rsGreenF, Table 1). When expressed in cells, these FPs displayed a 2.5–4.5-fold improved brightness compared to rsEGFP, and 1.5 to threefold compared to rsEGFP2, under 488 nm illumination [125]. In rsGreens variants, the absorption of *cis* **B** and *trans* **A'** states shows little variation [125]. Yet, the pK_a of some rsGreens (rsGreen0.7, rsGreen0.7b, rsGreen0.8, and rsGreenF) is close to neutrality, implying that a significant proportion of the *on*-state resides in *cis* **A'**. Determination of photoswitching yields showed a wide oscillation of φ_{off}, which ranges from almost the same value as for rsEGFP2 (in rsGreenF) to a reduction of about 3.4-fold (in rsGreen0.7) [125]. Conversely, φ_{on} varies in the narrow 1.2–1.8 range where also rsEGFP and rsEGFP2 fall. As expected for a nearly constant φ_{on} and similar spectral features, the contrast ratio R was proportionally related to φ_{off} (Eq. 31). Analogously, faster *off*-switchers appeared more resistant to irreversible photobleaching, as the ratio between φ_{bl} and φ_{off} decreases (Eq. 44). Detailed X-ray analysis of the *on* and *off* states showed *trans p*-HBI is significantly non-planar and is stabilized by the H-bond with a surrounding water molecule, similarly to what found in other negative switchers [125]. Comparison with the structures of non-switching EGFP and sfEGFP strongly posited the relevance of mutations Q69L and V150A to accommodate sufficient space for *cis* ↔ *trans* isomerization. In the following paper, the Dedecker group reported that the fusion of rsGreen1 and rsGreenF with a small binding peptide, named Enhancer, modulated the spectral as well as the switching properties [152]. Enhancer stabilizes preferentially a fast switching-*off* population of the proteins, hampering the progressive conversion of the protein to a slow switching-*off* population that is observed in the original protein.

E222Q (Q-RSFPs) variants In 2010, Bizzarri and coworkers showed that the introduction of the E222Q mutation conferred negative photoswitching behavior in non photoswitching proteins, generating the green switchers Mut2Q and the yellow switcher EYQ1 [117, 153]. This finding also rationalized previous observations on the peculiar photophysics of E222Q mutants [134–137]. Two more green switchers, WQ and WQT, have been later evolved from EGFP by just one (WQT: E222Q EGFP) or two (WQ: T65S E222Q EGFP) mutations. These proteins family display moderate

to fast photoswitching rates, although with a much lower contrast and thermal recovery as compared to rsEGFP2 (Table 1).

The recurrent effect of E222Q mutation in a variety of *Aequorea* FPs hints at a common mechanism by which this mutation unleashes negative photoswitching behavior in otherwise non-photoswitching proteins. In general, understanding the influence of specific amino acids in the vicinity of the chromophore on photoswitching properties is a challenging task. This challenge is particularly pronounced when addressing the switching *off* of negative switchers, in which this process is a relatively rare outcome of photoexcitation ($\varphi_{off} \sim 10^{-2}$–$10^{-3}$). Boxer and co-workers [154–156] have built a model for the chromophore electronic structure which very effectively explains various correlations among spectroscopic and photophysical properties of FPs. Previous studies have pointed out how different environments influence the electronic structure of the chromophore by affecting the interplay between two resonance structures, a benzenoid structure (P-form) with a formal charge on the phenolic oxygen and a single P-bond and quinonoid structure (I-form) with a formal charge on the imidazolidinone carbonyl oxygen and a single I-bond [42, 157]. The unifying model of Boxer and coworkers introduces a single parameter, namely the driving force, which is the energy difference between these two resonant structures in various environments. Using this parameter, they were able to quantitatively explain the correlations among absorption maxima, Stokes shifts, vibronic structures and extinction coefficients. In addition, they assumed that *cis* ↔ *trans* photoisomerization through the I-twist pathway would be favored whenever the P-form is more stabilized.

The effect of the E222Q mutation cannot be rationalized in terms of this model because the introduction of this mutation has no effect on the spectroscopic properties of the protein. Yet, in a recent paper we hypothesized that glutamine at position 222 has a unique role in stabilizing the intermediate twisted state during *cis–trans* photoisomerization [112]. We performed molecular dynamics simulations of the protein dynamics following excitation, using an ad-hoc force field reproducing the excited-state potential energy surface of the chromophore. The infrequent nature of the photoisomerization process required the simulation of several (1200) excited-state trajectories starting from configurations obtained by previously performed ground-state MD simulations. During the chosen excited-state simulation time of 0.5 ns, most of the trajectories sampled regions close to planarity, while a fraction (between 5 and 25% depending on the mutant) underwent twisting around the P or the I bond (Fig. 8a). The presence of Q222 led to more frequent I-twisting in the WQ mutant (F64L/E222Q wtGFP). This outcome could be explained thanks to the ability of the NH2 of Q222 amide to form two simultaneous H-bonds, one with the nitrogen in the imidazolidinone ring and the other with the neighboring Ser205 side chain (Fig. 8b). These two H-bonds can be simultaneously established only in the I-twisted intermediate, thus selectively stabilizing this configuration, whereas they are absent when the amide is not present (as in the E222 case).

3.2.4 Negative RSFPs from 22G of*Echinophyllia* sp. SC22

The main properties of most representative variants are reported in Table 2

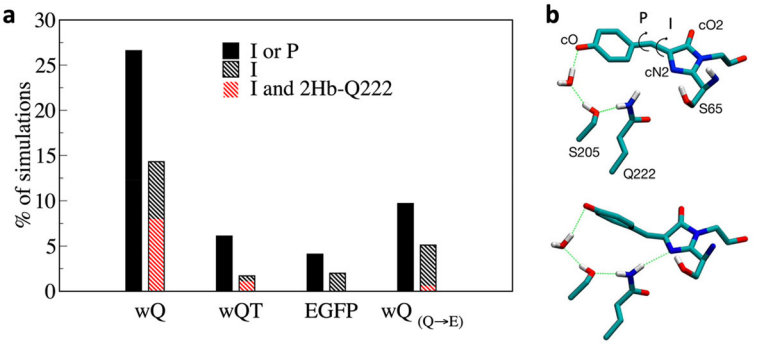

Fig. 8 Role in E222Q mutation in unleashing photochromic behavior in otherwise non-switching *Aequorea* FPs. **a** Percentage of 0.5 ns excited-state MD simulations leading to P or I twisting event (solid black), I twisting event (shaded black and red), and I twisting event accompanied by 2Hb-Q222 conformation (shaded red) in the examined mutants. wQ: F64L/E222Q wtGFP; wQT: F64L/S65T/E222Q; EGFP: F64L/S65T wtGFP; the wQ (Q → E) case refers to simulations where the Q was replaced by E during the excited-state simulations, but starting from the same ground state configurations of wQ. **b** Ground-state (top) and excited-state (bottom) representative MD snapshots of wildQ. In the bottom image, thanks to the twisted chromophore conformation, Q222 is able to form two H-bonds (green dotted lines). Figure adapted with permission from ref. [112]. Copyright 2018 American Chemical Society

Dronpa and its variants Dronpa was developed by Miyawaki et al. in 2004 [100] and it has been widely used ever since, becoming the "archetype" of negative protein switchers. Of note, this protein features a Y-Chro which differs from the wtGFP chromophore for the presence of Cys instead of Ser at position 65 (CYG chromophore). At physiological pH, Dronpa predominantly exhibits a bright/on state with a primary absorption peak at 503 nm, reflecting the *cis* **B** state (Table 1) [158]. Additionally, a smaller absorption peak at 390 nm is attributed to the neutral chromophore (**A'**). Exposure of *cis* **B** to 488 nm light produces intense fluorescence peaking at 518 nm ($\Phi = 0.85$), along with photoswitching *off* to *trans* **A'** with $\varphi_{off} = 3.2{\cdot}10^{-4}$ [159] (an alternative value of $1.6{\cdot}10^{-4}$ was reported by [103]). Illumination with 405 nm light swiftly reactivates the protein to its on state with $\varphi_{on} = 0.37$ [100, 115, 159] (an alternative value $\varphi_{on} = 0.165$ was reported by [103]).

Dronpa was well-characterized at single molecule level, demonstrating the inverse proportionality of the residence times in the *on* (τ_B, Eq. 20a) and *off* (τ_D, Eq. 20b) states from the light intensity at 488 and 405 nm, respectively [115, 160]. Bustamante and coworkers discovered that τ_B is also significantly affected by 488 nm light, on account of the residual absorption of *trans* **A'** at this wavelength and the high value of φ_{on} [160]. Accordingly, the same group introduced the V147L replacement in Dronpa to obtain a spectrally identical, slower photoswitching variant named rsKame that displays a 1.6-fold longer τ_D under sole 488 nm illumination, hinting at a significant reduction of φ_{on} (Eq. 20b) [160].

Although the properties of Dronpa allowed for its use in several imaging applications, the photoswitching properties of this protein are far from being optimized. For instance, the *off*-photoswitching yield of Dronpa is 1/20 of that reported for rsEGFP2. Compared to the latter protein, Dronpa displays also lower contrast and much lower

resistance to photobleaching (PR = 0.002 of rsEGFP2). Thus, several attempts have been devoted to optimize Dronpa photoswitching by sequence engineering.

The V60A replacement led to ffDronpa, a Dronpa variant optimized for very fast folding. ffDronpa is spectroscopically identical to Dronpa, but it is characterized by slightly slower *off*-photoswitching (Table 1) [103]. A faster ffDronpa, named ffDronpa-F, was developed through the screening of rational, semi-rational and random mutagenesis libraries. Compared to ffDronpa, ffDronpa-F bears two additional mutations, K45I and F173V, the latter increasing the *off*-photoswitching kinetics by about 1 order of magnitude compared to Dronpa [165].

rsFastLime variant was developed by adding a V157G mutation in Dronpa, thereby reducing steric hindrance exerted on the *trans* chromophore [144, 158]. Accordingly, rsFastLime is characterized by a tenfold faster *on* → *off* switching rate compared to Dronpa, as witnessed by the comparison of φ_{off} values, although this comes along with a slight decrease in Φ to 0.77 (Table 1) [158, 169]. Faster *off*-photoswitching was accomplished by the incorporation of a single (M159T) and double (V157I/M159A) mutations in Dronpa, to give Dronpa-2 or Dronpa-3, respectively. Dronpa-2 is about 1100-fold faster to switch *off* than Dronpa (Table 1). Yet, Dronpa-2 is significantly less emissive than Dronpa (Φ = 0.28). The switching *off* of Dronpa-3 is only 2 times faster than for its parent protein, but again the fluorescence quantum yield is significantly reduced (Φ = 0.33, Table 1) [164].

In view of further optimizing the Dronpa's properties, the Dedecker group has developed two proteins, pcDronpa and pcDronpa2, which efficiently combine negative photoswitching with green-to-red photoconversion [103]. pcDronpa and pcDronpa2 are tetrameric and, when in the "green" state ("GFP-like" chromophore) their spectral properties are almost indistinguishable from those of Dronpa, whereas *off*-photoswitching is 15 (pcDronpa2) to 30-fold (pcDronpa) slower. Illumination with strong 405 nm light photoconverts pcDronpa and pcDronpa2 to their red forms, which absorb at 569 nm and emits slightly above 580 nm (Table 1). Yet, after 50–60% of photoconversion, the UV-induced irreversible photobleaching becomes dominant [103]. In the red form, both proteins cannot be photoswitched back to the green state. SDS-PAGE and crystallographic studies on pcDronpa revealed that green-to-red photoconversion is accompanied by protein backbone cleavage between the Cα and the Nα of His62 [103], in line with the typical β-elimination mechanism which generates the red form of the HYG chromophore by extension of the π-conjugated system (e.g. in Kaede and EosFP) [170].

3.2.5 Negative RSFPs from cFP484 of *Clavularia sp.*

The main properties of most representative variants are reported in Table 2

mTFP0.7 mTFP0.7 is a cyan-emitting monomeric RSFP derived from the marine organism *Clavularia*, and it has been developed through directed evolution from TFP1.0 [171]. mTFP0.7 contains a Y-Chro obtained from the tripeptide ATG, which at physiological pH is fully deprotonated owing to a $pK_a = 4$ [171]. The bright cyan fluorescence of mTFP0.7 (Φ = 0.5) can be obtained by illuminating the *cis* **B** band (*on* state) around 450 nm; the same wavelength switches *off* the protein to the *trans*

A' (*off*) state, which absorbs around 370 nm (Table 1) [161]. Illumination of *trans* **A'** promptly restores the initial fluorescence. Interestingly, in the *on* state the mTFP0.7 chromophore adopts a *cis* conformation with the aromatic rings slightly tilted from coplanarity, whereas *trans p*-HBI is significantly nonplanar. Additionally, mTFP0.7 shows a rather fast monoexponential thermal decay from *trans* **A'** to *cis* **B**, with clear pH-dependence [161]. The replacement of I161 with V or T residues was found to slow down the thermal recovery, possibly on account of a lower steric hindrance with *p*-HBI in the *trans* configuration [161].

GMars variants Starting from mMaple3, a photoactivatable FP derived from *Clavularia sp.* [172], Wang and coworkers developed the GMars palette of RSFPs by a simple, yet straightforward, strategy [127, 162, 173]. Having noted the 78% sequence similarity between mMaple3 and mEosFP, they relieved the steric hindrance of M159 on the chromophore by replacing this residue with Alanine, much alike Adam and coworkers did on mEosFP to obtain reversible photochromicity (§2.4.6.2) [101]. The residual green-to-red photoconversion of mMaple3 M159A was then removed by mutation of the first amino acid of the HYG chromophore (H71), according to the same approach that inhibited color photoconversion in mGeos variants (§2.4.6.1) [102]. By this strategy, a set of 17 negative RSFPs, -all characterized by the H71X replacement- were engineered [173]. Of note, H71P replacement in GMars-P led to chromophore maturation but negligible fluorescence, whereas chromophore maturation was severely hampered in vivo for GMars-R and GMars-Y. Much alike mTFP0.7, GMars exhibited a blue-shifted absorption and emission spectrum as compared to green negative RSFPs such as rsEGFP2 or Dronpa (Tables 1, 2) [127, 162, 173]. Excitation of *cis* **B** around 470 nm yields bright fluorescence slightly below or at 500 nm ($\Phi = 0.65$ for GMars-Q [127] and the other variants display 0.1–2.5-fold the brightness of this variant, Table 2 [162, 173]) and also photoconverts the proteins to dark *trans* **A'** absorbing around 380 nm; 405-nm light promptly restored the *on* state. GMars displays contrast values ranging from 200 to about 10, being about 100 for the two most interesting variants, GMars-Q and G-Mars-T (Table 2) [173]. GMars-Q, GMars-L, GMars-T were reported to photoswitch-*off* 4.5-, 3- and twofold slower than rsEGFP2 under similar 488-nm illumination conditions, respectively [173]. For all other GMars variants, the *off*-photoswitching kinetics resulted one-to-threefold slower than GMars-Q. Although no quantitative determination of the switching fatigues was carried out, GMars exhibit more photobleaching fatigue as compared to rsEGFP2, except for GMars-L. Indeed, for GMars-Q, from the photobleaching plot we can infer $PR \sim 3 - 3.5$ as compared to rsEGFP2 (Table 2) [173]. Of note, a few GMars including GMars-Q exhibited an unusual pronounced biphasic photobleaching characteristic [127].

3.2.6 Negative RSFPs from EosFP of *Lobophyllia hemprichii*

The main properties of most representative variants are reported in Table 3.

mGeos and Skylan variants In 2012, Chang and coworkers reported that mutation of H62 in mEos2, a popular monomeric, irreversible green-to-red photoconverter, afforded a wide palette of negative RSFPs, which were called mGeos (monomeric

green Eos) [102]. In mEo2s, the *p*-HBI chromophore is the result of post-translational modification of the H62-Y63-G64 (HYG) triad: thus, H62X replacements act directly on the chromophore. mGeos proteins display spectral characteristics analogous to Dronpa, although some variants are brighter in the *on* state (Table 3) [102]. Accordingly, their photophysical characterization was carried out mostly in comparison with Dronpa and rsFastLime. As representative examples, we reported only a subset of mGeos (mGeos-E: H62E mutation; mGeos-M: H62M; mGeos-C: H62C) in Table 1, and the reader is referred to ref. [102] for the description of all the other mutants. Overall, mGeos variants with single H62X replacement exhibit variable *off* -photoswitching rates (from 0.25 to threefold) compared to Dronpa under the same illumination [102]. Addition of the F173S replacement did not change the spectral properties but greatly improved *off* -switching rates. For instance, mGeos-ES (H62E/F173S) exhibits a three times faster *off*-photoswitching rate than rsFastLime [102]. Unfortunately, no data was reported for the *on*-switching kinetics. H62X and H62X/F173S mGeos appear to share the low resistance to photofatigue of Dronpa [102].

The same H62X mutation approach was later applied to non-switchable mEos3.1, and mEos3.2 yielding two interesting negative switchers endowed with the H62S mutation, named Skylan-S [168] and Skylan-NS [151]. Skylan-S and Skylan-NS are spectrally similar to mGeos, but they offer much more resistance to photobleaching with respect to Dronpa (Table 3). Conversely, their thermal decay back to the *on* state was faster than in Dronpa, although still in the tens of minutes timescale (Table 3). Skylan-S is a slower *off* -switcher (1.45-fold) compared to Dronpa, whereas Skylan-NS is much faster (threefold) [151, 168, 174]. Although these authors calculated the switching contrast by integrating the *on* fluorescence from 100% to 1/e during the *on* $\rightarrow$ *off* decay, both Skylan-S and Skylan-NS exhibit high (> 10) contrast (Table 3).

3.3 Negative orange/red RSFPs

As previously stated (§1.1 and §1.5), further post-translational modification of the "GFP-like" Y-chro may lead to extended conjugation, thereby red-shifting both the absorption and emission of the protein. Yet, although a few efficient orange-to-red negative RSFPs have been described [119, 126, 175–177], their characterization is still largely incomplete owing to the complex relationships between the protein structures and their photophysical phenotypes. Accordingly, these orange-to-red negative RSFPs have not found as many imaging applications as their blue-to-yellow counterparts described in §2.2. In the next section (§2.3.1), we first describe their photoswitching mechanism. Next, in Sects. 2.3.2–2.3.3 and Table 4 we report the main properties of several representative variants, grouped into families according to their common ancestor protein. Finally, in Sect. 2.3.4 and Table 5 we report those variants that combine green-to-red photoactivation and reversible photoswitching in both spectral conditions.

Table 4 Negative switchers with orange/red chromophore. In each group, the proteins are ordered according to increasing maximum excitation wavelength of the *on* state

Name	λ_{max} *ON* ex/em (nm)	εON ($\times 10^3$)[a]	ϕ_F	Brightness relative to EGFP	λ_{max} *OFF* (nm)	εOFF ($\times 10^3$)[a]	pK_a *cis*	λ_{off} /λ_{on} (nm)	$\tau_{1/2}$, thermal, (min)[b]	Contrast	PR[c]	Refs
from DsRed of *Discosoma sp.*												
rsCherryRev	572/608	42.3[e]	0.005	0.006	572[e]	41.8[e]	5.5[c]	550/450	0.2	2.3[f]		[175]
rsCherryRev1.4	572/609			0.03	572		5.5[c]	570/430		10[r]		[177]
from eqFP578 of *Entacmaea quadricolor*												
rsTagRFP	567/585	36.8	0.11	0.12	440[e]	15.3[e]	6.6[c]	570/445	65[g]	20[r]		[119]
rsFusionRed1	577 /605	82.4	0.10	0.25	568		4.6	592/ 400–510	82	3	0.1 [h]	[126]
rsFusionRed2	580/607	35.5	0.12	0.13	564		4.6	592/ 400–510		12.5	0.3 [h]	[126]
rsFusionRed3	580/607	38.0	0.08	0.09	565		4.7	592/ 400–510		20	0.14 [h]	[126]

[a] In $M^{-1} cm^{-1}$
[b] Of the *off* state
[c] For definition of PR see Eq. 48. We adopted: PR = 1 for rsEGFP2
[d] From the on to the off state
[e] From [176]
[f] From [176]; ref. [175] reports a value of 20
[g] From [126]
[h] These PR values (see Eq. 48) are calculated taking into account the number of cycles needed to halve the fluorescence at $\lambda = 510$ nm (data from Fig. S6 of [126])

Table 5 Negative switchers with dual green/orange states. In each group the proteins are ordered according to increasing maximum absorption wavelength of the *on* state

Name	λ_{max} *ON* ex/em (nm)	εON ($\times 10^3$)[a]	ϕ_F	Brightness EGFP = 1	λ_{max} *OFF* (nm)	εOFF ($\times 10^3$)[a]	pK_a	$\lambda_{off}/\lambda_{on}$ (nm)	ϕ_{off} $\times 10^3$	ϕ_{on} $\times 10$	$\tau_{1/2}$, thermal, (min)[c]	Refs
From dendFP of *Dendronephthya sp.*												
Dendra2 M159A GS[b]	471/504	51.1	0.55	0.84			6.5	488/405	1.1	0.8		[101]
Dendra2 M159A OS[b]	528/562	45.0	0.75	1.0			6.8	561/440	3.2	0.1		[101]
NijiFP GS[b]	469/507	41.1	0.64	0.78			7.0	488/405	1.8	1.0		[101]
NijiFP OS[b]	526/569	42.0	0.65	0.81			7.3	561/440	1.0	1.0		[101]
From EosFP of *Lobophyllia hemprichii*												
IrisFP (T) GS[b]	488/516	52.0	0.43	0.67	~ 380	~ 15	6.4	488/405	14[b]	5.0	330	[185]
IrisFP (T) OS[b]	551/580	35.0	0.47	0.50	450	~ 24	7.2	561/440	2.0	0.47	190	[185]
mIrisFP GS[b]	486/516	47.0	0.54	0.76			5.4	486/405	6.9	3.6	53	[186]
mIrisFP OS[b]	546/578	33.0	0.59	0.58			7.6	546/446	3.1	2.8	24	[186]

Table 5 (continued)

Name	λ_{max} *ON* ex/em (nm)	εON ($\times 10^3$)[a]	ϕ_F	Brightness EGFP = 1	λ_{max} *OFF* (nm)	εOFF ($\times 10^3$)[a]	pK_a	$\lambda_{off}/\lambda_{on}$ (nm)	ϕ_{off} $\times 10^3$	ϕ_{on} $\times 10$	$\tau_{1/2}$, thermal, (min)[c]	Refs
mEos F173S GS[b]	486/514	53.2	0.43	0.68			5.8	488/405	2.2	2.0	53	[186]
mEos F173S OS[b]	550/581	25.0	0.41	0.31			6.2	561/446	0.4	0.6	24	[186]

[a] In $M^{-1}cm^{-1}$

[b] GS = Green State; OS = Orange state

3.3.1 Photoswitching mechanism

Although ultrafast spectroscopy experiments have never addressed the photoswitching process of orange/red negative RSFPs, a few excellent studies have established four general properties of these variants [143]. (1) Photoswitching is due to *cis* ↔ *trans* photoisomerization of the chromophore. (2) The most efficient orange/red negative RSFPs share a "DsRed-like" chromophore, which is characterized by a MYG *p*-HBI structure possessing an additional conjugated N-acylimine group (C = N–C = O) generated by further post-translational modification of the original "GFP-like" chromophore (Scheme2 and §1.4) [85]. (3) In these proteins, the stable ground state *is not* composed solely by *cis p*-HBI, but the *trans* chromophore has a significant − when not overwhelming − population, on account of high chromophore mobility in its pocket and low energy differences between the two isomers; actually, the large presence of *trans* chromophore in the stable form of the protein is a widespread characteristic within the RFP family [85]. (4) Photoswitching is always coupled to protonation, and the classical *cis* **B** ≡*on* ↔ *trans* **A'**≡*off* scheme holds (Scheme 10), although also *trans* **B** can contribute to the *off* state (e.g. in rsCherryRev1.4 [177]).

In the following, we shortly address the properties of the most efficient red-emitting negative RSFPs grouped into families that share a common ancestor.

3.3.2 Negative RSFPs from DsRed of*Discosoma sp.*

The main properties of the most representative variants are reported in Table 4.

mCherry variants In 2008 the Jakobs group reported the successful conversion of non-photoswitching popular red-emitting mCherry (derived from the *Discosoma* sp. progenitor DsRed through sequential engineering [178]) into the negative RSFP variant rsCherryRev [175]. Starting from the knowledge of the *cis* chromophore configuration of mCherry [89], and in view of releasing the intrinsic *cis* ↔ *trans* photoisomerization of *p*-HBI, rsCherryRev was obtained through a mix of rational and multiple site random mutagenesis. First, I161S replacement afforded the larger chromophore cavity necessary for accommodating the putative *trans* isomer, leading to a photoswitching variant; next, residues surrounding the chromophore were mutated to optimize the switching efficiency. Of note, the engineering of I161S Cherry also afforded rsCherry, a positive RSFP (§2.4.2.2). In rsCherryRev the *on* state absorbs at 572 nm. Illumination at 550 nm switches *off* the protein, whereas irradiation at 450 nm restores fluorescence [175]. Remarkably, the *cis* **B** state of rsCherryRev undergoes a thermal decay that decreases (90%) the maximum *on* fluorescence ($\Phi = 0.005$, Table 4). Albeit little structural characterization of this mutant has been reported, it seems reasonable that the stable ground state of rsCherryRev is characterized by a mixture of *cis* **B**, *trans* **B**, and *trans* **A'**. A further series of mutagenesis afforded the variant rsCherryRev1.4 [177], which retained most of the photophysical characteristics of rsCherryRev but improved the contrast [126, 176] and the overall folding efficiency [177].

3.3.3 Negative RSFPs from eqFP578 of*Entacmaea quadricolor*

TagRFP variants Starting from the popular bright red fluorescent protein TagRFP (derived from *Entacmaea quadricolor* progenitor eqFP578 through sequential engineering, [179, 180]), the Verkusha group developed rsTagRFP by combining site-directed and random mutagenesis [176]. In this variant, illumination around 570 nm both excites fluorescence (at 585 nm) and switches *off* the protein [176]. The dark state of rsTagRFP is characterized by an absorption band at 440 nm and is promptly photoswitched back to *on* ($\varphi_{on}/\varphi_{off} = 1000$), yielding a contrast $R = 20$ (Table 4) [176]. Like rsCherryRev, after a single *on*-switching rsTagRFP relaxes to a ground state losing about one-third of *on* population ($t_{1/2} = 65$ min at RT). This equilibrated, partially fluorescent ground state can be also reached from the *off* state by thermal recovery ($t_{1/2} = 46$ min at RT). This peculiar behavior has been rationalized by X-ray measurements of the crystallized protein in its different photostates [119]. The *off* state of rsTagRFP corresponds to a protonated chromophore adopting exclusively the classical *trans* conformation (*trans* **A'**). Vice-versa, the thermally stable state is characterized by a mixture of *cis* **B** and *trans* **A**' isomers. The easy ground-state conversion between *cis* and *trans* state is also coupled with the proton equilibrium of chromophore, as higher pH favors *cis* **B** at the expenses of *trans* **A'**. This phenotype was linked to a complete absence of direct hydrogen bonding of the chromophore with the protein scaffold. The same work also proposed a protonation/deprotonation mechanism of the isomerizing chromophore that relies on H-bonded chain of three surrounding residues [119]. A similar pH-induced *cis* ↔ *trans* ground-state isomerization had been previously observed in the non-switching mKate protein [181], a variant directly evolved from TagRFP [182] and therefore closely related to rsTagRFP.

FusionRed family Starting from the monomeric and bright red fluorescent protein FusionRed (derived from *Entacmaea quadricolor* progenitor eqFP578 through sequential engineering of TagRFP and mKate [183]), Testa and coworkers engineered three negative red-emitting RSFPs: rsFusionRed1, rsFusionRed2, and rsFusionRed3 [126]. rsFusionRed1 have a single absorption band at 560 nm, whereas sFusionRed2-3 also displays a band around 400 nm. For these proteins, switching *off* is achieved by illumination at 590 nm, whereas switching *on* can be obtained by illuminating at a wide range of wavelengths, i.e. from 405 to 510 nm. rsFusionRed1-3 are characterized by contrast values of 12–20, like those observed for rsTagRFP ($R = 17$) and rsCherryRev1.4 ($R = 10$) [126]. Yet, under the same illumination intensity, rsFusionRed1-3 showed much faster *off*-switching kinetics compared to rsTagRFP (8–30-fold) or rsCherryRev1.4 (four-to-sixfold). rsFusionRed proteins also displayed strong resistance to irreversible photobleaching, witnessed by a drop of 50% fluorescence after about 1000 cycles when illuminated at 510 nm [126]. Spontaneous recovery from *off* state occurred with 20–40 min half-life, in line with rsTagRFP and rsCherryRev1.4 [126]. Remarkably, however, only rsFusionRed1 exhibited the thermal *on* → *off* decay found in rsTagRFP, rsCherryRev and rsCherryRev1.4. Although no further characterization was provided by Testa and coworkers. We may speculate that the *trans* chromophore is negligibly present in the thermally-equilibrated state of rsFusionRed2-3.

3.3.4 Dual green/red photoswitchers

Quite remarkably, the irreversible green-to-red photoconversion was combined with reversible photoswitching to generate dual green/red photoswitchers from *Anthozoa* proteins.

IrisFP was obtained by Adam and coworkers in 2008 by introducing a single F173S mutation in the EosFP of *Lobophyllia hemprichii* [184]. At physiological pH, the *cis* **B** and **A'** states of native IrisFP absorb near 488 nm and 390 nm, respectively [185]. Green fluorescence at 516 nm is obtained upon excitation of *cis* **B** with $\Phi = 0.43$; fluorescence emission is paralleled by *on*-to-*off* photoswitching to *trans* **A'** ($\lambda =$ 390 nm), with $\varphi_{off} = 0.014$ (Table 5). Excitation of *trans* **A'** at 405 nm reactivates efficiently the protein ($\varphi_{on} = 0.5$) and induces its conversion to an orange form (φ_{gr} $= 0.0018$) [185]. The orange form of IrisFP absorbs around 551 nm and emits at 580 nm with $\Phi = 0.47$. Very remarkably, the orange form can also switch between *on* and *off* states using 532 nm and 440 nm light, respectively, albeit the photoswitching yields are lower than for the green form ($\varphi_{off} = 2{\cdot}10^{-3}$, $\varphi_{on} = 0.047$) [185]. Since the tetrameric nature of IrisFP complicates its applications in cells, monomeric RSFPs that are also photoconvertible were subsequently engineered. In 2010, Nienhaus and coworkers realized the monomeric IrisFP (mIrisFP) by adding four mutations to IrisFP [186]. mIrisFP is slightly blue-shifted in the red form as compared to IrisFP, while its photoswitching yields are within a factor of three (Table 5). Yet, monomerization accelerates the thermal decay in both the green and red (orange) forms.

In search of a dual variant with more efficient green-to-red photoconversion, Adam and coworkers successfully transformed the popular green-to-red photoconvertible Dendra2 (derived from the ancestor protein dendFP of *Dendronephthya sp.*) into a palette of switchers by a rational mutation strategy [101]. In more detail, they modified the residues at positions 157, 159 and 173 which are located around the chromophore in several FPs and are supposedly of major importance in modulating the photophysical properties of the proteins. They also applied this strategy to mEosFP, a monomeric variant derived from EosFP by the A69V replacement [184]. Very remarkably, the authors found that the single F173S replacement generated dual photoswitchers in both the mEosFP and Dendra2 scaffolds. Conversely, M159A afforded a dual photoswitcher only when incorporated in Dendra2 [101]. Compared to Eos derivatives, Dendra derivatives are blue-shifted by about 10–20 nm in both absorption and emission of the green and red forms (Table 5). Yet, photoswitching yields of green and red forms are very similar for all three variants (Table 5) [101, 185, 186]. Dendra2 variants were found to be much more stable as dimers than mEosFP derivatives and, on account of its efficient green-to-red photoconversion (φ_{gr} was not reported), Dendra2 F173S has been named NijiFP, from the Japanese word for rainbow [101].

3.4 Positive RSFPs

Positive switchers appear extremely valuable for imaging applications, particularly RESOLFT (§2.4.1) [187]. In spite of this, only a few variants displaying the switching phenotype have been reported. In the next section (§2.4.1), we first describe their

photoswitching mechanism. Next, in Sects. 2.4.2–2.4.3 and Table 6 we report the main properties of known variants, grouped into families according to their common ancestor protein.

3.4.1 Photoswitching mechanism of positive RSFPs

As previously stated, positive RSFPs are characterized by a photochromic behavior opposite to negative switchers. Yet, their photophysical phenotype can be interpreted in the same way: photoswitching occurs as photoisomerization from a dark *trans* to a *cis* bright state of their Y-Chro. The major change in positive switchers is the relative stability of states: the *trans* anionic chromophore is now more stable than its protonated form, on account of the different stabilizing interactions of *p*-HBI with its surrounding residues. Additionally, the *trans* configuration is usually more stable than its *cis* counterpart. This change of pattern is brilliantly highlighted by the evolution of the positive RSFP Padron from negative switching Dronpa. In Dronpa, a robust hydrogen bonding interaction between Ser142 and *p*-HBI stabilizes the *cis* conformation, enabling the negative switching pattern. Padron is a monomeric RSFP created from Dronpa through the introduction of eight mutations [163]. Mutation M159Y is critical, as Y159 establishes a strong H-bond with *p*-HBI stabilizing the anionic *trans* conformer of the chromophore and flipping the switching direction [163]. Schematically, in positive switchers the *off* state combines *trans* configuration and deprotonation of the phenolic function (*trans* **B** state). Excitation at the absorption wavelengths of *trans***B** triggers *trans* → *cis* photoisomerization. Instead, exciting *cis* **A'** switches the protein to *trans* **B**, whereas exciting *cis***B** elicits fluorescence (Fig. 4). Both *cis* **A'** and *cis***B** forms of the chromophore may be populated at physiological pH, and their stoichiometric ratio is determined by the nature of amino acids that surround the chromophores. Thus, a remarkable difference between negative and positive switchers pertains to the actual fluorescence of the *trans* state(s) and the role of protonation in determining the emission loss. In negative switchers, the loss of fluorescence of the *trans* state is an effect of the protonation following the *cis*-to-*trans* isomerization [143]. In positive switchers, instead, the *trans* form of the chromophore is dim or non-fluorescent also in the deprotonated state, likely on account of an increase in chromophore flexibility upon excitation [188]. The inverse stability of *cis* and *trans* states may be also the basis of the radical change of photoswitching yields: in positive switchers φ_{off} is generally much higher than φ_{on}, opposite to negative RSFPs [104]. Yet, φ_{off} is at best around 0.1–0.2, and this has so far complicated ultrafast studies addressing the photoisomerization mechanisms. For Padron, Fron et al. described *cis* → *trans* and *trans* → *cis* photoprocesses with 14.5 and 5.2 ps time constants [189], respectively, but their findings are questioned by the low switching yields of this positive RSFP variant (§2.4.3) [143]. Nonetheless, their data converge with those of Walter et al. [190] in showing that the first step of photoinduced *cis* → *trans* isomerization may involve ultrafast (~ 1 ps) ESPT of the chromophore.

Table 6 Positive and decoupled switchers. In each group, the proteins are ordered according to increasing maximum excitation wavelength of the *on* state

Name (M = monomer T = tetramer)	λ_{max} *ON* ex/em (nm)	εON ($\times 10^3$)[a]	ϕ_F	Brightness relative to EGFP	λ_{max} *OFF* (nm)	εOFF ($\times 10^3$)[a]	pK_a (*cis*)	$\lambda_{off}/\lambda_{on}$ (nm)	$\phi_{off} \times 10$	$\phi_{on} \times 10^3$	$\tau_{1/2}$, thermal, (min)	Contrast	PR[b]	Refs
Positive switchers (on → off)														
From 22G of *Echinophyllia sp. SC22*														
Kohinoor	495/514	62.9[c]	0.71	1.33	496	39.5[d]	5.9	405/488	1.5[c]	20[c]			0.3	[191]
Kohinoor 2.0	500/516	31.2	0.61	0.57			6.0		3.3					[192]
Padron*	503/519	58.0	0.62	1.07	503			405/488			110	50	0.01	[163]
Padron	503/522	43.0	0.64	0.82	505	57.7[d]		405/488	0.4	3	150	143	0.02	[163]
Padron2	492/516	13.2	0.49	0.48	498	48.7			1.15	5			8.1	[187]
Padron0.9	504/529	36.0	0.61	0.65	504		5.6		0.2[d]	0.3[d]	250	250		[188]
From asFP595 of *Anemonia sulcata*														
asFP595 (T)	572/595	56.2	< 0.001	< 0.002				450/569						[193]
KFP1 (T)	590/600	59.0	0.07	0.12				458/532						[99]
From DsRed of *Discosoma sp.*														
rsCherry	572/610							450/550			0.7	7		
Decoupled														
From avGFP of *Aequorea* Victoria														

Table 6 (continued)

Name (M = monomer T = tetramer)	λ_{max} *ON* ex/em (nm)	εON ($\times 10^3$)[a]	ϕ_F	Brightness relative to EGFP	λ_{max} *OFF* (nm)	εOFF ($\times 10^3$)[a]	pK_a (*cis*)	$\lambda_{off}/\lambda_{on}$ (nm)	$\phi_{off} \times 10$	$\phi_{on} \times 10^3$	$\tau_{1/2}$, thermal, (min)	Contrast	PR[b]	Refs
Spoon	510/527	54.0	0.5	0.80			7.2	411/339						[105]
Dreiklang	511/529	83.0	0.41	1.01			7.2	405/365						[104]

[a] In $M^{-1}cm^{-1}$

[b] For a definition of PR see Eq. 48. We adopted: PR = 1 for rsEGFP2

[c] Value at pH = 10; at pH = 7.5 [190] reports $\varepsilon = 12.4$

[d] Ref. [187] reports: $\varphi_{off} = 0.088$ and $\varphi_{on} = 0.015$

[e] From [190]

3.4.2 Positive RSFPs from asFP595 of*Anemonia sulcata*

asFP595 and its variants Although its tetrameric nature, the poor switching properties and the imperceptible quantum yield (< 0.001) strongly hampered the use of asFP595 in imaging applications, this protein must surely be cited as it has been the first positive RSFP ever reported. asFP595 was isolated from the sea anemone *Anemonia sulcata* by Lukyanov and coworkers [193], and afterward it has been the subject of intense photophysical studies [110, 114, 159, 194–196]. The chromophore of asFP595 come from the cyclization/oxidation modification of the M63-Y64-G65 (MYG) tripeptide to give a highly conjugated 2-iminomethyl-5-(4-hydroxybenzylidene)-imidazolidinone system, where the original conjugation of the wtGFP chromphore is elongated by an additional carbonyl group [86]. Yet, X-ray measurement on asFP595 and its variants A143G (KFP1: "kindling" fluorescent protein, $\Phi = 0.07$ [99]) and A143S have shown that the protein backbone is broken between C62 and the chromophore [159, 197, 198]. In the *off* state, asFP595 and its variants adopt solely the *trans* configuration of the deprotonated chromophore (*trans* **B**), absorbing at ~ 570 nm (Table 6). asFP595 and KFP1 can be switched-*on* by illuminating *trans* **B**. Jakobs and coworkers were the first to identify the *on* state of the A143S variant of asFP595 with the *cis* configuration of the chromophore, which is partly protonated [159]. Illumination on *cis* **A'** around 450 nm switches back these proteins to the *off* state. Yet, thermal *cis* → *trans* relaxation occurs within a second in all mutants, being very fast in the ancestor asFP595. Of note, prolonged irradiation with intense green light leads irreversibly to a non-switching fluorescent state [99]. At the basis of this phenomenon could be a stabilization of the *cis* **B** state due to photoinduced decarboxylation of the glutamic acid E215, similarly to what was observed in wtGFP [93].

rsCherry rsCherry was developed by Jakobs and coworkers from mCherry concomitantly to the negative switcher rsCherryRev (§2.3.2.1). Both variants share the I163S mutation that enables the chromophore cavity to accommodate the *trans p*-HBI form [175]. rsCherry exhibits an absorption peak at 572 nm and emits at 610 nm, whereas excitation at 450 nm promotes switching *off* with a final residual fluorescence of about 15% ($R = 7$, Table 6). Thermal relaxation is rather fast, as the *on* state loses about 70% fluorescence with $t_{1/2} = 40$ s [175]. Altogether, these findings indicate higher stability of *trans* **B** compared to *cis* **A'**, but ground state chromophore isomerization has a low energy barrier. Although no extensive characterization of the photoswitching yields has been reported yet, Jakobs and coworkers claimed this protein to be rather slow-switching in comparison to more optimized variants belonging to the Padron family (§2.4.3) [187].

Padron family A major breakthrough in the field of positive switchers was obtained by Jakobs and coworkers with the development of the already mentioned Padron [163] and its derivatives Padron* (I94H/I100S/L141R/K222N) and Padron0.9 (Y116C/K198I Padron) by a combination of rational and random mutagenesis of the Dronpa sequence [163, 188]. Both Padron* and Padron0.9 conserve the same spectral properties of Padron. Yet, while Padron* eliminates the slight tendency of Padron to

dimerization (15% at 4 °C), Padron0.9 is slightly more amenable to dimerization, thus facilitating its crystallization.

In their *on* states at physiological pH, Padron, Padron*, and Padron0.9 display a smaller absorption peak at around 395 nm (*cis* **A'**) and a larger peak at 503 nm (*cis* **B**), resulting from a rather high pK_a ($pK_a = 6.0$ for Padron0.9, Table 5) [163]. When illuminated with light at around 503 nm, Padron and Padron0.9 produce strong green fluorescence ($\lambda_{em} = 522$ nm) ($\Phi = 0.64$ for Padron, 0.61 for Padron0.9, Table 6) [163]. In these proteins, illumination of *cis* **A'** induces *cis* → *trans* photoisomerization, which in turn drops the pK_a of the chromophore ($pK_a = 4.5$ for Padron0.9, Table 6), leading to an *off* state dominated by *trans* **B** (absorbing at 504–505 nm) [163, 188]. *trans* → *cis* isomerization in Padron is decoupled from the protonation change at the phenolic hydroxy end, enabling photoactivation of Padron fluorescence at cryotemperatures [199]. Padron and Padron0.9 share impressive contrast $R > 100$, as well as slow spontaneous *on* → *off* decay (Table 6) [188]. Unfortunately, these two RSFPs are characterized by rather slow switching, as witnessed by photoswitching yields well below 0.01 (Table 6) [163, 190].

In the quest for a faster switcher, the Nagai group. developed Kohinoor by introducing 8 mutations into the Padron's sequence [191]. Kohinoor is indeed associated with 4–tenfold faster switching than Padron ($\varphi_{off} = 0.15$ and $\varphi_{on} = 0.02$, Table 6) and slightly improved fluorescence quantum yield ($\Phi = 0.71$), although a lower contrast ratio $R \sim 50$ and an 8–10 nm blue-shifted absorption/fluorescence were reported [191]. Of note, the photoswitching yields of Kohinoor have been recently revisited by the Jakobs group, which published $\varphi_{off} = 0.088$ and $\varphi_{on} = 0.015$ [187]. Kohinoor has been recently optimized to Kohinoor2.0 by introducing 7 more mutations [192]. Kohinoor2.0 retains the same spectral properties as Kohinoor while being 2.6-fold brighter, on account of the larger absorption of the fluorescent *cis* **B** state. Kohinoor2.0 also switches *off* faster than its ancestor, owing to an increase of φ_{off} (Table 6) [192]. Much alike Padron, in Kohinoor and Kohinoor2.0 the *on* state partitions into a protonated and a deprotonated chromophore, with a complex pH dependence, but in contrast to Padron the *on* (*cis*) state(s) also constitute the thermally equilibrated forms. A careful investigation posited the presence of three distinct protonation equilibria ($pK_{a1} \sim 6$, $pK_{a1} \sim 8.2$–8.6, and $pK_{a3} \sim 9.3$) affecting the optical properties of Kohinoor and Kohinoor2.0, related to as many conformational states [192]. It was speculated that the protonation equilibria of H193, E144 and E211 may influence pK_{a2} and pK_{a3} through a network of hydrogen bonds, assuming implicitly that pK_{a1} refers to *p*-HBI protonation [192]. A multiple protonation pattern has been revealed also for the *on* and *off* states of Padron0.9 [190]. Analogously to Kohinoor and Kohinoor2.0, a model involving the protonation of the chromophore as well as of two more residues has been invoked [190]. Although it has not been considered as such, these patterns are consistent with the 2S-model of FP protonation and reveal the presence of the mixed state **A** (§1.3) around neutral pH.

It has been observed that the major obstacles to applying Padron, Kohinoor and Kohinoor2.0 to unconventional (e.g. super-resolution) imaging applications resides in their limited fatigue resistance under the typical microscopy illumination intensities [187]. To address this issue, the Jakobs group has recently developed Padron2 through random and site-directed mutagenesis of the Padron sequence [187]. Padron2 has

spectral and photoswitching properties similar to Kohinoor, but it showed increased resistance to photobleaching in comparison to both Kohinoor and Padron under continuous illumination at 488 nm in bacterial colonies (Table 6).

3.5 Decoupled RSFPs

The spectral and switching properties of the decoupled switchers are listed in Table 6. As previously mentioned, Dreiklang and its descendant Spoon distinguish from both negative and positive switchers in that their photoswitching is driven at wavelengths not relevant to produce fluorescence. This *decoupled* photochromic behavior stems from a molecular mechanism not involving *cis–trans* photoisomerization (Fig. 4) [104]. Dreiklang has been developed by introducing the mutations V61L/F64I/Y145H/N146D in the yellow mutant Citrine from *Aequorea* (S65G/V68L/Q69/M/S72A/T203Y wtGFP) [104]. Unlike Citrine whose pK_a is around 5, native Dreiklang has $pK_a = 7.2$ and is therefore characterized by a mixture of protonated **A'** ($\lambda = 412$ nm) and deprotonated **B** ($\lambda = 511$ nm) at physiological pH (Table 6). Excitation of **B** generates fluorescence at 529 nm with $\Phi = 0.41$. On the other hand, excitation of **A'** causes hydration of the C65 atom of the imidazolidinone ring, thereby transitioning the protein to the *off* state, which absorbs around 350 nm. Illumination on the *off* state band leads to the reactivation of the protein. The decoupled wavelengths of photoswitching and fluorescence excitation avoid the conflicting effects between *on*, *off*, and excitation lights that are always intertwined in negative and positive switchers and make Dreiklang very useful for several applications [104]. Spoon adds five more mutations to the Dreiklang sequence (I47V/T59S/M153T/S208G/M233T), and is spectroscopically indistinguishable from its parent protein, being nonetheless much faster to *off*-photoswitching [105]. The photoswitching mechanism of Dreiklang (and presumably of Spoon) involves first ESPT from excited *cis* A', followed by a negative charge transfer to the imidazolidinone ring, which is eventually protonated by the nearby E222 catalyzing the addition of a water molecule [200]. This water adduct, where the classical π-conjugated electron system of *p*-HBI is shortened, absorbs around 350 nm and -upon excitation- photochemically reverts to the **A'** and **B** states by eliminating a water molecule [104]. Yet, this mechanism has been recently challenged by a computational study, which posits a three-step proton transfer from Y203 to the chromophore locked by water addition [201].

4 Applications

In 2004, Miyawaki and coworkers published the first application of a reversibly photoswitchable protein, Dronpa, to imaging [100]. By an approach that has been referred to as inverse FRAP (or $FRAP^{-1}$), they first converted all the protein to the *off* state and the reactivated it selectively in the cell nucleus (or cytoplasm), wherefrom they followed the protein nucleocytoplasmic diffusion due to active transport. This pioneering result came only two years after the demonstration by Patterson and Lippincott-Schwartz that the photoactivation of an FP could add an externally controllable discrete and

reversible dimension to space, time and wavelength dimensions to enable functional microscopy [202]. From any perspective, the pioneering work of Miyawaki offered an even more valuable option: the reversibility of external control with light that would incredibly expand the number of imaging schemes to retrieve information from the cellular setting. The age of photochromic FPs applied to bioimaging had eventually started.

Two years later came the super-resolution revolution, i.e. the popularization of a scientific concept that had smoldered under the ashes of some very specialized literature for decades [16]. Basically, the extra dimension offered by photochromic fluorophores could enable optical imaging at an unprecedented spatial resolution.

In the last 20 years, the number of applications of RSFPs has constantly grown, disclosing crucial knowledge about several biological processes, concomitantly leading to a heated technological and industrial field of research. It is nearly impossible to summarize in a few pages all the applications that have leveraged the peculiar photophysics of RSFPs, and we shall not attempt it. Rather, in the following sections we shall focus on representative families of imaging schemes, particularly in the super-resolution field, which clearly posit the enormous potential related to the combination of genetic encoding and reversible control of the optical properties by external light.

4.1 RSFPs in super-resolution microscopy (SRM)

In this section, we initially provide a short introduction to the basic idea of SRM, although the reader is referred to more specialized reviews for a comprehensive description of this field of microscopy [14, 15, 203]. Then, we shall review the main applications of RSFPs by distinguishing between two different families of SRM: those which are based either on the time or on spatial modulation of the excitation/emission, respectively.

Viewed through the lens of physics, light emitted by a point source, such as a fluorescent molecule observed through a microscope's objective, is subject to diffraction. This effect causes the point source to manifest in the resulting image as what is termed an Airy diffraction pattern [204]. Due to the reversible nature of light paths, the same spreading effect is evident when light converges to a single point, like when a sample is lit up to trigger fluorescence. This spread of light in three dimensions, shaped by the Airy pattern, is defined as the Point Spread Function (PSF). The PSF's inherent size places a cap on the optical system's spatial resolution. This cap is quantified by Ernst Abbe's principle, which articulates that the smallest separation at which a microscope can resolve two distinct points—the image's maximum spatial frequency—is given by a specific formula [205]:

$$d = \frac{\lambda}{2NA}, \tag{51}$$

where λ is the wavelength of the probing radiation and NA is the numerical aperture of the microscope objective. Thus, our ability to distinguish two nearby emitter is limited to about half the emission wavelength at best. Eukaryotic cells, typically ranging in diameter from 10 to 300 μm, pose a challenge due to their small size and the

dense presence of proteins. Indeed, confocal microscopes are limited to approximately 200–300 nm of lateral resolution (in the xy plane of the sample) and 600–1000 nm of axial resolution (along the z-axis of the sample). Yet, the resolving power of an optical device such as a microscope is not a well-defined physical quantity, Rather, it greatly hinges on the extent of information about the subject in view, as originally stated by Toraldo di Francia [206]. For example, in classical "diffraction-limited" fluorescence microscopy, no previous knowledge about the sample or the way we address each emitter is provided. Accordingly, all fluorophores within the excitation PSF are excited and emit light almost simultaneously. Therefore, their fluorescence signals are detected together as the product of excitation and emission PSF. The fundamental solution to overcome this diffraction barrier lies in briefly making adjacent molecules distinguishable, preventing the simultaneous detection of different molecules within the same diffraction region. For this aim, it is necessary to infuse the system with extra information. This can involve manipulating the likelihood that molecules will emit light when excited, effectively dispersing their emissions either spatially (coordinate-targeted SRM) or temporally (coordinate-stochastic), preventing their collective detection. This approach is the key to super-resolution microscopy and heavily relies on the bistability of the emitters (Fig. 9) [16]. This bistability may stem from an intrinsic property of any fluorophore, like the *on–off* photoswitching by alternate excitation and stimulated emission exploited in STimulated Emission Depletion (STED) microscopy. Albeit less general, the use of photochromic molecules such as RSFPs enables the use of much lower illumination intensities, with obvious beneficial effects on the viability of biological samples [207].

In all super-resolution applications relying on RSFPs as labels, image quality and the achievable spatial resolution are determined by the fluorescence brightness, the ensemble switching speed, the switching fatigue, and the switching contrast [131]. The latter is undisputedly the most critical parameter for achieving high spatial resolution, and its maximization is one of the most important targets in the engineering of RSFPs for SRM [151].

4.1.1 SRM approaches that leverage time-modulation of the excitation/emission

Fluorescence photoactivation localization microscopy (PALM, F-PALM) The family of SRM techniques generally referred to as Single Molecule Localization Microscopy (SMLM) [208] was pioneered in 2006 concomitantly by the groups of Betzig [209], Zhuang [210], and Hess [211]. For this discovery, Eric Betzig received the Nobel Prize in Chemistry in 2014, together with other two pioneers of SRM, Stefan Hell [212] and William E. Moerner [95]. SMLM includes stochastic optical reconstruction microscopy (STORM [210]), also in its variant *direct* STORM (dSTORM [213]), fluorescence photoactivated localization microscopy (F-PALM [209, 211]), and point accumulation for imaging in nanoscale topography (PAINT) [188–190]. Within SMLM, *single fluorophores* from the same excitation PSF are *temporally isolated* by recording their emissions *one at the time* (Fig. 10) Achieving this result is feasible either through the transient attachment of fluorophores that emit light continuously, as seen in the PAINT technique or by employing photoactivatable fluorophores (F-PALM and STORM/dSTORM). In both cases, excitation randomly activates only

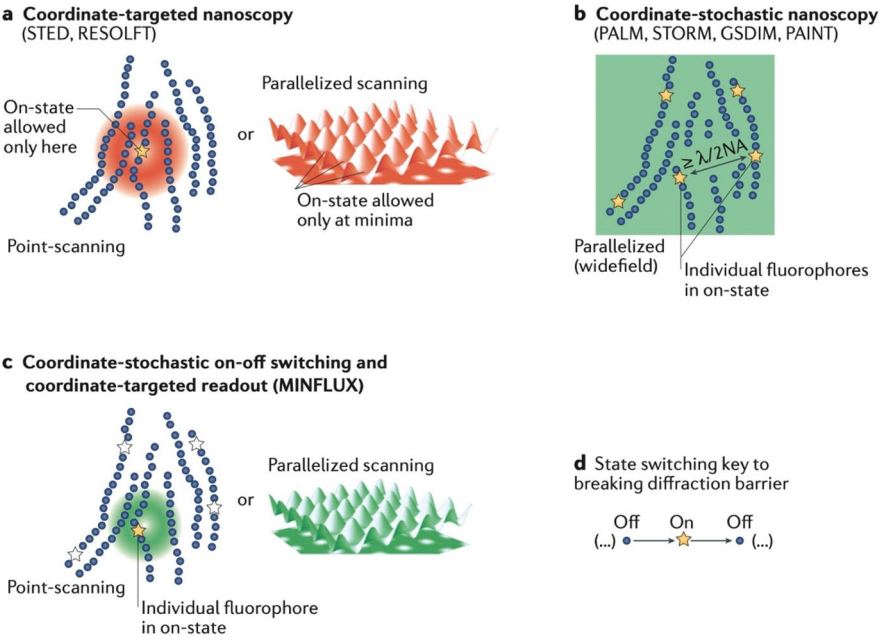

Fig. 9 Basic working principles of super-resolution microscopy (SRM). **a** Coordinate-targeted SRM: a spatially-modulated point light pattern (red) is used to *off*-switch the fluorophores, whereas fluorophores stay *on* only at the intensity minima (shown by the yellow star). This approach can also be parallelized (red, periodic pattern). **b** Coordinate-targeted SRM: single-*on* fluorophores are established and localized at distances larger than the diffraction limit $d = \lambda/2\mathrm{NA}$ (Eq. 49). **c** Coordinate-targeted and coordinate-stochastic can also be combined, and single fluorophores can be localized at the nanometre scale with minimal photon numbers (MINFLUX approach) because their position is inferred from the positioning of the intensity minimum of the light pattern used for excitation. **d** SRM techniques rely on *on* $\leftrightarrow$ *off* transitions of fluorophores to distinguish neighboring molecules in the same diffraction area. Reprinted with permission from ref. [14]

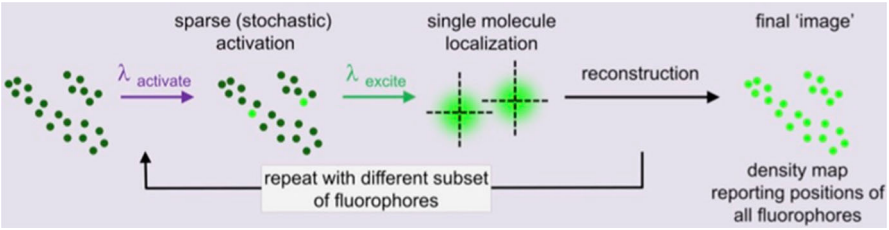

Fig. 10 Single Molecule Localization Microscopy (SMLM). SMLM approaches such as STORM/F-PALM rely on the stochastic activation of individual emitters by light localized with high precision. Adapted with permission from ref. [214]

a handful of fluorophores at any given moment. This approach is taken to ensure that the PSFs of individual fluorophores *do not merge into one another within the same snapshot*. The sample is subjected to a thousand cycles of activation and deactivation, and as many frames are recorded, each frame featuring only a limited number of sparsely distributed, single-molecule emitters (Fig. 10).

After the acquisition, a specialized algorithm is used to accurately determine the position of each molecule's center. This post-processing step culminates in the production of high-resolution images, achieving lateral resolutions down to < 20 nm. Actually, in SMLM the traditional concept of resolution has been replaced by *the precision* with which individual molecules are located. Achieving this high level of localization precision in SMLM requires long acquisition times, as the precision is directly linked to the square root of the number of photons collected [208].

F-PALM and STORM/dSTORM utilize either phototransformable fluorescent proteins (FPs) or blinking organic dyes as their temporally modulable emitters, respectively. With years irreversible photoconvertible FPs (PCFPs) have been preferentially chosen over reversible saturable/switchable fluorescent proteins (RSFPs) for F-PALM, because they generally produce a higher photon budget per each localization, display higher contrast, and have fewer issues with repeated localizations of individual molecules [12]. Yet, rsFastLime has been early applied to a F-PALM variant called "PALM with independently running acquisition" (PALMIRA). PALMIRA utilizes spontaneous *off–on* cycles of single negative RSFPs under illumination solely at excitation wavelength without synchronization to a detector [215, 216]. Similarly, the peculiar switching pattern of SPOON provided a simple F-PALM imaging platform that requires only a single 488 nm laser. In fact, strong irradiation of SPOON at 488 nm leads to an equilibrium between *off*-photoswitching and thermal switching-*on*, yielding a single wavelength blinking amenable to SMLM [105]. Instead, the fast negative switcher Dronpa-3 was applied to an F-PALM variant known as stroboscopic PALM (s-PALM), which leverages a dual-color lighting approach. s-PALM employs two-color (405/488 nm) short pulses whose duration is tuned to the characteristic *on*-time of the protein [217].

RSFPs were repeatedly proved useful in multicolor F-PALM. Bock et al. showed that rsFastLime could be localized concomitantly with Cy5, affording two-color nanoscale images inside whole cells [218]. A green-to-red photoconvertible protein such as PAmCherry1 was co-expressed with a negative green switcher like Dronpa: alternate illumination at 405 and 561 nm enabled localization of the PCFPs, whereas the alternate illumination at 405 and 488 afforded the localization of RSFPs (Fig. 11) [160, 219, 220]. Dual color F-PALM images were also obtained by co-expression of negative and positive RSFPs, such as bsDronpa or rsFastlime and Padron [163].

Stochastic optical fluctuation imaging (SOFI and pcSOFI) Dispersion of the emission over the temporal axis is also at basis of the SRM technique called Stochastic optical fluctuation imaging (SOFI). SOFI enhances image resolution by exploiting fluorescence intensity fluctuations ("flickering") of single fluorescent markers [18, 221]. The basic principle of SOFI involves collecting a series of images over time, where the fluorescent markers stochastically flicker *on* and *off* due to specific photophysical features. By analyzing the correlation of these intensity fluctuations over time, SOFI can

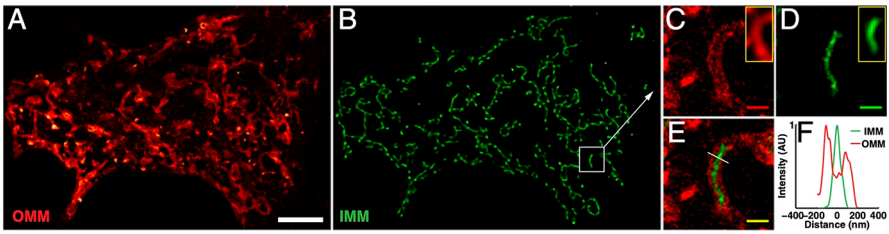

Fig. 11 Two-color F-PALM by combining the green RSFP rsKame with the green-to-red photoconvertible PAmCherry1. **a**, **b** In EpH4 cells, the outer (OMM) and inner (IMM) mitochondrial membranes were labeled with PAmCherry1-Lk-BclXl and BCS1L$^{1-160}$-Lk-rsKame, respectively. **c**–**e** Elongated mitochondria are observed with distinctly defined membranes (∼20-nm resolution). **f** intensity profiles in the two channels for the white line in panel (**e**) which crosses both OMM and IMM. Reprinted with permission from ref. [160]

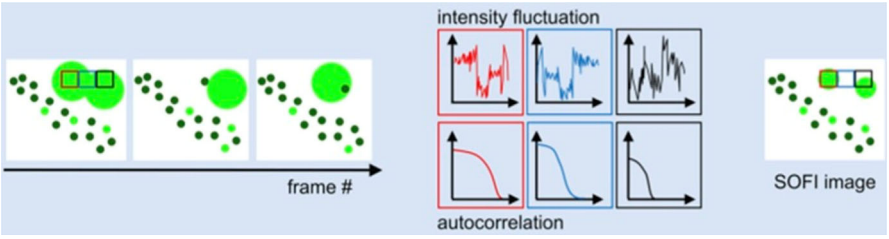

Fig. 12 Stochastic Optical Fluctuation Microscopy (SOFI). SOFI locates individual emitters based on the autocorrelation of their temporal fluorescence fluctuations. Adapted with permission from ref. [214]

reconstruct an image with two–threefold improved resolution. This process leverages the fact that the fluctuations are uncorrelated in space, allowing for the separation of features that would otherwise be unresolved in traditional fluorescence microscopy (Fig. 12). Although classical SMLM outperforms SOFI in terms of resolution, SOFI enables high-speed SRM because it tolerates a wide range of blinking statistics and much lower SNRs [222]. Furthermore, SOFI is characterized by inherent optical sectioning which may be suitable for bright-field illumination and 3D imaging over a broad depth range [223].

Any stochastically "flickering" fluorophore can be in principle used for SOFI, and indeed the first demonstration of this technique made use of Q-Dots [223]. Yet, in 2012 Dedecker's group demonstrated that the flickering of RSFPs at a single molecule level, easily obtained by single-wavelength illumination as an effect of *on* ↔ *off* photosteady state, provided "a necessary, sufficient, and convenient way to achieve the requirements inherent to SOFI imaging" [224]. This approach has been referred to as "photochromic SOFI" (pcSOFI). In the last decade, several RSFPs have been applied to pcSOFI measurements, including Dronpa, ffDronpa and rsGreen [165, 225, 226], and Skylan-S [168]. pcSOFI was also combined with F-PALM by using the "combo" negative switching/green-to-red photoconverting pcDronpa and pcDronpa2 (Fig. 13) [103]. The Dedecker's group developed "SOFIevaluator", a neutral, automatic algorithm designed for computing various metrics that are instrumental in assessing the quality

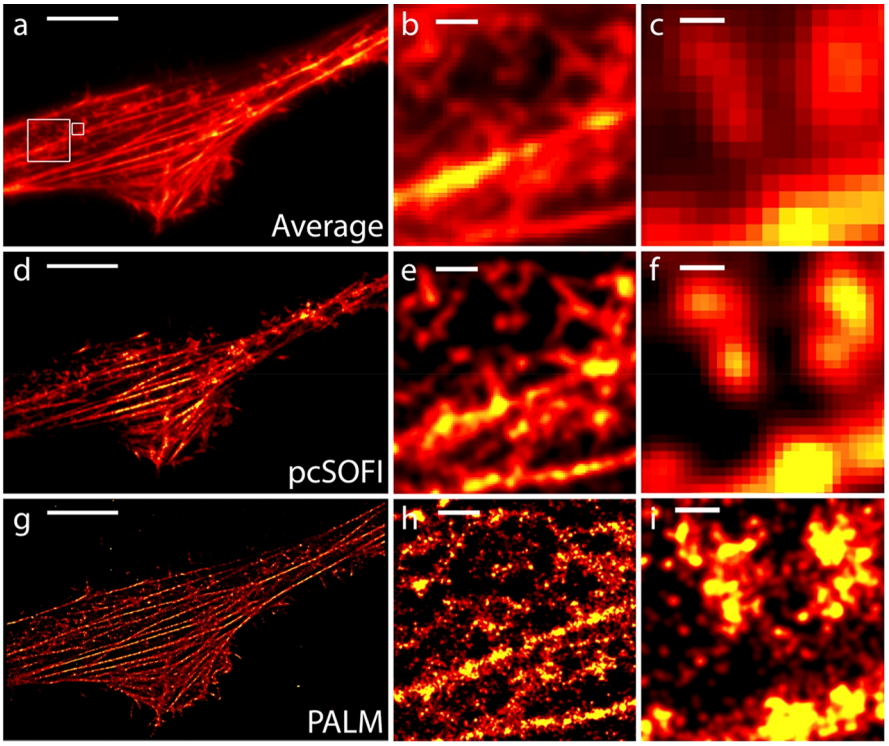

Fig. 13 pcDronpa enables SOFI and F-PALM acquisition on the same sample. pcDronpa2-labeled β-actin in HeLa cells is imaged by wide-field (**a**–**c**), pcSOFI (**d**–**f**), and F-PALM (**g**–**i**) microscopy. **b**–**h** and **c**–**i** Display details of the β-actin network. Scale bar: 10 μm (**a**, **d**, **g**), 1 μm (**b**, **e**, **h**), 0.3 μm (**c**, **f**, **i**). Figure reprinted with permission from ref. [103]. Copyright 2014 American Chemical Society

of super-resolution fluorescence imaging data for SOFI. By the same algorithm, 20 different "flickering" FPs, including several RSFPs, were evaluated, suggesting that SkylanS, ffDronpa and WQ have good/excellent compatibility with SOFI on account of high S/N ratio [227]. In a later paper by the same group, it was suggested that optimal image quality in SOFI is attained for fast RSFPs with low switching fatigue, which enables long measurement duration [228].

Of note, dual-color pcSOFI was carried out by discriminating the switching kinetics of two RSFPs with overlapping spectra [165], also in multiplexed mode with AFM and SMLM [229]. Here, the best results were obtained by combining rsGreen1 and rsKame, although the couples rsGreen1/Dronpa and ffDronpa-f/rsKame proved still adequate [229]. The ability to distinguish among different switching regimes in SOFI has been also exploited to generate a new class of biosensors, called FLINCs [230, 231]. In the FLINC scheme, the proximity of Dronpa (or a Dronpa mutant where the chromophore is inactive [231]) to TagRFP-T changes the fluorescence fluctuation behavior of the readout protein, thereby enabling super-resolution imaging with pcSOFI. By computing pairwise cross-cumulants using correctly matched pixel pairs, one can derive a metric similar to an autocorrelation, referred to here as the 'pcSOFI

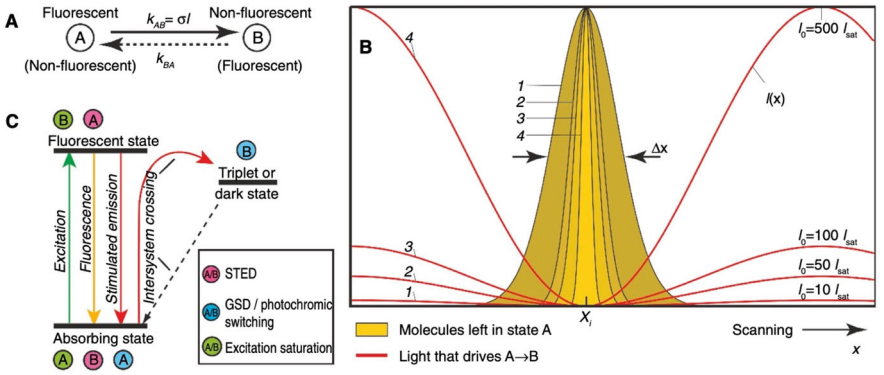

Fig. 14 The reversible saturable optical transitions (RESOLFT) concept. **A** RESOLFT requires two optically distinct fluorescent states A and B of a marker (here bright and dark). The optical transition from A to B takes place at a rate k_{AB} proportional to the applied light intensity I ($k_{AB} = \sigma I$). **B** A standing wave of light with zero intensity at x_i is applied with increasing power, from 10 to 500 times the intensity at which the transition saturated, i.e.: $I_{sat} = 1/\sigma\tau$. Profiles 1–4 show the spatial region in which the label is allowed to be in state A: increasing the intensity ensures that the region in which the label may reside in A is squeezed down, in principle, indefinitely. If A is the fluorescent state of the label, this ultrasharp region works as the effective fluorescent spot of the microscope and Δx is its FWHM. In any case, the resolution is no longer limited by diffraction, but only determined by the value of I_0/I_{sat}. The creation of a fluorescence image requires scanning that is moving the zero along the x-axis with subsequent storage of the recorded fluorescence. (C) The simplified energy diagram of a fluorophore depicts possible schemes for implementing saturable optical transitions, including photochromic switching. Reprinted with permission from ref. [232]

value' [165]. This metric, attainable at a resolution finer than a single pixel, is useful for measuring the intensity of fluctuations within the imaging data, which is in turn related to the metabolite-dependent proximity between Dronpa and TagRFP-T [230].

4.1.2 SRM approaches that leverage spatial-modulation of the excitation/emission

Reversible saturable optical fluorescence transitions (RESOLFT) microscopy
RESOLFT is a general concept of achieving super-resolution by properly shaping the excitation PSF and must be included in the family of coordinate-targeted SRM techniques. The mechanism of RESOLFT is easily explained by the following one-dimensional example taken from the original description of this technique (Fig. 14) [207].

We first consider a photoinduced transition $A \rightarrow B$ and we illuminate the sample with a (diffraction-light) light profile $I(x)$ which is zero for $x = x_i$: accordingly, the transition will occur everywhere except in x_i (Fig. 14). Now, we increase the intensity $I(x)$ so to almost saturate the transition everywhere. In such a case, significant fractions of state A will survive only in the vicinity of x_i, disappearing outside this narrow region in a *steep, non-linear fashion* (Fig. 14). If A is fluorescent, then fluorescence will be spatially confined as described. Let us now move the intensity zero across the specimen, reading out at the same time the fluorescence for each coordinate: this would provide

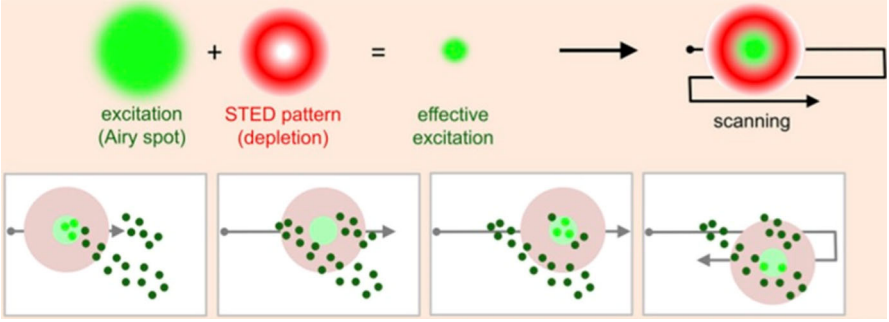

Fig. 15 The STED/RESOLFT imaging approach. In STED/RESOLFT the diffraction-limited excitation spot is overlaid with a doughnut-shaped that deactivates all the emitters in the periphery of the excitation spot, generating an effective excitation PSF which is then scanned across the sample. Adapted with permission from ref. [214]

a narrower "effective" excitation PSF that enables enhanced resolution even if the illumination is diffraction-limited (Fig. 15).

Clearly, this concept is not limited just to scanning microscopy: multiple nodes may be produced in the illumination profile and a camera-based parallelized imaging strategy can be adopted as well. It can be demonstrated that the RESOLFT resolution scales with the square root of the illumination, according to:

$$\Delta x \cong \frac{\Delta x_0}{\sqrt{1 + \frac{I}{I_s}}}, \tag{52}$$

where Δx_0 is the diffraction-limited resolution, I is the maximum intensity that promotes $A \rightarrow B$, and I_s is the "saturation intensity" of the transition [233]. I_s can be deduced as follows. The photoprocess $A \rightarrow B$ is linear, and its rate constant is $k_{AB} = \sigma_A I(x)$. Saturation depends critically on any process $B \rightarrow A$ which counteracts deactivation of A. Let us identify the deactivation rate constant of B with k_{BA} without stating any hypothesis on its origin. Then, saturation of $A \rightarrow B$ is achieved for $k_{AB} = \sigma_A I(x) \gg k_{BA}$. By defining $I_s = k_{BA}/\sigma_A$, we have:

$$I(x) \gg \frac{k_{BA}}{\sigma_A} = I_s. \tag{53}$$

Thus, I_s "weights" the extent of saturation promoted by $I(x)$ in each point, and is related to resolution through Eq. 52. For the sake of clarity, it is more convenient to rewrite I_s by considering the intrinsic lifetime τ_{BA} of the B state, that is:

$$I_s = \frac{1}{\sigma_A \tau_{BA}}. \tag{54}$$

The first major application of the RESOLFT approach has been STED microscopy [234, 235]. In STED, A and B identify with the excited and ground states of a molecule,

respectively (Figs. 14, 15). The $A \rightarrow B$ photoprocess is stimulated emission, which can be easily spectrally decoupled from spontaneous emission by depleting with photons on the red tail of the emission spectrum of the irradiated fluorophore [235]. $B \rightarrow A$ accounts for the spontaneous decay back to the ground state, which entails both radiative and non-radiative transitions and τ_{BA} is the fluorescence lifetime of the molecule. The depletion 2D/3D $I(x, y, z)$ "doughnut-shaped" illumination profile with a node in (x_0, y_0, z_0) is accomplished by putting in front of the objective an optical device leveraging light interference [234]. In spite of its general applicability, STED requires very strong depletion light as $\sigma_A \sim 10^{-17}$ cm^2 and $\tau_{BA} \sim 1$ ns, yielding $I_s \approx 100$ MW/cm^2 [207, 236]. Accordingly, STED is generally restricted to specialized fluorophores able to withstand the intense depletion laser for several cycles with little loss of fluorescence [73] and it is predominantly used for fixed biological specimens where cell viability is not an issue [237]. An alternative approach to produce lower photodamage in cells makes use of photochromic dyes, because in such a case: 1) the $A \leftrightarrow B$ transitions occur between ground states with $A \equiv on$, $B \equiv off$, and 2) $\tau_{BA} = 10^{-3} \div 1$ ms [207, 236], scaling down I_s by 3–6 orders of magnitude to values similar to those applied in live-cell confocal fluorescence microscopy [124]. This approach is widely referred to simply as RESOLFT and -for simplicity and consistency- we shall follow this nomenclature, although we should stress that RESOLFT is less a specific technique than a general concept (Fig. 14). From its original conception in 2005 by the Hell group [207], RESOLFT has targeted RSFPs as photochromic switchers, and several studies have been published in these 20 years. The reader is referred to the recent review by Jensen [17] for a comprehensive description of this topic. In the following, we shall discuss the main features of RSFP-based RESOLFT and provide some updated references.

Currently, the majority of RESOLFT methods depend on RSFPs that operate in a negative switching mode (Fig. 16) [17]. In such standard RESOLFT approaches, the fluorophores are activated in a sequential manner, albeit a wide range of optical configurations are exploited to improve SRM imaging, particularly of living specimens [104, 127, 147, 177, 238–240]. Consequently, following the initial activation to the *on*-state, RSFPs are turned *off* using a doughnut-shaped beam or a standing wave light pattern, and the "central" fluorophores that remain in the *on*-state are examined using a Gaussian-shaped focused beam (Fig. 16). The negative switching property implies that the central fluorophores are deactivated during the readout process. Therefore, it is often necessary to repeat the switching and readout sequence to gather enough photons, particularly if the expression levels are low. This procedure did not hamper complex imaging schemes. For example, dual-channel SRM imaging was achieved by leveraging the different switching kinetics and fluorescence lifetimes of otherwise spectrally overlapping Dronpa and rsEGFP variants, down to 60–70 nm [240]. In addition, molecular nanoscale live imaging with a sectioning ability (MoNaLisa) RESOLFT was specifically developed for parallelized RESOLFT imaging in 3D samples, (a 15 mm penetration in brain slices was demonstrated), by multifoci (3,600) illumination, which effectively blocks out-of-focus light, with a sinusoidal illumination pattern [239]. The parallelization concept behind MoNaLisa was recently shown to generate SRM images over fields of view as wide as $100 - 130\,\mu$m without compromising the resolution (45–65 nm) [241]. Most of these applications took advantage of

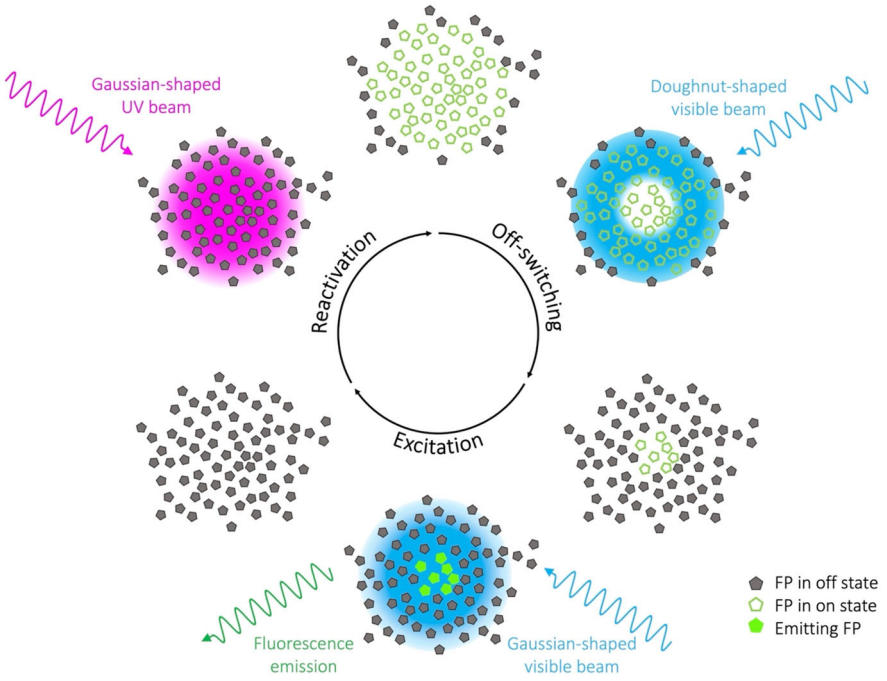

Fig. 16 Scheme of RESOLFT by negative RSFP. At the beginning of each cycle, in each spatial location, all the RSFPs are activated by short-wavelength (reactivation) light focused as a Gaussian-shaped beam. Then, RSFPs on the periphery are switched off by intense long-wavelength (excitation) light focused as a doughnut-shaped beam. Finally, fluorescence is generated by dim excitation light focused as a Gaussian-shaped beam. Thus, fluorescence comes only from those central molecules that survived the *off*-switching step. This optical cycle is repeated several times while the beam positions scan spatially the sample

the excellent switching properties of rsEGFP2, which afforded resolutions as low as ~ 40 nm in living cells (Fig. 17) [124, 147]. The switching properties of rsEGFP2 were leveraged to build a genetically encoded calcium sensor amenable to SRM imaging in living cells by RESOLFT with about 80 nm resolution [242]. The recent development of high-contrast, very photostable GMars RSFPs offered a further option to reach the < 80 nm resolution in living cells [127, 173]. The engineering of rsFusionReds paved also the way to effective MoNaLisa RESOLFT (50–70 nm resolution) with green/orange light, thereby avoiding both the moderately phototoxic 405 nm illumination and the autofluorescence-rich green region of emission spectrum observed in cells [126]. In a general sense, however, using negative RSFPs may be disadvantageous as it in general leads to longer image acquisition times and higher light exposure to the sample [187].

Positive RSFPs offer a solution to the issue of limited fluorescence detection per switching cycle. This is because the fluorescence excitation initiates the *on*-switching, allowing proteins at the center of the doughnut to remain in the *on*-state for an extended period during readout. To achieve subdiffraction resolution in this setup, it is sufficient to combine the regular focused excitation light with a doughnut-shaped *off*-switching beam, to keep the molecules at the periphery in the off-state. These two interlaced

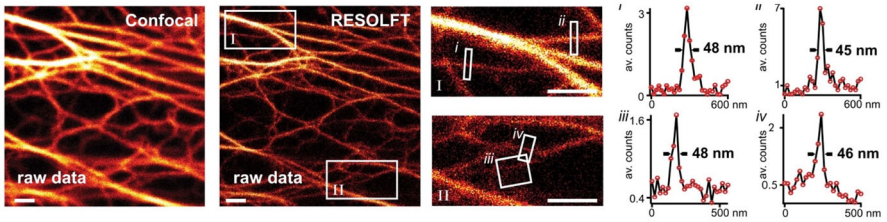

Fig. 17 Scheme of RESOLFT by negative RSFP. Keratin19-rsEGFP2 expressed in PtK9 cells was imaged in confocal and RESOLFT modes. From left to right: confocal raw image and corresponding raw RESOLFT image. Magnifications of the boxed areas in the RESOLFT image. The graphs show averaged line profiles across the indicated filaments (i–iv) within the respective boxes. Reprinted with permission from ref. [124]

beams could be simultaneously moved across the sample to capture an SRM image, eliminating the need for sequential illumination steps. Accordingly, this method has been termed "one-step" RESOLFT nanoscopy [187]. Although the first demonstration of RESOLFT has leveraged the positive switcher asFP595 [207], until very recently none of the reported positive RSFPs displayed switching performances complying with RESOLFT, namely: high contrast, low switching fatigue, high quantum yield in the *on* state, and slow -if any- spontaneous recovery from the *off* state [163, 175, 192, 243]. Kohinoor was indeed applied to generate SRM maps achieving 85 nm resolution, but still by a sequential RESOLFT approach, although it simplified the optical setup (only a 488-nm confocal and a 405-nm doughnut laser line) compared to negative switchers [191]. In 2021, however, Jakobs' group applied the newly engineered mutant Padron2 to achieve a 60–75 nm resolution in living cells. Although this performance cannot compare with the resolutions exhibited by negative RSFPs such as rsEGFP2, Padron2 is a promising step towards more effective RESOLFT imaging.

Structured illumination microscopy (SIM and SSIM) SIM is an advanced SRM technique that involves diffraction-limited pattern illumination of the specimen, generating a beat pattern (Moiré fringes) in the resultant image [14, 244]. This pattern contains information about the spatial frequencies of the object that exceed the diffraction limit. Since the structure of the illumination pattern is known, these frequencies can be extracted from the captured image. Given that the spatial frequencies of both the object and the illumination patterns are diffraction-limited, SIM resolution enhancement is approximately twofold, assuming a minor Stokes shift between excitation and emission [245]. For image reconstruction, 2D SIM needs a minimum of nine exposures, while 3D SIM requires at least fifteen [12, 246]. The specimen must be static during these exposures, a fact that restricts SIM mostly to fixed cells. Yet, the advent of high-speed cameras has made live-cell imaging increasingly practical [247].

Resolution enhancements > 2 can be obtained by exploiting the saturability of fluorescence emission, according to the technique developed by Gustafsson and named saturated structured illumination microscopy (SSIM) [248]. Although original SSIM was based on the emission saturation of photostable fluorophores, this approach can be easily extended to the saturation of photoswitching processes in RSFPs, analogously to the conceptual step from STED to photochromic RESOLFT [249]. Gustafsson has

pioneered in 2011 this strategy by using Dronpa and obtaining about 60 nm resolution in fixed samples [246]. A few years later Betzig and coworkers reached 45–60 nm in fixed and living cells using the improved negative switcher Skylan-NS, [151, 250].

4.2 Special applications of RSFPs

4.2.1 Photochromic FRET and optical lock-in detection (OLID)

Förster Resonance Energy Transfer (FRET) is a method of spectroscopy that can be readily integrated into fluorescence microscopy, making it particularly effective for examining biomolecular interactions in solutions, live cells, and tissues [251]. The principle of FRET involves the non-radiative energy transfer from an excited molecular fluorophore, known as the donor (D), to a chromophore, referred to as the acceptor (A), through long-range dipole–dipole coupling [252]. In many applications, the acceptor is also fluorescent, but this is not a necessary condition for FRET to take place. Förster's theory predicts that the efficiency E of FRET is inversely proportional to the sixth power of the separation (r) between the transition dipole moments of D and A [252]:

$$E = \frac{R_0^6}{R_0^6 + r^6}, \tag{55}$$

where R_0 is a parameter, named Förster's radius, which represents the D-A distance at which $E = 0.5$. R_0 is related to the photophysical properties of D and A according to [253]:

$$R_0 = 0.02108\left[J \cdot \frac{\kappa^2 \Phi_D}{n^4}\right]^{1/6}, \tag{56}$$

where Φ_D is the quantum yield of the donor (for non-fluorescent D, $\Phi_D = 0$ and $R_0 = 0$), n is the refractive index of the medium, κ^2 is the so-called *orientation factor* between the donor's and acceptor's transition dipoles [252], and J is the "overlap integral" J, i.e. the spectral integral of the product of donor's normalized emission $\overline{F_D}(\lambda)$ and acceptor's absorption $\varepsilon(\lambda)$ weighted by the fourth power of wavelength:

$$J = \int \overline{F_D}(\lambda) \cdot \varepsilon(\lambda) \cdot \lambda^4 d\lambda; \int \overline{F_D}(\lambda) d\lambda = 1. \tag{57}$$

Good donor/acceptor (D/A) pairs with a significant overlap integral in the visible spectrum range can yield $R_0 = 5 - 7$ nm. This capability offers a method to discern molecular interactions (i.e., proximities) up to 10–12 nm, significantly surpassing the optical diffraction limit. Typically, the donor (D) and acceptor (A) are exogenous fluorophores attached to target biomolecules, such as proteins. Detecting FRET in specific areas of a microscopy image strongly suggests that the donor and acceptor-labelled molecules are part of a complex. Furthermore, the quantitative assessment of

E, along with the known R0 for the D/A pair and the configuration of D and A fusion constructs, can yield valuable structural insights into the complex, for example the average distance between the D and A (Eq. 55).

Over time, various techniques have been developed to quantitatively measure FRET efficiency [251, 254–257]. Among others, the development of photochromic organic fluorescent dyes enabled a new method for quantitative FRET, named photochromic FRET (pcFRET) [258, 259]. pcFRET is defined as FRET carried out in the presence of either a photochromic donor (D-pcFRET) or a photochromic acceptor (A-pcFRET). Modulations of fluorescence emission by D can be induced by reversible switching of A (A-pcFRET), whereas the opposite pattern holds for D-pcFRET (Fig. 18). Both approaches afford the quantitative and repeatable determination of the FRET efficiency between two molecules without the need to apply corrections based on reference images [259]. The use of RSFPs in A-pcFRET was pioneered by both Bizzarri [117] and Subach in 2010 [176]. Bizzarri and coworkers developed the negative switcher EYQ1, possessing YFP spectral characteristics, and demostrated its utility as a strong acceptor in couple with donor EGFP ($R_0 = 5.64$ nm) to reveal intense (30%) FRET in living cells by looking at the anticorrelated switching of D and A. Similarly, Subach

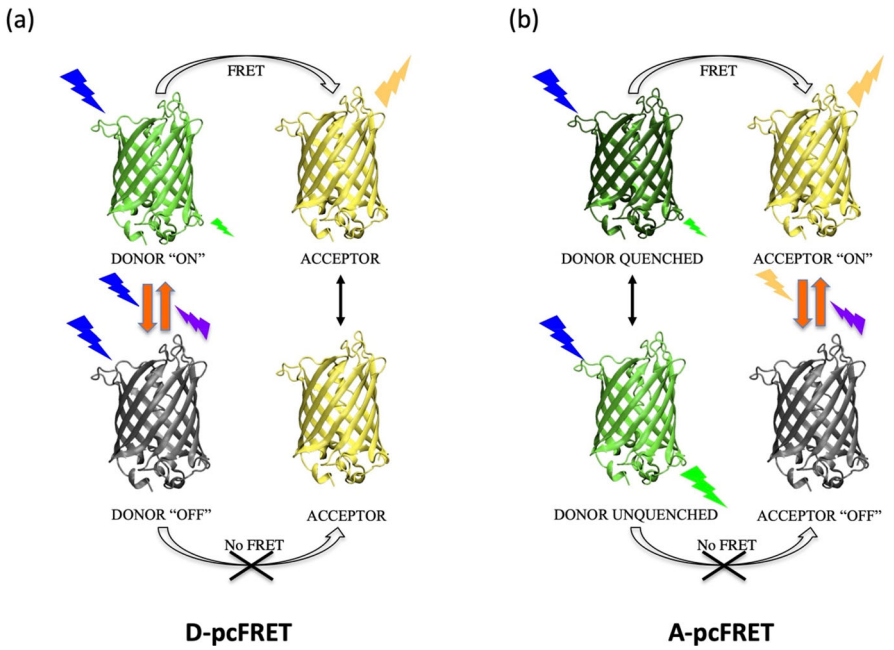

Fig. 18 Principle of pcFRET. Scheme of pcFRET between a green fluorescent protein (GFP) donor and a yellow fluorescent protein (YFP) acceptor. **a** D-pcFRET: the donor is photochromic, and FRET ensues only when the donor is in the *on* state. **b** A-pcFRET: the acceptor is photochromic, and FRET ensues only when the acceptor is in the *on* state. Note that in both cases the Donor emission is always modulated by the photoswitching process: in D-pcFRET this is a constitutive property of the Donor; in A-pcFRET this property stems from the FRET-quenching/dequenching originated by the Acceptor photoswitching. Reprinted with permission from ref. [261]

and coworkers engineered rsTagRFP as an acceptor of donor EYFP, monitoring both the donor intensity and lifetime. Of note, A-pcFRET relies only on the photochromic change in the *absorption* spectrum of the acceptor, which needs not to be fluorescent. Indeed, Don Paul and coworkers have developed Phanta, a non-emissive negative switcher similar to EYQ1, which can work as a non-fluorescent acceptor of EGFP donor in A-pcFRET [260].

Experiments on D-pcFRET have been carried out either by direct monitoring of the modulated emission of either the Donor or the Acceptor. Interestingly, Bizzarri and coworkers [132] applied EYQ1 as a Donor in Optical Lock-In Detection (OLID) microscopy to visualize intracellular FRET. OLID has been developed to isolate modulated (AC) fluorescence signals against a large, non-switching, background (DC) [262–265]. Practically, OLID requires the deterministic control of the fluorescence of a photochromic emitter through optical modulation and a digital or post-processed lock-in detection to enhance the components of the AC signal in sync with the switching reference function with respect to the DC contribution. By OLID-FRET, Bizzarri and coworkers have confirmed the existence of a complex between the nociceptor TRPV1 (linked to EYQ1) and microtubules (α-tubulin linked to TagRFP) (Fig. 19) [132].

Of note, the same group leveraged OLID as a way to separate out the signals of two spectrally similar FPs, only one of which is amenable to reversible photoswitching [112]. The Dedecker's group has recently published a study that pioneers the use of an RSFP donor to distinguish spectrally overlapping FRET pairs in multiplexed biosensing [266]. Their approach relied on the determination of the switching contrasts for both the donor and the acceptor as a way to compute according to the sensitized emission theory. Remarkably, this strategy was applied to imaging in living cells cAMP-dependent protein kinase (PKA) and extracellular signal-regulated kinase

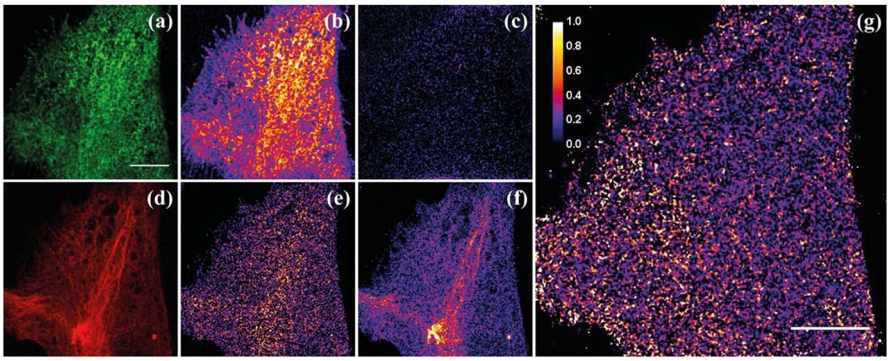

Fig. 19 OLID-FRET by using the negative switcher EYQ1. TRPV1-EYQ1 (donor, D) and TagRFP-α-tubulin (acceptor, A) were expressed in CHO and six photochromic *on–off* cycles were repeated, acquiring emission during the *off*-switching phase. **a** Average of D channel. **b** Switching fraction in the D channel. **c** Non-switching fraction in the D channel. **d** Average of A channel. **e** Switching fraction in the A channel. **f** Non-switching fraction in the A channel. **g** Map of FRET efficiency. Scale bar 10 μm. Reprinted with permission from ref. [132]

(ERK) activities in living cells by two spectrally identical FRET biosensors, one of which is based on the photoswitchable mTFP0.7 variant as donor [266].

When an acceptor is situated near a photoswitchable donor, it creates an alternative route for energy transfer, which interferes with the donor's ability to switch *off*. This leads to a slower *off* photoswitching rate of the donor molecule [266, 267]. This effect has been exploited by Patterson's group to monitor FRET between Dronpa (D) and mCherry (A) at the intracellular level [267]. Dronpa was selected for its high contrast and slow $on \rightarrow off$ photoswitching rate, which may facilitate the detection of the photoswitching kinetics. Of note, the authors validated their strategy by comparison with several other methods of FRET detections [267]. In addition, they reported significant FRET between histone H2B conjugated either to Dronpa or to mCherry, hinting at FRET interactions occurring between neighboring nucleosomes or nucleosomes brought together by higher-order chromatin folding [267].

4.2.2 Viscosity sensing

In 2012, Kao and coworkers revealed that the photoswitching rate of Dronpa and its mutant Dronpa-3 decreases upon the increase of medium viscosity [268]. This finding hints at an existing relationship between photoswitching and β-barrel plasticity, as lately described by Chang [120]. In keeping with this view of dynamic flexibility as determined in the photoswitching, Mizuno et al. revealed that the kinetics of photoswitching in Dronpa variants are strongly related to the self-association of the proteins [166].

Dronpa-3 was particularly sensitive to viscosity changes, as an increase of glycerol in the medium from 0 to 90% led to a fourfold slower *off*-switching of the protein [268]. Dronpa-3 was therefore suggested as a genetically encoded reporter for microviscosity in cells, and a preliminary study demonstrated the heterogeneus compaction of chromatin in the nucleus [268].

4.2.3 Photochromic anisotropy

Fluorescence anisotropy decay is part of a broader category of relaxation techniques that track how a system evolves over time from an initially biased state to a random configuration. In short, let us consider a pulse excitation by plane-polarized light of an ensemble of randomly oriented fluorophores. For each molecule, the likelihood of absorption is directly related to $\cos^2\varphi$, where φ is the angle between the incident light and the absorption transition dipole. Thus, absorption of linearly polarized leads to photoselection, i.e. only a subset of molecules will reach the excited state with a probability weighted by $\cos^2\varphi$. If the molecules do not rotate, their radiative decay will produce a partially polarized fluorescence, because each emission transition dipole has a fixed geometrical relationship with the absorption transition dipole. Yet, if the molecules do rotate, we must consider emission depolarization due to progressive randomization of the orientations of the emission transition dipoles. The polarization degree of the emitted light is measured by the fluorescence anisotropy r, which is

defined as [269]:

$$r(t) = \frac{I_{\parallel}(t) - GI_{\perp}(t)}{I_{\parallel}(t) + 2GI_{\perp}(t)}, \tag{58}$$

where $I_{\parallel}(t)$ and $I_{\perp}(t)$ are the (time-dependent) emission intensities parallel and perpendicular to the polarization direction of the excitation light, respectively; G is a factor that considers the different collection efficiency along the parallel and perpendicular direction. It is easy to show that [270]:

$$r(t) = r_0 \frac{3\overline{\cos^2\omega(t) - 1}}{2}, \tag{59}$$

where the fraction represents the depolarization autocorrelation function, i.e. the probability that the emission dipole of a molecule will be oriented at $\omega(t)$ with respect to its orientation at time zero. r_0 is said to the fundamental anisotropy, and it is related to the angle α between the absorption and transition dipole by:

$$r_0 = 0.4 \frac{3\cos^2\alpha - 1}{2}. \tag{60}$$

For a free isotropic rotor with rotational diffusion coefficient D_r, the theory shows [270]:

$$r(t) = r_0 e^{-t/\tau_r}, \tag{61}$$

where the characteristic time $\tau_r = 1/6D_r$. If constant excitation is applied, the time dependence of anisotropy drops, and we obtain Perrin's equation for "static" anisotropy:

$$\overline{r} = r_0 \left(1 + \frac{\tau}{\tau_r}\right)^{-1}, \tag{62}$$

where τ is the fluorescence lifetime of the fluorophore, which we suppose to decay monoexponentially from the excited state (Eq. 62) can be easily extended to fluorophores characterized by multiexponential emission decays). A simple expression of D_r is provided by the Stokes–Einstein equation holding for spherical rigid rotors:

$$D_r = \frac{RT}{6V\eta}. \tag{63}$$

In Eq. 63 V is the volume of the rotor, whereas η is the viscosity of the solution. The Stokes–Einstein equation can be generalized by considering V as the empirical "hydrodynamic volume" of any rotor. Finally, the Perrin equation becomes [269]:

$$\overline{r} = r_0 \left(1 + \tau \frac{RT}{V\eta}\right)^{-1}. \tag{64}$$

Anisotropy measurements to probe large molecular sizes Equation 64 shows that static anisotropy posits an interesting method to estimate the molecular size of rotating molecules, as originally proposed by Perrin [271]. Indeed, fluorescence anisotropy, in both static or time-resolved approaches, is particularly useful to reveal mass changes related to molecular binding. For this reason, it is widely applied in microscopy and enables several life-science applications such as drug screening (for a comprehensive review, see [271]). Yet, the dynamic range of anisotropy change with rotor volume is critically dependent on the τ/τ_r ratio, on account of τ_r scaling with the third power of molecular radius (Eq. 64). This means that the measurement of very large volumes (characterized by large τ_r values) is possible only if the lifetime is large as well. The slowest decaying FPs exhibit $\tau \sim 4$ ns [272]. Assuming that anisotropy changes as low as 5% can be measured with adequate S/N ratio, this implies a maximum $\tau_r \approx 75$ ns. For proteins, we may consider $V \approx 2M\overline{v}$, where M is the molecular weight in Dalton and $\overline{v}$ is the specific volume of the protein (~ 0.735 ml/g [273]). With $\eta = 0.94$ cP and $T = 37°$, we calculate that $M \approx 140$ kD. Thus, anisotropy measurements leveraging FPs are unable to detect all those large mass changes (several hundreds of kDa) that frequently occur in the eukaryotic proteome as a result of multiple protein binding (e.g. the assembly of multiple transcription factor within specific chromatin loci), because the molecular complexes rotate too slowly to produce significant changes in the polarization of the emitted light. Replacing FPs with other fluorophores does not alleviate this problem, since most organic fluorophores display fluorescence lifetimes well below 5 ns [274] and -given their usual small size- they experience high rotational freedom (and very low τ_r) even when conjugated to much larger biomolecules.

To address this issue, Testa's group has very recently developed an approach named selective time-resolved anisotropy with reversibly switchable states (STARSS), which extends the observable mass range by more than three orders of magnitude by using RSFPs [275]. STARSS leverages photoselection of *on* ↔ *off* transitions in fast switcher rsEGFP2 and Dronpa M159T by linearly polarized light, to subsequently probe depolarization along the photoswitching kinetics occurring with a μs to s timescale depending on the illumination intensity. Three different imaging schemes (STARSS 1,2,3) were developed (Fig. 20). In STARSS 1, after switching *off* all proteins by non-polarized 488-nm light, *off* → *on* reactivation was photoselected in a subset of proteins by using a short pulse (250 μs) of linearly polarized 405-nm light and the slow time-dependent depolarization of these emitters along *on* → *off* photoswitching was probed by non-polarized 488-nm light; (2) the illumination scheme was the same as in (1), but now the reactivation light was not polarized, whereas the probing 488-nm light was polarized to photoselect aligned dipoles for switching *off* so as to induce an artificial depolarization in the system; (3) the illumination scheme was the same as in (1), but *two* short 405-nm pulses, separated by a variable time lag (0.2–500 μs), were applied, and the following emission along *on* → *off* photoswitching was integrated, to provide a static anisotropy signal dependent on the rotation extent of molecules during the applied time lag. Imaging scheme (2) afforded a large photon budget since early 405-nm photoselection was not required and all the molecules were probed. Scheme (3) enabled monitoring faster kinetics. STARRS has been applied to characterize the rotational mobility of several molecular complexes in cells, including the retroviral Gag lattice and chromatin in interphase and during mitosis [275]. Of note, data hinted

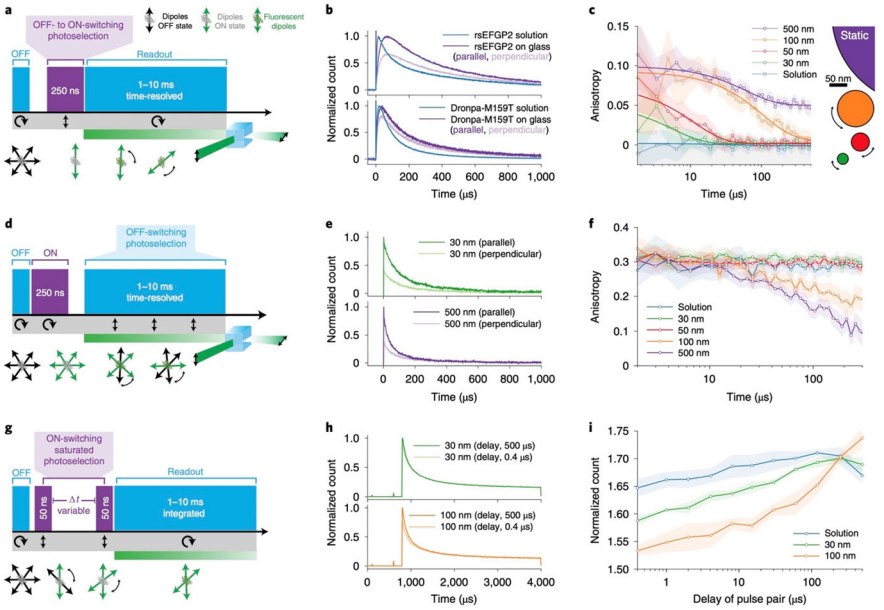

Fig. 20 Selective time-resolved anisotropy with reversibly switchable states (STARSS). **a** STARSS method 1 pulse scheme with photoselection during ON-switching, circular cyan light for probing and polarization-sensitive, two-channel detection. **b** Experimental raw data recorded with STARSS method 1, showing distinct relaxation of the parallel and perpendicular channels for Dronpa-2 and rsEGFP2 after *on*-switching photoselection. **c** STARSS method 1 experiments on beads of varying diameter. The logarithmic x axis shows the extended temporal observation window up to 500 µs, which allows measurement of tumbling of spheres of diameter 30–100 nm (500-nm beads are a reference static sample). **d** STARSS method 2 pulse scheme with photoselection during *off*-switching, and with circular *on*-switching and polarized-sensitive detection. **e** Detected raw signal recorded with STARSS method 2 for beads of varying size, reporting the decay of parallel and perpendicular channels. **f** STARSS method 2 experiments on beads of varying diameter. **g** STARSS method 3 consists of photoselection with polarized *on*-switching pulses delivered at two distinct time points and circular cyan light to read out the fluorescence detected with polarized-sensitive detection. **h** Detected raw signal with STARSS method 3 under two delay conditions for beads of varying size. **i** STARSS method 3 curve derived from beads of varying size. The information on rotational diffusion is encoded in the count increase for different delays between ON-switching pulses. Counts are normalized by the signal obtained from a scheme with a single ON-switching pulse. Shaded regions of anisotropy values are 95% confidence intervals evaluated from detector noise. Reprinted with permission from ref. [275]

at a continuous spectrum of hydrodynamic diameters exhibited by nucleosome core particles.

Anisotropy measurements to probe protein oligomerization Protein oligomerization plays a role in various cellular processes, and having simple, reliable, and precise methods to observe these interactions enhances our comprehension of protein behavior. Homogeneous Förster Resonance Energy Transfer (HomoFRET) is an interesting variant of FRET where energy transfer occurs between identical fluorophores, provided a large overlap between the excitation and emission spectra and close molecular proximity [276, 277]. In HomoFRET no changes in the intensities or lifetimes of the

molecules are produced. Yet, multiple energy transfers between fluorophores adopting random mutual orientations leads to depolarization. Accordingly, HomoFRET can be applied to probe the oligomerization status of fluorophores endowed with small Stokes' shift, as elegantly demonstrated by Runnels and Scarlata in 1995 [277, 278]. The great advantage of HomoFRET is leveraging identical fluorophores because it only needs one fluorescence channel to track protein oligomerization.

In the biological context, HomoFRET has been repeteadly applied to probe protein oligomerization by using genetically encodable FPs [276]. Indeed, the high rotational characteristic time of FPs ($\tau_r \sim 36$ ns at intracellular level [279, 280]) ensures low depolarization due to motion within the emission lifetime, and the observed drop in anisotropy upon oligomerization can be mostly attributed to HomoFRET [281]. Classical HomoFRET microscopy has some drawbacks, tough. The most critical is surely the loss of anisotropy due to high numerical aperture (NA) objectives, which often forces the experimentalist to use low NA at the expense of optical resolution [282, 283]. This and other issues of HomoFRET microscopy have been addressed by a recent work of Patterson's group, which introduced photoswitching Anisotropy FRET (psAFRET) [284]. psAFRET strategy makes use of an RSFP to bestow upon anisotropy slow kinetics related to photoswitching. Indeed, when all interacting molecules are in the *on* state, they transfer energy between each other yielding a decreased anisotropy. Increasing the population of photoswitched-*off* FPs leads to lower HomoFret and higher anisotropy. Patterson and coworkers used several chimeras containing two or more Dronpa molecules and verified that anisotropy linearly increased with the *off*-photoswitched population due to HomoFRET [284]. This linear behavior enabled the inner calibration of any experiment, as the extrapolated anisotropy at 100% *off* protein corresponds to the intrinsic anisotropy of the Dronpa's chimera under observation. From this, Patterson and coworkers calculated a quantity, drFRET, which represents the percentage increase in fluorescence signal in the perpendicular channel compared with the total signal [284]. Like anisotropy, drFRET increases as result of less HomoFRET along *off*-photoswitching, but it was found to be much less affected by polarization mixing due to the high NA of the objective. Thus, drFRET can standardize the same homo-FRET measurements made across different optical configurations.

4.2.4 Optogenetics

In the search for alternatives to Dronpa for F-PALM applications, Mizuno and coworkers developed in 2010 the Dronpa L145N mutant PDM1-4. The slower *off*-photoswitching of PDM1-4 compared to its parent protein was explained by its tetrameric quaternary structure and the structural/photophysical coupling between the assembly interface and *cis–trans* isomerization of the chromophore [166, 285]. Remarkably, Lin's group demonstrated that *off*-photoswitching let to the disassembly of tetrameric PDM1-4 to give four monomeric proteins in the *off* state. Reactivation to *on* state restored the tetrameric structure of the protein. The reversible photoinduced assembly/disassembly of PDM1-4 opened the way to the use of RSFPs in optogenetics. At first, Lin's group developed an approach where an enzyme domain was genetically tethered to Dronpa at one end and to PDM1-4 at the other end [11]. This strategy enabled "caging" of the enzyme domain through the formation of a Dronpa/PDM1-4

dimer in the *on* state of both proteins. Vice-versa, in the *off* state the two proteins split, restoring the enzyme's activity. To demonstrate the generality of this approach, optogenetic caging was applied to regulate intracellularly intersectin, a guanine nucleotide exchange factor that activates Cdc42, and the hepatitis C virus (HCV) NS3-4A protease [11]. The same researchers expanded the optogenetic toolbox by developing a photodissociable dimeric Dronpa domain, pdDronpa1, by rationally introducing mutations to break the antiparallel dimer interface and strengthen the cross-dimer interface in Dronpa145N [286]. Since its conception, pdDronpa1 has attracted growing interest in controlling specific cellular activities. By strategically placing two pdDronpa1 domains within the kinase domain, Lin and coworkers engineered a set of photoswitchable kinases (psRaf1, psMEK1, psMEK2, and psCDK5), which were applied to control several intracellular processes and to develop an optogenetic cellular assay to test kinase inhibitors [286]. The same group also generated single-chain photoswitchable Cas9 (ps-Cas9) chimeras in which the DNA-binding cleft was optically caged/uncaged, enabling light-induced transcriptional activation [287]. Ju and coworkers developed a photochromic RhoA guanine nucleotide exchange factor, investigating the role of RhoA activity levels in promoting focal adhesion disassembly [288]. Of note, a recent study using atomic force microscopy (AFM)-based single molecule force spectroscopy (SMFS) suggested that the dimer association of pdDronpa1 can be controlled by light as well as by force, opening to possible optogenetical applications of this protein in biomechanics.

5 Conclusions

Fluorescence proteins (FPs) and their applications in fluorescence microscopy have revolutionized the biology of cells, due to the genetic encoding of fluorescence that allows for labeling almost any protein by creating fusion constructs. The genetic encoding of fluorescence, nonetheless, enabled an even further intriguing possibility: changing the sequence of FPs to tailor their photophysical features to the targeted imaging strategy. In this context, a peculiar role is played by FPs that can be photoconverted between two different optical states (Photo-Transformable Fluorescent Proteins, PTFPs [9]). Accordingly, another degree of freedom (i.e., the temporal dimension) can be introduced in fluorescence microscopy techniques. The two optical states can be distinguishable due to fluorescent emission with different colors, distinct polarizations, different quantum yields of fluorescence emission (in particular a bright *"on"* state and a dark *"off"* state), etc. Among the PTFPs, two main groups of photoconvertible proteins can be identified: the irreversibly Photo-Activatable Fluorescent Proteins (PAFPs), whose change of optical state can be induced only once, and the Reversibly Switching Fluorescent Proteins (RSFPs), which instead can photoswitch several times [289].

By exploiting the bistability of PTFPs, new imaging methods able to break the diffraction limit of resolution [14, 15] have been conceived. Yet, even if the phototransformation capability of the fluorophore is a necessary requirement to acquire super-resolved images, it is not a sufficient condition. Indeed, super-resolution techniques require probes with specific features, whose "optimization" differs depending

on the imaging method. In this context, RSFPs are much more flexible, due to the additional degree of freedom given by the modulable activation-deactivation feature [17]. Even at conventional resolutions, RSFPs can be applied to strongly improve signal contrast technique [132, 263], or yield a clean FRET image just by exploiting the alternate modulation of the fluorescence [117, 176].

In this review, we tried to outline the genesis of the photochromic behavior, starting from the basic photophysical properties of the *Aequorea* GFP (wtGFP) and addressing the subtle structure–property relationships that unleash and modulate the photoswitching ability. We provided also a simple mathematical framework that rationalizes the macroscopic observations, and we described in some detail several protein variants developed in the last 20 years. We did not pretend to be exhaustive, but rather to afford a clear and balanced picture of the main switching phenotypes and their molecular determinants, if known. We believe that the accurate knowledge of the photoswitching mechanism, as well as of concepts such as the photoswitching yields, the fatigue resistance, the thermal recovery at ground state is fundamental to guide the experimentalist either in choosing the best reporter for the desired application, or to further engineer the protein sequences and generate new, improved, mutants. Of note, we dedicated a full chapter to the most exciting fields of application enabled by the RSFPs, among which super-resolution imaging definitely constitutes the largest share.

What is next in this exciting field? We believe this question is particularly crucial. For a start, we must say that the evolution of RSFPs to date has taught a clear lesson: the photoswitching ability can surely be optimized by random mutagenesis of the FP sequence followed by screening, but the real breakthroughs have come when the knowledge of structure–property relationships was put into service of protein engineering. Thus, full photophysical characterization of all these processes that underlie the optical photoswitching is essential, and the recent developments of ultrafast spectroscopy coupled with X-ray analysis (e.g. serial femtosecond crystallography SFX, [131]) hold promise to unveil other crucial details to guide protein engineers. We should note that for most variants the *onoff* mechanism is much less clear that its *offon* counterpart, on account of a significantly lower photoswitching yield that has prevented generalizable ultrafast characterization insofar [143]. Another key issue is the development of novel positive photoswitching variants. In principle, positive RSFPs enable simpler imaging schemes particularly in super-resolution, but—with few exceptions—their switching properties do not keep up with those exhibited by negative RSFPs [187]. Yet, the mechanism at the basis of positive switching is subtler, as it involves unusual stabilization of the negative form of *trans* chromophore [143]. "Combo" approaches that mix reversible switching with irreversible phototransformation have been described in literature, but their use in optical imaging is still quite limited, likely because of the conservative approach of many experimentalists toward applying new probes in non-conventional imaging schemes. In this sense, the development of variants whose mutation pattern and optical properties are close to popular non-switching variants looks promising to lower the hesitancy of researchers toward the use of novel, improved, RSFPs.

Last, we must say that our ability to take advantage of the novel dimension supplied by switching could be still in its infancy. In a recent commentary [4], Konstantin Lukyanov, renowned for his contributions to FP engineering, has drawn an insightful

analogy with DNA sequencing. This technique has evolved from Sanger sequencing, which deals with single purified DNA fragments and therefore requires extraordinary efforts for whole genome sequencing, to Next Generation Sequencing (NGS) approaches based on simultaneous analysis of complex mixtures of DNA molecules, which afford whole genome sequencing by routine. In optical imaging, Lukyanov says, we are at the "Sanger sequencing" stage: proteins are labeled specifically and detected one-by-one. The future holds the promise of a "Next Generation Imaging" (NGI) revolution, where several, if not all, cell proteins could be visualized in a single experiment by combining experimental measurements along several contrast dimension with artificial intelligence This idea echoes the "liquid tunable microscopy" (liquitopy) approach recently proposed by Alberto Diaspro, who also posits the relevant role of label-free imaging [15].

Will all this become reality? We cannot say now. But we are optimistic, as we have lived and worked in exciting years where two revolutions, FPs and super-resolution, have changed our perception and study of the biological realm. In both, reversible photoswitching played a key role. It is even curious that it took some time after their discovery to revolutionize imaging. Yet, this is far from being an uncommon story in science. In the summer of 1609, Galileo Galilei learned that some Dutch eyeglass makers had created a curious optical instrument: a tube equipped with two lenses at the ends, looking through which distant objects appeared closer. As soon as he knew the construction details, Galileo dedicated himself to perfecting the instrument, managing to increase its magnifying power in just a few months. However, it was only towards the autumn of 1609 that Galileo performed an unprecedented act: driven by scientific curiosity, he pointed his perfected instrument towards the sky. It is said that Galileo was amazed by what he could finally see: the known stars revealed unexpected physiognomies and new stars were added to those of the old Ptolemaic Cosmos. It was the dawn of a new scientific era.

Acknowledgements Dr. Paolo Bianchini, Prof. Cristiano Viappiani and Prof. Alberto Diaspro are gratefully acknowledged for their useful discussions. The Italian Ministry of University and Research is gratefully acknowledged for funding this work through the grant PRIN 2022 "Novel protein-based Genetically-Encoded Fluorescent Indicators (GEFI) for Functional Super-Resolution Imaging of Biomolecular Activities in Living Cells"—GEFinder (BIZZARRI_2022RRFJC4, CUP I53D23003880006).

Author contributions All authors contributed to the study's conception and design. Material preparation, data collection and analysis were performed by all authors. The first draft of the manuscript was written by Ranieri Bizzarri and all authors commented on previous versions of the manuscript. All authors read and approved the final manuscript.

Funding Open access funding provided by Università di Pisa within the CRUI-CARE Agreement. This work was supported by PRIN 2022 "Novel protein-based Genetically-Encoded Fluorescent Indicators (GEFI) for Functional Super-Resolution Imaging of Biomolecular Activities in Living Cells" –GEFinder, (BIZZARRI_2022RRFJC4, CUP I53D23003880006).

Data availability The bibliographical search information dataset analysed during the current review study is available from the corresponding author upon reasonable request.

Declarations

Conflict of interest The authors have no relevant financial or non-financial interests to disclose.

References

1. M. Chalfie, Angew. Chem. Int. Edit. **48**(31), 5603 (2009)
2. M. Chalfie, Y. Tu, G. Euskirchen, W.W. Ward, D.C. Prasher, Science **263**(5148), 802 (1994)
3. E.A. Rodriguez, R.E. Campbell, J.Y. Lin, M.Z. Lin, A. Miyawaki, A.E. Palmer, X.K. Shu, J. Zhang, R.Y. Tsien, Trends Biochem. Sci. **42**(2), 111 (2017)
4. K.A. Lukyanov, Biochem. Biophs. Res. Co **633**, 29 (2022)
5. R.Y. Tsien, Annu Rev. Biochem. **67**, 509 (1998)
6. O. Shimomura, Angew. Chem. Int. Edit. **48**(31), 5590 (2009)
7. K.A. Lukyanov, D.M. Chudakov, A.F. Fradkov, Y.A. Labas, M.V. Matz, S. Lukyanov, Discovery and properties of GFP-like proteins from nonbioluminescent anthozoa, in *Green Fluorescent Protein: Properties, Applications, and Protocols*. ed. by M. Chalfie, S.R. Kains (John Wiley & Sons Inc, Hoboken, 2006), p.121
8. D.M. Chudakov, M.V. Matz, S. Lukyanov, K.A. Lukyanov, Physiol. Rev. **90**(3), 1103 (2010)
9. K.A. Lukyanov, D.M. Chudakov, S. Lukyanov, V.V. Verkhusha, Nat. Rev. Mol. Cell Biol. **6**(11), 885 (2005)
10. V. Voliani, R. Bizzarri, R. Nifosi, S. Abbruzzetti, E. Grandi, C. Viappiani, F. Beltram, J. Phys. Chem. B **112**(34), 10714 (2008)
11. X.X. Zhou, H.K. Chung, A.J. Lam, M.Z. Lin, Science **338**(6108), 810 (2012)
12. K. Nienhaus, G.U. Nienhaus, Methods Appl. Fluores. **10**(4), 042002 (2022)
13. K. Nienhaus, G.U. Nienhaus, Chem. Soc. Rev. **43**(4), 1088 (2014)
14. S.J. Sahl, S.W. Hell, S. Jakobs, Nat. Rev. Mol. Cell Biol. **18**(11), 685 (2017)
15. A. Diaspro, P. Bianchini, Riv. Nuovo. Cimento. **43**(8), 385 (2020)
16. S.W. Hell, Nat. Methods **6**(1), 24 (2009)
17. N.A. Jensen, I. Jansen, M. Kamper, S. Jakobs, Nanoscale Photonic Imaging **134**, 241 (2020)
18. M. Pawlowska, R. Tenne, B. Ghosh, A. Makowski, R. Lapkiewicz, J. Phys.-Photon. **4**(1), 012002 (2022)
19. O. Shimomura, F.H. Johnson, Y. Saiga, J. Cell. Comp. Physiol. **59**, 223 (1962)
20. D.C. Prasher, V.K. Eckenrode, W.W. Ward, F.G. Prendergast, M.J. Cormier, Gene **111**(2), 229 (1992)
21. S. Inouye, F.I. Tsuji, FEBS Lett. **341**(2–3), 277 (1994)
22. M.V. Matz, A.F. Fradkov, Y.A. Labas, A.P. Savitsky, A.G. Zaraisky, M.L. Markelov, S.A. Lukyanov, Nat. Biotechnol. **17**(10), 969 (1999)
23. M.L. Macel, F. Ristoratore, A. Locascio, A. Spagnuolo, P. Sordino, S. D'Aniello, Zool. Lett. (2020). https://doi.org/10.1186/s40851-020-00161-9
24. T.J. Lambert, Nat. Methods **16**(4), 277 (2019)
25. O.V. Stepanenko, V.V. Verkhusha, I.M. Kuznetsova, V.N. Uversky, K.K. Turoverov, Curr. Protein Pept. Sci. **9**(4), 338 (2008)
26. T.D. Craggs, Chem. Soc. Rev. **38**(10), 2865 (2009)
27. D.A. Zacharias, J.D. Violin, A.C. Newton, R.Y. Tsien, Science **296**(5569), 913 (2002)
28. D. von Stetten, M. Noirclerc-Savoye, J. Goedhart, T.W.J. Gadella, A. Royant, Acta Crystallographica Sect. F-Struct. Biol. Commun. **68**, 878 (2012)
29. R.E. Campbell, O. Tour, A.E. Palmer, P.A. Steinbach, G.S. Baird, D.A. Zacharias, R.Y. Tsien, Proc. Natl. Acad. Sci. U.S.A. **99**(12), 7877 (2002)
30. T.M. Wannier, S.K. Gillespie, N. Hutchins, R.S. McIsaac, S.Y. Wu, Y. Shen, R.E. Campbell, K.S. Brown, S.L. Mayo, Proc. Natl. Acad. Sci. U.S.A. **115**(48), E11294 (2018)

31. B.L. Grigorenko, A.I. Krylov, A.V. Nemukhin, J. Am. Chem. Soc. **139**(30), 10239 (2017)
32. M. Bartkiewicz, S. Kazazic, J. Krasowska, P.L. Clark, B. Wielgus-Kutrowska, A. Bzowska, FEBS Lett. **592**(9), 1516 (2018)
33. A.A. Pakhomov, V.I. Martynov, Chem. Biol. **15**(8), 755 (2008)
34. S. Mukherjee, R. Jimenez, J. Phys. Chem. B **126**(4), 735 (2022)
35. M.J. Wang, Y. Da, Y. Tian, Chem. Soc. Rev. **52**(4), 1189 (2023)
36. M. Ormo, A.B. Cubitt, K. Kallio, L.A. Gross, R.Y. Tsien, S.J. Remington, Science **273**(5280), 1392 (1996)
37. H. Niwa, S. Inouye, T. Hirano, T. Matsuno, S. Kojima, M. Kubota, M. Ohashi, F.I. Tsuji, Proc. Natl. Acad. Am. Sci. **93**(24), 13617 (1996)
38. R.M. Wachter, Acc. Chem. Res. **40**(2), 120 (2007)
39. L. Zhang, H.N. Patel, J.W. Lappe, R.M. Wachter, J. Am. Chem. Soc. **128**(14), 4766 (2006)
40. N.M. Webber, K.L. Litvinenko, S.R. Meech, J. Phys. Chem. B **105**(33), 8036 (2001)
41. J. Dong, K.M. Solntsev, L.M. Tolbert, J. Am. Chem. Soc. **128**(37), 12038 (2006)
42. A.F. Bell, X. He, R.M. Wachter, P.J. Tonge, Biochemistry **39**(15), 4423 (2000)
43. A.A. Voityuk, M.E. Michel-Beyerle, N. Rosch, Chem. Phys. **231**(1), 13 (1998)
44. R. Bizzarri, R. Nifosì, Fluorescent proteins: structural determinants of optical response, in *CRC Handbook of Organic Photochemistry and Photobiology*, vol. 2, 3rd edn., ed. by A. Griesbeck, M. Oelgemöller, F. Ghettis (CRC Press, Boca Raton, 2012), p.1325
45. M.E. Martin, F. Negri, M. Olivucci, J. Am. Chem. Soc. **126**(17), 5452 (2004)
46. X. He, A.F. Bell, P.J. Tonge, FEBS Lett. **549**(1–3), 35 (2003)
47. D. Mandal, T. Tahara, S.R. Meech, J. Phys. Chem. B **108**(3), 1102 (2004)
48. K.L. Litvinenko, N.M. Webber, S.R. Meech, J. Phys. Chem. A **107**(15), 2616 (2003)
49. K.L. Litvinenko, N.M. Webber, S.R. Meech, Bull. Chem. Soc. Jpn **75**(5), 1065 (2002)
50. K.L. Litvinenko, N.M. Webber, S.R. Meech, Chem. Phys. Lett. **346**(1–2), 47 (2001)
51. A. Follenius-Wund, M. Bourotte, M. Schmitt, F. Iyice, H. Lami, J.J. Bourguignon, J. Haiech, C. Pigault, Biophys. J. **85**(3), 1839 (2003)
52. S.B. Nielsen, A. Lapierre, J.U. Andersen, U.V. Pedersen, S. Tomita, L.H. Andersen, Phys. Rev. Lett. (2001). https://doi.org/10.1103/PhysRevLett.87.228102
53. M.W. Forbes, R.A. Jockusch, J. Am. Chem. Soc. **131**(47), 17038 (2009)
54. C.W. West, A.S. Hudson, S.L. Cobb, J.R.R. Verlet, J. Chem. Phys. (2013). https://doi.org/10.1063/1.4819078
55. C.R.S. Mooney, D.A. Horke, A.S. Chatterley, A. Simperler, H.H. Fielding, J.R.R. Verlet, Chem. Sci. **4**(3), 921 (2013)
56. A. Svendsen, H.V. Kiefer, H.B. Pedersen, A.V. Bochenkova, L.H. Andersen, J. Am. Chem. Soc. **139**(25), 8766 (2017)
57. K. Addison, I.A. Heisler, J. Conyard, T. Dixon, P.C.B. Page, S.R. Meech, Faraday Discuss **163**, 277 (2013)
58. S. Olsen, K. Lamothe, T.J. Martinez, J. Am. Chem. Soc. **132**(4), 1192 (2010)
59. N.H. List, C.M. Jones, T.J. Martínez, Chem. Sci. **13**(2), 373 (2022)
60. J.S. Yang, G.J. Huang, Y.H. Liu, S.M. Peng, Chem. Commun. (Camb.) (2008). https://doi.org/10.1039/b717714c
61. E. Carrascosa, J.N. Bull, M.S. Scholz, N.J.A. Coughlan, S. Olsen, U. Wille, E.J. Bieske, J. Phys. Chem. Lett. **9**(10), 2647 (2018)
62. K. Addison, J. Conyard, T. Dixon, P.C.B. Page, K.M. Solntsev, S.R. Meech, J. Phys. Chem. Lett. **3**(16), 2298 (2012)
63. B. Hager, B. Schwarzinger, H. Falk, Monatsh. Chem. **137**(2), 163 (2006)
64. M.J. Li, Y.H. Lin, R. Sung, K.S. Sung, J. Phys. Chem. A **125**(17), 3614 (2021)
65. J. Dong, F. Abulwerdi, A. Baldridge, J. Kowalik, K.M. Solntsev, L.M. Tolbert, J. Am. Chem. Soc. **130**(43), 14096 (2008)
66. M. Drobizhev, P.R. Callis, R. Nifosì, G. Wicks, C. Stoltzfus, L. Barnett, T.E. Hughes, P. Sullivan, A. Rebane, Sci. Rep. (2015). https://doi.org/10.1038/srep13223
67. A.D. Kummer, J. Wiehler, H. Rehaber, C. Kompa, B. Steipe, M.E. Michel-Beyerle, J. Phys. Chem. B **104**(19), 4791 (2000)
68. K. Brejc, T.K. Sixma, P.A. Kitts, S.R. Kain, R.Y. Tsien, M. Ormo, S.J. Remington, Proc. Natl. Acad. Am. Sci. **94**(6), 2306 (1997)
69. R.M. Wachter, D. Yarbrough, K. Kallio, S.J. Remington, J. Mol. Biol. **301**(1), 157 (2000)

70. G.H. Patterson, S.M. Knobel, W.D. Sharif, S.R. Kain, D.W. Piston, Biophys. J. **73**(5), 2782 (1997)
71. G.J. Palm, A. Wlodawer, Methods Enzymol **302**, 378 (1999)
72. R. Bizzarri et al., Biochemistry **46**(18), 5494 (2007)
73. B. Storti, B. Carlotti, G. Chiellini, M. Ruglioni, T. Salvadori, M. Scotto, F. Elisei, A. Diaspro, P. Bianchini, R. Bizzarri, Int. J. Mol. Sci. **23**(5), 2482 (2022)
74. H. Morise, O. Shimomura, F.H. Johnson, J. Winant, Biochemistry **13**(12), 2656 (1974)
75. W.W. Ward, S.H. Bokman, Biochemistry **21**(19), 4535 (1982)
76. H. Lossau, A. Kummer, R. Heinecke, F. PollingerDammer, C. Kompa, G. Bieser, T. Jonsson, C.M. Silva, M.M. Yang, D.C. Youvan, M.E. MichelBeyerle, Chem. Phys. **213**(1–3), 1 (1996)
77. M. Chattoraj, B.A. King, G.U. Bublitz, S.G. Boxer, Proc. Natl. Acad. Am. Sci. **93**(16), 8362 (1996)
78. T.B. McAnaney, E.S. Park, G.T. Hanson, S.J. Remington, S.G. Boxer, Biochemistry **41**(52), 15489 (2002)
79. S. Bonsma, R. Purchase, S. Jezowski, J. Gallus, F. Konz, S. Volker, ChemPhysChem **6**(5), 838 (2005)
80. T.M. Creemers, A.J. Lock, V. Subramaniam, T.M. Jovin, S. Volker, Nat. Struct. Biol. **6**(6), 557 (1999)
81. J. Wiehler, G. Jung, C. Seebacher, A. Zumbusch, B. Steipe, ChemBioChem **4**(11), 1164 (2003)
82. R. Heim, R.Y. Tsien, Curr. Biol. **6**(2), 178 (1996)
83. A. Crameri, E.A. Whitehorn, E. Tate, W.P.C. Stemmer, Nat. Biotechnol. **14**(3), 315 (1996)
84. B.P. Cormack, R.H. Valdivia, S. Falkow, Gene **173**(1 Spec No), 33 (1996)
85. F.V. Subach, V.V. Verkhusha, Chem. Rev. **112**(7), 4308 (2012)
86. R.M. Wachter, J.L. Watkins, H. Kim, Biochemistry **49**(35), 7417 (2010)
87. A. Kikuchi, E. Fukumura, S. Karasawa, H. Mizuno, A. Miyawaki, Y. Shiro, Biochemistry **47**(44), 11573 (2008)
88. S.J. Remington, R.M. Wachter, D.K. Yarbrough, B. Branchaud, D.C. Anderson, K. Kallio, K.A. Lukyanov, Biochemistry **44**(1), 202 (2005)
89. X. Shu, N.C. Shaner, C.A. Yarbrough, R.Y. Tsien, S.J. Remington, Biochemistry **45**(32), 9639 (2006)
90. K. Nienhaus, G.U. Nienhaus, J. Wiedenmann, H. Nar, Proc. Natl. Acad. Sci. U.S.A. **102**(26), 9156 (2005)
91. A.B. Cubitt, R. Heim, S.R. Adams, A.E. Boyd, L.A. Gross, R.Y. Tsien, Trends Biochem. Sci. **20**(11), 448 (1995)
92. J.J. van Thor, A.J. Pierik, I. Nugteren-Roodzant, A.H. Xie, K.J. Hellingwerf, Biochemistry **37**(48), 16915 (1998)
93. J.J. van Thor, T. Gensch, K.J. Hellingwerf, L.N. Johnson, Nat. Struct. Biol. **9**(1), 37 (2002)
94. M.B. Elowitz, M.G. Surette, P.E. Wolf, J. Stock, S. Leibler, Curr. Biol. **7**(10), 809 (1997)
95. R.M. Dickson, A.B. Cubitt, R.Y. Tsien, W.E. Moerner, Nature **388**(6640), 355 (1997)
96. D. Sinnecker, P. Voigt, N. Hellwig, M. Schaefer, Biochemistry **44**(18), 7085 (2005)
97. R. Nifosi, A. Ferrari, C. Arcangeli, V. Tozzini, V. Pellegrini, F. Beltram, J. Phys. Chem. B **107**(7), 1679 (2003)
98. X.X. Zhou, M.Z. Lin, Curr. Opin. Chem. Biol. **17**(4), 682 (2013)
99. D.M. Chudakov, V.V. Belousov, A.G. Zaraisky, V.V. Novoselov, D.B. Staroverov, D.B. Zorov, S. Lukyanov, K.A. Lukyanov, Nat. Biotechnol. **21**(2), 191 (2003)
100. R. Ando, H. Mizuno, A. Miyawaki, Science **306**(5700), 1370 (2004)
101. V. Adam, B. Moeyaert, C.C. David, H. Mizuno, M. Lelimousin, P. Dedecker, R. Ando, A. Miyawaki, J. Michiels, Y. Engelborghs, J. Hofkens, Chem. Biol. **18**(10), 1241 (2011)
102. H. Chang, M.S. Zhang, W. Ji, J.J. Chen, Y.D. Zhang, B. Liu, J.Z. Lu, J.L. Zhang, P.Y. Xu, T. Xu, Proc. Natl. Acad. Sci. U.S.A. **109**(12), 4455 (2012)
103. B. Moeyaert, N.N. Bich, E. De Zitter, S. Rocha, K. Clays, H. Mizuno, L. Van Meervelt, J. Hofkens, P. Dedecker, ACS Nano **8**(2), 1664 (2014)
104. T. Brakemann et al., Nat. Biotechnol. **29**(10), 942 (2011)
105. Y. Arai, H. Takauchi, Y. Ogami, S. Fujiwara, M. Nakano, T. Matsuda, T. Nagai, ACS Chem. Biol. **13**(8), 1938 (2018)
106. S. Violot, P. Carpentier, L. Blanchoin, D. Bourgeois, J. Am. Chem. Soc. **131**(30), 10356 (2009)
107. J. Petersen, P.G. Wilmann, T. Beddoe, A.J. Oakley, R.J. Devenish, M. Prescott, J. Rossjohn, J. Biol. Chem. **278**(45), 44626 (2003)
108. N. Coquelle et al., Nat. Chem. **10**(1), 31 (2018)
109. S.P. Laptenok, A.A. Gil, C.R. Hall, A. Lukacs, J.N. Iuliano, G.A. Jones, G.M. Greetham, P. Donaldson, A. Miyawaki, P.J. Tonge, S.R. Meech, Nat. Chem. **10**(8), 845 (2018)
110. B. Grigorenko, A. Savitsky, I. Topol, S. Burt, A. Nemukhin, J. Phys. Chem. B **110**(37), 18635 (2006)

111. S.L.C. Moors, S. Michielssens, C. Flors, P. Dedecker, J. Hofkens, A. Ceulemans, J. Chem. Theory Comput. **4**(6), 1012 (2008)
112. B. Storti, E. Margheritis, G. Abbandonato, G. Domenichini, J. Dreier, I. Testa, G. Garau, R. Nifosi, R. Bizzarri, ACS Chem. Biol. **13**(8), 2082 (2018)
113. S. Habuchi, P. Dedecker, J.I. Hotta, C. Flors, R. Ando, H. Mizuno, A. Miyawaki, J. Hofkens, Photochem. Photobiol. Sci. **5**(6), 567 (2006)
114. L.V. Schäfer, G. Groenhof, A.R. Klingen, G.M. Ullmann, M. Boggio-Pasqua, M.A. Robb, H. Grubmüller, Angew. Chem. Int. Edit. **46**(4), 530 (2007)
115. S. Habuchi, R. Ando, P. Dedecker, W. Verheijen, H. Mizuno, A. Miyawaki, J. Hofkens, Proc. Natl. Acad. Sci. U.S.A. **102**(27), 9511 (2005)
116. M. Andresen, A.C. Stiel, S. Trowitzsch, G. Weber, C. Eggeling, M.C. Wahl, S.W. Hell, S. Jakobs, Proc. Natl. Acad. Sci. U.S.A. **104**(32), 13005 (2007)
117. R. Bizzarri, M. Serresi, F. Cardarelli, S. Abbruzzetti, B. Campanini, C. Viappiani, F. Beltram, J. Am. Chem. Soc. **132**(1), 85 (2010)
118. H. Mizuno, T.K. Mal, M. Walchli, A. Kikuchi, T. Fukano, R. Ando, J. Jeyakanthan, J. Taka, Y. Shiro, M. Ikura, A. Miyawaki, Proc. Natl. Acad. Sci. U.S.A. **105**(27), 9227 (2008)
119. S. Pletnev, F.V. Subach, Z. Dauter, A. Wlodawer, V.V. Verkhusha, J. Mol. Biol. **417**(3), 144 (2012)
120. J. Chang, M.G. Romei, S.G. Boxer, J. Am. Chem. Soc. **141**(39), 15504 (2019)
121. P.G. Wilmann, K. Turcic, J.M. Battad, M.C. Wilce, R.J. Devenish, M. Prescott, J. Rossjohn, J. Mol. Biol. **364**(2), 213 (2006)
122. D. Ruhlandt, M. Andresen, N. Jensen, I. Gregor, S. Jakobs, J. Enderlein, A.I. Chizhik, Commun. Biol. **3**(1), 627 (2020)
123. T. Matsuda, A. Miyawaki, T. Nagai, Nat. Methods **5**(4), 339 (2008)
124. T. Grotjohann, I. Testa, M. Reuss, T. Brakemann, C. Eggeling, S.W. Hell, S. Jakobs, Elife **1**, e00248 (2012)
125. S. Duwé, E. De Zitter, V. Gielen, B. Moeyaert, W. Vandenberg, T. Grotjohann, K. Clays, S. Jakobs, L. Van Meervelt, P. Dedecker, ACS Nano **9**(10), 9528 (2015)
126. F. Pennacchietti et al., Nat. Methods **15**(8), 601 (2018)
127. S. Wang, X.Z. Chen, L. Chang, R.Y. Xue, H.F. Duan, Y.J. Sun, ACS Nano **10**(10), 9136 (2016)
128. J. Blanc, D.L. Ross, J. Phys. Chem. **72**(8), 2817 (1968)
129. G. Zimmerman, L.-Y. Chow, U.-J. Paik, J. Am. Chem. Soc. **80**(14), 3528 (1958)
130. N.E. Christou, K. Giandoreggio-Barranco, I. Ayala, O. Glushonkov, V. Adam, D. Bourgeois, B. Brutscher, J. Am. Chem. Soc. **143**(19), 7521 (2021)
131. V. Adam et al., Chemphyschem **23**(19), e202200192 (2022)
132. G. Abbandonato, B. Storti, G. Signore, F. Beltram, R. Bizzarri, Microsc. Res. Tech. **79**(10), 929 (2016)
133. C. Fang, L.T. Tang, C. Chen, J. Chem. Phys. (2019). https://doi.org/10.1063/1.5128388
134. X. Li, L.W. Chung, H. Mizuno, A. Miyawaki, K. Morokuma, J. Phys. Chem. B **114**(2), 1114 (2010)
135. D. Bourgeois, V. Adam, IUBMB Life **64**(6), 482 (2012)
136. M. Kaucikas, M. Tros, J.J. van Thor, J. Phys. Chem. B **119**(6), 2350 (2015)
137. M.M. Warren, M. Kaucikas, A. Fitzpatrick, P. Champion, J.T. Sage, J.J. van Thor, Nat. Commun. **4**, 1461 (2013)
138. D. Yadav, F. Lacombat, N. Dozova, F. Rappaport, P. Plaza, A. Espagne, J. Phys. Chem. B **119**(6), 2404 (2015)
139. J.P. Colletier et al., J. Phys. Chem. Lett. **7**(5), 882 (2016)
140. J. Woodhouse et al., Nat. Commun. **11**(1), 741 (2020)
141. L.M. Uriarte et al., J. Phys. Chem. Lett. **13**(5), 1194 (2022)
142. A. Fadini et al., J. Am. Chem. Soc. **145**(29), 15796 (2023)
143. L.T. Tang, C. Fang, Int. J. Mol. Sci. **23**(12), 6459 (2022)
144. D. Smyrnova, K. Zinovjev, I. Tuñón, A. Ceulemans, J. Phys. Chem. B **120**(50), 12820 (2016)
145. D. Morozov, G. Groenhof, Angew. Chem. Int. Edit. **55**(2), 576 (2016)
146. D. Smyrnova, B. Moeyaert, S. Michielssens, J. Hofkens, P. Dedecker, A. Ceulemans, J. Phys. Chem. B **119**(36), 12007 (2015)
147. T. Grotjohann, I. Testa, M. Leutenegger, H. Bock, N.T. Urban, F. Lavoie-Cardinal, K.I. Willig, C. Eggeling, S. Jakobs, S.W. Hell, Nature **478**(7368), 204 (2011)
148. M. El Khatib, A. Martins, D. Bourgeois, J.P. Colletier, V. Adam, Sci. Rep. **6**, 18459 (2016)
149. J.D. Pedelacq, S. Cabantous, T. Tran, T.C. Terwilliger, G.S. Waldo, Nat. Biotechnol. **24**(1), 79 (2006)

150. A.E. Jablonski, R.B. Vegh, J.C. Hsiang, B. Bommarius, Y.C. Chen, K.M. Solntsev, A.S. Bommarius, L.M. Tolbert, R.M. Dickson, J. Am. Chem. Soc. **135**(44), 16410 (2013)
151. X. Zhang, M.S. Zhang, D. Li, W.T. He, J.X. Peng, E. Betzig, P.Y. Xu, Proc. Natl. Acad. Sci. U.S.A. **113**(37), 10364 (2016)
152. T. Roebroek, S. Duwé, W. Vandenberg, P. Dedecker, Int. J. Mol. Sci. (2017). https://doi.org/10.3390/ijms18092015
153. S. Abbruzzetti, R. Bizzarri, S. Luin, R. Nifosi, B. Storti, C. Viappiani, F. Beltram, Photochem. Photobiol. Sci. **9**(10), 1307 (2010)
154. M.G. Romei, C.Y. Lin, I.I. Mathews, S.G. Boxer, Science **367**(6473), 76 (2020)
155. C.Y. Lin, S.G. Boxer, J. Am. Chem. Soc. **142**(25), 11032 (2020)
156. C.Y. Lin, M.G. Romei, L.M. Oltrogge, I.I. Mathews, S.G. Boxer, J. Am. Chem. Soc. **141**(38), 15250 (2019)
157. T. Laino, R. Nifosi, V. Tozzini, Chem. Phys. **298**(1–3), 17 (2004)
158. A.C. Stiel, S. Trowitzsch, G. Weber, M. Andresen, C. Eggeling, S.W. Hell, S. Jakobs, M.C. Wahl, Biochem. J. **402**(1), 35 (2007)
159. M. Andresen, M.C. Wahl, A.C. Stiel, F. Grater, L.V. Schafer, S. Trowitzsch, G. Weber, C. Eggeling, H. Grubmuller, S.W. Hell, S. Jakobs, Proc. Natl. Acad. Sci. U.S.A. **102**(37), 13070 (2005)
160. A.B. Rosenbloom, S.H. Lee, M. To, A. Lee, J.Y. Shin, C. Bustamante, Proc. Natl. Acad. Sci. U.S.A. **111**(36), 13093 (2014)
161. J.N. Henderson, H.W. Ai, R.E. Campbell, S.J. Remington, Proc. Natl. Acad. Sci. U.S.A. **104**(16), 6672 (2007)
162. S. Wang, X.Z. Chen, L. Chang, M.A. Ding, R.Y. Xue, H.F. Duan, Y.J. Sun, Anal. Chem. **90**(11), 6626 (2018)
163. M. Andresen, A.C. Stiel, J. Folling, D. Wenzel, A. Schonle, A. Egner, C. Eggeling, S.W. Hell, S. Jakobs, Nat. Biotechnol. **26**(9), 1035 (2008)
164. R. Ando, C. Flors, H. Mizuno, J. Hofkens, A. Miyawaki, Biophys. J. **92**(12), L97 (2007)
165. S. Duwe, W. Vandenberg, P. Dedecker, Chem. Commun. **53**(53), 7242 (2017)
166. H. Mizuno, P. Dedecker, R. Ando, T. Fukano, J. Hofkens, A. Miyawaki, Photochem. Photobiol. Sci. **9**(2), 239 (2010)
167. C. Duan, V. Adam, M. Byrdin, D. Bourgeois, Structural basis of photoswitching in fluorescent proteins, in *Photoswitching Proteins: Methods and Protocols*. ed. by S. Cambridges (Springer, New York, 2014), p.177
168. X. Zhang, X.Z. Chen, Z.P. Zeng, M.S. Zhang, Y.J. Sun, P. Xi, J.X. Peng, P.Y. Xu, ACS Nano **9**(3), 2659 (2015)
169. Y.C. Chen, A.E. Jablonski, I. Issaeva, D. Bourassa, J.C. Hsiang, C.J. Fahrni, R.M. Dickson, J. Am. Chem. Soc. **137**(40), 12764 (2015)
170. H. Tsutsui, H. Shimizu, H. Mizuno, N. Nukina, T. Furuta, A. Miyawaki, Chem. Biol. **16**(11), 1140 (2009)
171. H.W. Ai, J.N. Henderson, S.J. Remington, R.E. Campbell, Biochem. J. **400**, 531 (2006)
172. S.Y. Wang, J.R. Moffitt, G.T. Dempsey, X.S. Xie, X.W. Zhuang, Proc. Natl. Acad. Sci. U.S.A. **111**(23), 8452 (2014)
173. S. Wang, Y. Shuai, C.Y. Sun, B.X. Xue, Y.P. Hou, X.D. Su, Y.J. Sun, Acs Sensors **3**(11), 2269 (2018)
174. N. Zhang, Y.Y. Zeng, W.W. Du, J.J. Zhu, D. Shen, Z.Y. Liu, J.A. Huang, Int. J. Oncol. **49**(4), 1360 (2016)
175. A.C. Stiel, M. Andresen, H. Bock, M. Hilbert, J. Schilde, A. Schönle, C. Eggeling, A. Egner, S.W. Hell, S. Jakobs, Biophys. J. **95**(6), 2989 (2008)
176. F.V. Subach, L. Zhang, T.W. Gadella, N.G. Gurskaya, K.A. Lukyanov, V.V. Verkhusha, Chem. Biol. **17**(7), 745 (2010)
177. F. Lavoie-Cardinal, N.A. Jensen, V. Westphal, A.C. Stiel, A. Chmyrov, J. Bierwagen, I. Testa, S. Jakobs, S.W. Hell, ChemPhysChem **15**(4), 655 (2014)
178. N.C. Shaner, R.E. Campbell, P.A. Steinbach, B.N.G. Giepmans, A.E. Palmer, R.Y. Tsien, Nat. Biotechnol. **22**(12), 1567 (2004)
179. E.M. Merzlyak, J. Goedhart, D. Shcherbo, M.E. Bulina, A.S. Shcheglov, A.F. Fradkov, A. Gaintzeva, K.A. Lukyanov, S. Lukyanov, T.W.J. Gadella, D.M. Chudakov, Nat. Methods **4**(7), 555 (2007)
180. N.C. Shaner, M.Z. Lin, M.R. McKeown, P.A. Steinbach, K.L. Hazelwood, M.W. Davidson, R.Y. Tsien, Nat. Methods **5**(6), 545 (2008)

181. S. Pletnev, D. Shcherbo, D.M. Chudakov, N. Pletneva, E.M. Merzlyak, A. Wlodawer, Z. Dauter, V. Pletnev, J. Biol. Chem. **283**(43), 28980 (2008)
182. D. Shcherbo, E.M. Merzlyak, T.V. Chepurnykh, A.F. Fradkov, G.V. Ermakova, E.A. Solovieva, K.A. Lukyanov, E.A. Bogdanova, A.G. Zaraisky, S. Lukyanov, D.M. Chudakov, Nat. Methods **4**(9), 741 (2007)
183. I.I. Shemiakina et al., Nat. Commun. **3**, 1204 (2012)
184. J. Wiedenmann, S. Ivanchenko, F. Oswald, F. Schmitt, C. Röcker, A. Salih, K.D. Spindler, G.U. Nienhaus, Proc. Natl. Acad. Sci. U.S.A. **101**(45), 15905 (2004)
185. V. Adam, M. Lelimousin, S. Boehme, G. Desfonds, K. Nienhaus, M.J. Field, J. Wiedenmann, S. McSweeney, G.U. Nienhaus, D. Bourgeois, Proc. Natl. Acad. Sci. U.S.A. **105**(47), 18343 (2008)
186. J. Fuchs, S. Böhme, F. Oswald, P.N. Hedde, M. Krause, J. Wiedenmann, G.U. Nienhaus, Nat. Methods **7**(8), 627 (2010)
187. T. Konen, D. Stumpf, T. Grotjohann, I. Jansen, M. Bossi, M. Weber, N. Jensen, S.W. Hell, S. Jakobs, ACS Nano **15**(6), 9509 (2021)
188. T. Brakemann, G. Weber, M. Andresen, G. Groenhof, A.C. Stiel, S. Trowitzsch, C. Eggeling, H. Grubmuller, S.W. Hell, M.C. Wahl, S. Jakobs, J. Biol. Chem. **285**(19), 14603 (2010)
189. E. Fron, M. Van der Auweraer, J. Hofkens, P. Dedecker, J. Phys. Chem. B **117**(51), 16422 (2013)
190. A. Walter, M. Andresen, S. Jakobs, J. Schroeder, D. Schwarzer, J. Phys. Chem. B **119**(16), 5136 (2015)
191. D.K. Tiwari, Y. Arai, M. Yamanaka, T. Matsuda, M. Agetsuma, M. Nakano, K. Fujita, T. Nagai, Nat. Methods **12**(6), 515 (2015)
192. T. Wazawa, R. Noma, S. Uto, K. Sugiura, T. Washio, T. Nagai, Microscopy **70**(4), 340 (2021)
193. K.A. Lukyanov et al., J. Biol. Chem. **275**(34), 25879 (2000)
194. M.L. Quillin, D.A. Anstrom, X.K. Shu, S. O'Leary, K. Kallio, D.A. Chudakov, S.J. Remington, Biochemistry **44**(15), 5774 (2005)
195. I.V. Yampolsky, S.J. Remington, V.I. Martynov, V.K. Potapov, S. Lukyanov, K.A. Lukyanov, Biochemistry **44**(15), 5788 (2005)
196. L.V. Schafer, G. Groenhof, M. Boggio-Pasqua, M.A. Robb, H. Grubmuller, PLoS Comput. Biol. **4**(3), e1000034 (2008)
197. P.G. Wilmann, J. Petersen, R.J. Devenish, M. Prescott, J. Rossjohn, J. Biol. Chem. **280**(4), 2401 (2005)
198. V.E. Zagranichny, N.V. Rudenko, A.Y. Gorokhovatsky, M.V. Zakharov, T.A. Balashova, A.S. Arseniev, Biochemistry **43**(42), 13598 (2004)
199. A.R. Faro, P. Carpentier, G. Jonasson, G. Pompidor, D. Arcizett, I. Demachy, D. Bourgeois, J. Am. Chem. Soc. **133**(41), 16362 (2011)
200. F. Lacombat, P. Plaza, M.A. Plamont, A. Espagne, J. Phys. Chem. Lett. **8**(7), 1489 (2017)
201. T. Sen, Y.Y. Ma, I.V. Polyakov, B.L. Grigorenko, A.V. Nemukhin, A.I. Krylov, J. Phys. Chem. B **125**(3), 757 (2021)
202. G.H. Patterson, J. Lippincott-Schwartz, Science **297**(5588), 1873 (2002)
203. J. Vangindertael, R. Camacho, W. Sempels, H. Mizuno, P. Dedecker, K.P.F. Janssen, Methods Appl. Fluores. **6**(2), 022003 (2018)
204. G. Vicidomini, *Image Formation in Fluorescence Microscopy* (Springer, Netherlands, Dordrecht, 2005)
205. B.R. Masters, Abbe's Theory of Image Formation in the Microscope, in Superresolution Optical Microscopy ed. (Springer Nature Switzerland AG, Cham, Switzerland, 2020), p. 65.
206. G. Toraldo di Francia, J. Opt. Soc. Am. **45**(7), 497 (1955)
207. M. Hofmann, C. Eggeling, S. Jakobs, S.W. Hell, Proc. Natl. Acad. Sci. U.S.A. **102**(49), 17565 (2005)
208. M. Lelek, M.T. Gyparaki, G. Beliu, F. Schueder, J. Griffié, S. Manley, R. Jungmann, M. Sauer, M. Lakadamyali, C. Zimmer, Nat. Rev. Methods Primers **1**(1), 39 (2021)
209. E. Betzig, G.H. Patterson, R. Sougrat, O.W. Lindwasser, S. Olenych, J.S. Bonifacino, M.W. Davidson, J. Lippincott-Schwartz, H.F. Hess, Science **313**(5793), 1642 (2006)
210. M.J. Rust, M. Bates, X. Zhuang, Nat. Methods **3**(10), 793 (2006)
211. S.T. Hess, T.P. Girirajan, M.D. Mason, Biophys. J. **91**(11), 4258 (2006)
212. S.W. Hell, J. Wichmann, Opt. Lett. **19**(11), 780 (1994)
213. M. Sauer, M. Heilemann, Chem. Rev. **117**(11), 7478 (2017)
214. Y.H. Lin, K. Nienhaus, G.U. Nienhaus, Chemnanomat **4**(3), 253 (2018)
215. A. Egner et al., Biophys. J. **93**(9), 3285 (2007)

216. C. Geisler, A. Schönle, C. von Middendorff, H. Bock, C. Eggeling, A. Egner, S.W. Hell, Appl. Phys. A-Mater. Sci. Process. **88**(2), 223 (2007)
217. C. Flors, J. Hotta, H. Uji-I, P. Dedecker, R. Ando, H. Mizuno, A. Miyawaki, J. Hofkens, J. Am. Chem. Soc. **129**(45), 13970 (2007)
218. H. Bock, C. Geisler, C.A. Wurm, C. Von Middendorff, S. Jakobs, A. Schönle, A. Egner, S.W. Hell, C. Eggeling, Appl. Phys. B-Lasers Opt. **88**(2), 161 (2007)
219. H. Shroff, C.G. Galbraith, J.A. Galbraith, E. Betzig, Nat. Methods **5**(5), 417 (2008)
220. C.J. Hsu, T. Baumgart, PLoS One **6**(8), e23586 (2011)
221. W. Vandenberg, M. Leutenegger, S. Duwé, P. Dedecker, Opt. Express **27**(18), 25749 (2019)
222. S. Geissbuehler, C. Dellagiacoma, T. Lasser, Biomed. Opt. Express **2**(3), 408 (2011)
223. T. Dertinger, R. Colyer, G. Iyer, S. Weiss, J. Enderlein, Proc. Natl. Acad. Sci. U.S.A. **106**(52), 22287 (2009)
224. P. Dedecker, G.C. Mo, T. Dertinger, J. Zhang, Proc. Natl. Acad. Sci. U.S.A. **109**(27), 10909 (2012)
225. F. Hertel, G.C.H. Mo, S. Duwe, P. Dedecker, J. Zhang, Cell Rep. **14**(2), 390 (2016)
226. A.M. Rozario, S. Duwé, C. Elliott, R.B. Hargreaves, G.W. Moseley, P. Dedecker, D.R. Whelan, T.D.M. Bell, Bmc Biol. (2021). https://doi.org/10.1186/s12915-021-01164-4
227. B. Moeyaert, W. Vandenberg, P. Dedecker, Biomed. Opt. Express **11**(2), 636 (2020)
228. D. Cevoli, R. Vitale, W. Vandenberg, S. Hugelier, R. Van den Eynde, P. Dedecker, C. Ruckebusch, Biomed. Opt. Express **12**(5), 2617 (2021)
229. R.B. Hargreaves, S. Duwé, A.M. Rozario, A.M. Funston, R.F. Tabor, P. Dedecker, D.R. Whelan, T.D.M. Bell, Acs Bio. Med. Chem. Au **3**(3), 261 (2023)
230. G.C.H. Mo et al., Nat. Methods **14**(4), 427 (2017)
231. W. Lin, G.C.H. Mo, S. Mehta, J. Zhang, J. Am. Chem. Soc. **143**(37), 14951 (2021)
232. S.W. Hell, K.I. Willig, M. Dyba, S. Jakobs, L. Kastrup, V. Westphal, Nanoscale resolution with focused light: stimulated emission depletion and other reversible saturable optical fluorescence transitions microscopy concepts, in *Handbook of Biological Confocal Microscopy*. ed. by J.B. Pawleys (Springer, Boston, 2006), p.571
233. S.W. Hell, M. Dyba, S. Jakobs, Curr. Opin. Neurobiol. **14**(5), 599 (2004)
234. S.W. Hell, Nat. Biotechnol. **21**(11), 1347 (2003)
235. G. Vicidomini, P. Bianchini, A. Diaspro, Nat. Methods **15**(3), 173 (2018)
236. S.W. Hell, Science **316**(5828), 1153 (2007)
237. N. Kilian, A. Goryaynov, M.D. Lessard, G. Hooker, D. Toomre, J.E. Rothman, J. Bewersdorf, Nat. Methods **15**(10), 755 (2018)
238. A. Chmyrov, J. Keller, T. Grotjohann, M. Ratz, E. d'Este, S. Jakobs, C. Eggeling, S.W. Hell, Nat. Methods **10**(8), 737 (2013)
239. L.A. Masullo, A. Bodén, F. Pennacchietti, G. Coceano, M. Ratz, I. Testa, Nat. Commun. **9**(1), 3281 (2018)
240. I. Testa, E. D'Este, N.T. Urban, F. Balzarotti, S.W. Hell, Nano Lett. **15**(1), 103 (2015)
241. X.C. Moreno, F. Pennacchietti, G. Minet, M. Damenti, D. Ollech, F. Barabas, I. Testa, J. Microsc. **291**(1), 16 (2023)
242. K. Mishra et al., Nat. Biotechnol. **40**(4), 598 (2022)
243. P. Dedecker, J.I. Hotta, C. Flors, M. Sliwa, H. Uji-I, M.B.J. Roeffaers, R. Ando, H. Mizuno, A. Miyawaki, J. Hofkens, J. Am. Chem. Soc. **129**(51), 16132 (2007)
244. L. Schermelleh, R. Heintzmann, H. Leonhardt, J. Cell Biol. **190**(2), 165 (2010)
245. J. Mertz, Nat. Methods **8**(10), 811 (2011)
246. E.H. Rego, L. Shao, J.J. Macklin, L. Winoto, G.A. Johansson, N. Kamps-Hughes, M.W. Davidson, M.G.L. Gustafsson, Proc. Natl. Acad. Sci. U.S.A. **109**(3), E135 (2012)
247. Y.C. Wu, H. Shroff, Nat. Methods **15**(12), 1011 (2018)
248. M.G.L. Gustafsson, Proc. Natl. Acad. Sci. U.S.A. **102**(37), 13081 (2005)
249. R. Heintzmann, T. Huser, Chem. Rev. **117**(23), 13890 (2017)
250. D. Li et al., Science **349**(6251), aab3500 (2015)
251. T.W. Gadella, ed. *FRET and FLIM Techniques*. Laboratory Techniques in Biochemistry and Molecular Biology, ed. S. Pillai, P.C. Van der Vliet. 2008, Elsevier: Amsterdam, The Netherlands
252. W.W. Parson, *Modern Optical Spectroscopy*, 1st edn. (Springer-Verlag, Berlin, 2007)
253. S.E. Braslavsky, E. Fron, H.B. Rodriguez, E.S. Roman, G.D. Scholes, G. Schweitzer, B. Valeur, J. Wirz, Photochem. Photobiol. Sci. **7**(12), 1444 (2008)
254. E.A. Jares-Erijman, T.M. Jovin, Nat. Biotechnol. **21**(11), 1387 (2003)

255. C.F. Kaminski, E.J. Rees, G.S.K. Schierle, Fluorescence Spectroscopy and Microscopy: Methods and Protocols **1076**, 445 (2014)
256. K. Suhling, P.M. French, D. Phillips, Photochem. Photobiol. Sci. **4**(1), 13 (2005)
257. J. Wlodarczyk, A. Woehler, F. Kobe, E. Ponimaskin, A. Zeug, E. Neher, Biophys. J. **94**(3), 986 (2008)
258. L. Giordano, T.M. Jovin, M. Irie, E.A. Jares-Erijman, J. Am. Chem. Soc. **124**(25), 7481 (2002)
259. E.A. Jares-Erijman, L. Giordano, C. Spagnuolo, J. Kawior, R.J. Vermeij, T.M. Jovin, Multiphoton Microscopy in the Biomedical Sciences Iv **5323**, 13 (2004)
260. C.D. Paul, C. Kiss, D.A.K. Traore, L. Gong, M.C.J. Wilce, R.J. Devenish, A. Bradbury, M. Prescott, PLoS One **8**(9), e75835 (2013)
261. P. Bianchini, A. Diaspro, C. Sheppard, M. Bouzin, *Multimodal and Nanoscale Optical Microscopy* (IOS Press, Washington, 2023)
262. S. Mao, R.K. Benninger, Y. Yan, C. Petchprayoon, D. Jackson, C.J. Easley, D.W. Piston, G. Marriott, Biophys. J. **94**(11), 4515 (2008)
263. G. Marriott et al., Proc. Natl. Acad. Sci. U.S.A. **105**(46), 17789 (2008)
264. C. Petchprayoon, Y. Yan, S. Mao, G. Marriott, Bioorg. Med. Chem. **19**(3), 1030 (2011)
265. Y. Yan, M.E. Marriott, C. Petchprayoon, G. Marriott, Biochem. J. **433**(3), 411 (2011)
266. T. Roebroek, W. Vandenberg, F. Sipieter, S. Hugelier, C. Stove, J. Zhang, P. Dedecker, Nat. Commun. **12**(1), 2005 (2021)
267. K.H. Rainey, G.H. Patterson, Proc. Natl. Acad. Sci. U.S.A. **116**(3), 864 (2019)
268. Y.T. Kao, X.X. Zhu, W. Min, Proc. Natl. Acad. Sci. U.S.A. **109**(9), 3220 (2012)
269. J.R. Lakowicz, *Principles of Fluorescence Spectroscopy*, 3rd edn. (Springer Science, New York, 2006)
270. B. Valeur, *Molecular Fluorescence: Principles and Applications*, 1st edn. (Wiley-VCH, Weinheim, 2001)
271. D.M. Jameson, J.A. Ross, Chem. Rev. **110**(5), 2685 (2010)
272. M. Erard, A. Fredj, H. Pasquier, D.B. Beltolngar, Y. Bousmah, V. Derrien, P. Vincent, F. Merola, Mol. Biosyst. **9**(2), 258 (2013)
273. P.H. Brown, A. Balbo, H.Y. Zhao, C. Ebel, P. Schuck, PLoS One **6**(10), e26221 (2011)
274. M.Y. Berezin, S. Achilefu, Chem. Rev. **110**(5), 2641 (2010)
275. A. Volpato, D. Ollech, J. Alvelid, M. Damenti, B. Müller, A.G. York, M. Ingaramo, I. Testa, Nat. Biotechnol. **41**(4), 552 (2023)
276. S. Ghosh, S. Saha, D. Goswami, S. Bilgrami, S. Mayor, Method Enzymol **505**, 291 (2012)
277. N.E. Snell, V.P. Rao, K.M. Seckinger, J.Y. Liang, J. Leser, A.E. Mancini, M.A. Rizzo, Biosensors-Basel **8**(4), 89 (2018)
278. L.W. Runnels, S.F. Scarlata, Biophys. J. **69**(4), 1569 (1995)
279. M.J. Dayel, E.F.Y. Hom, A.S. Verkman, Biophys. J. **76**(5), 2843 (1999)
280. R. Swaminathan, C.P. Hoang, A.S. Verkman, Biophys. J. **72**(4), 1900 (1997)
281. D.S. Lidke, P. Nagy, B.G. Barisas, R. Heintzmann, J.N. Post, K.A. Lidke, A.H.A. Clayton, D.J. Arndt-Jovin, T.M. Jovin, Biochem. Soc. Trans. **31**, 1020 (2003)
282. D. Axelrod, Biophys. J. **26**(3), 557 (1979)
283. D.W. Piston, M.A. Rizzo, Fluorescent Proteins, Second Edition 85415 (2008)
284. N. Ojha, K.H. Rainey, G.H. Patterson, Nat. Commun. (2020). https://doi.org/10.1038/s41467-019-13843-6
285. N.N. Bich, B. Moeyaert, K. Van Hecke, P. Dedecker, H. Mizuno, J. Hofkens, L. Van Meervelt, Acta Crystallogr. Sect. D-Struct. Biol. **68**, 1653 (2012)
286. X.X. Zhou, L.L.Z. Fan, P.P. Li, K. Shen, M.Z. Lin, Science **355**(6327), 836 (2017)
287. X.X. Zhou, X.Z. Zou, H.Y.K. Chung, Y.C. Gao, Y.X. Liu, L.S. Qi, M.Z. Lin, ACS Chem. Biol. **13**(2), 443 (2018)
288. J. Ju, H.N. Lee, L. Ning, H. Ryu, X.X. Zhou, H. Chun, Y.W. Lee, A.I. Lee-Richerson, C. Jeong, M.Z. Lin, J. Seong, Cell Rep. **40**(2), 111080 (2022)
289. V. Adam, R. Berardozzi, M. Byrdin, D. Bourgeois, Curr. Opin. Chem. Biol. **20**, 92 (2014)